

---

# Time-dependent boundaries in numerical models

Nils Peter Wedi

---



München 2004



---

# **Time-dependent boundaries in numerical models**

**Nils Peter Wedi**

---

Dissertation  
an der Fakultät für Physik  
der Ludwig-Maximilians-Universität  
München

vorgelegt von  
Nils Peter Wedi  
aus Greven, Nordrhein-Westfalen

München, den 28.10.2004

Erstgutachter: Prof. Dr. U. Schumann

Zweitgutachter: Prof. Dr. J. Egger

Tag der mündlichen Prüfung: 21.01.2005



# Contents

<b>Zusammenfassung</b>	<b>xi</b>
<b>Abstract</b>	<b>xiii</b>
<b>1 Introduction</b>	<b>1</b>
1.1 Preamble	1
1.2 Numerical modelling of the atmosphere in curvilinear coordinates	2
1.3 The quasi-biennial oscillation	4
1.4 Linear internal wave theory of Boussinesq flow	8
1.5 Wave propagation and the relevance of boundary conditions	12
1.5.1 Rigid surface	13
1.5.2 Pliant and free surface	14
1.5.3 Free-slip and no-slip velocity boundary conditions	16
1.5.4 “Infinite depth”	18
1.6 Methodology and thesis questions	19
<b>2 Modelling framework</b>	<b>21</b>
2.1 Model summary	21
2.2 Generalised Gal-Chen & Somerville vertical coordinate	23
2.3 The numerical approximation	26
<b>3 Examples of applications</b>	<b>29</b>
3.1 Boundary forced oscillating flow	29
3.2 Orographically-forced atmospheric gravity waves	30
3.3 Finite amplitude free surface flow	34
<b>4 The numerical equivalent to the quasi-biennial oscillation analogue</b>	<b>41</b>
4.1 Experimental setup	42
4.2 Summary of the numerical simulations	43
4.2.1 Parametric sensitivities	51
4.2.2 Numerical sensitivities, linearisation and boundary effects	54
4.3 Energy budget	60
4.4 Spectral analysis	66

---

4.5	Theoretical considerations to the QBO analogue . . . . .	67
4.6	A revised schematic description of the QBO analogue . . . . .	73
4.7	Summary . . . . .	83
<b>5</b>	<b>Discussion</b>	<b>87</b>
5.1	The generalised time-dependent coordinate transformation . . . . .	87
5.2	Implications for atmospheric equatorial zonal mean flow oscillations . . . . .	88
5.3	Future work . . . . .	94
<b>6</b>	<b>Conclusions</b>	<b>95</b>
<b>A</b>	<b>Tensor algebra</b>	<b>97</b>
A.1	Curvilinear framework - the transformation of coordinates . . . . .	97
A.1.1	General definitions of tensor analysis . . . . .	98
A.1.2	The momentum equation . . . . .	101
A.1.3	The momentum equation in strong conservation formulation . . . . .	101
A.1.4	The continuity equation . . . . .	102
A.1.5	Spherical coordinates . . . . .	103
A.1.6	Free surface boundary condition . . . . .	104
A.2	Symbol tables . . . . .	106
	<b>Acknowledgements</b>	<b>119</b>

# List of Figures

1.1	The quasi-biennial oscillation as analysed in ERA40 in a time-height representation. . . . .	4
1.2	Picture of the cylindrical annulus used for the QBO experiments at the university of Kyoto. . . . .	6
1.3	Example of fully reflected gravity waves from the top of a computational domain. . . . .	14
1.4	Example of gravity wave reflection from the model top in the ECMWF forecast model. . . . .	17
1.5	Example of (artificial) wave absorption at the model top in the operational ECMWF forecast model. . . . .	19
3.1	Oscillating membranes bounding a homogeneous Boussinesq fluid. . . . .	31
3.2	Vertical velocity for the flow past a given terrain profile after 5 hours of simulation. . . . .	33
3.3	The regime diagram for the hydrostatic shallow-water equations. . . . .	36
3.4	Summary of the solutions with a gentle slope for subcritical, critical and supercritical flow conditions at time $t = 0.5$ . . . . .	37
3.5	Time evolution of a critical flow at time $t = 0.15$ and $t = 0.5$ , respectively, for a predicted shallow-water upper surface and a “two-layer” simulation. . . . .	38
3.6	Solutions for a critical flow past a steep mountain at time $t = 0.15$ and $t = 0.5$ , for a predicted shallow-water upper surface and a “two-layer” simulation. . . . .	40
4.1	The shape of the oscillating membrane in the Plumb-McEwan experiment. . . . .	42
4.2	Time-height cross-sections of the zonal-mean flow velocity at $y = L_y/2$ in the numerical simulations. . . . .	44
4.3	Different phases during the numerical 2D simulation of the Plumb-McEwan laboratory analogue of the quasi-biennial oscillation (QBO). . . . .	45
4.4	Time-height cross-sections of the zonal-mean flow velocity at $y = L_y/2$ in the 3D numerical simulation in comparison to the corresponding 2D simulation. . . . .	49
4.5	Time-height cross-section of the zonal-mean flow velocity at $y = L_y/2$ in the numerical simulation of the laboratory setup at the university of Kyoto. . . . .	50
4.6	Time height cross section of the zonal mean flow for a mixed wavenumber/frequency forcing. . . . .	53

4.7	Time-height cross-section of the zonal-mean flow velocity in the 2D numerical simulation using a noslip rigid upper boundary with a flux-form Eulerian advection scheme. . . . .	56
4.8	Time-height cross-section of the zonal-mean flow velocity in the 2D numerical simulation using a noslip rigid upper boundary with a semi-Lagrangian advection scheme. . . . .	57
4.9	Potential energy budget for the flux-form Eulerian advection case. . . . .	60
4.10	Potential energy budget for the semi-Lagrangian advection case. . . . .	61
4.11	Kinetic energy budget. . . . .	62
4.12	Energy diagram for density stratified Boussinesq flow. . . . .	64
4.13	Exchange rates of energy. . . . .	65
4.14	Comparison of zonal wind, horizontal and vertical wave numbers, and dominant frequencies diagnosed at selected time intervals by spectrally analysing the zonal velocity. . . . .	68
4.15	The principle mechanism of the oscillation in the laboratory experiment of Plumb and McEwan in four representative phases of the zonal mean zonal flow. . . . .	74
4.16	Time-height cross-section of the zonal-mean flow velocity for the in detail described phases of the mean flow reversal. . . . .	75
4.17	Symmetric gravity are excited by the oscillating membrane in the beginning of the simulation with no background flow. . . . .	76
4.18	Time evolution of zonal wind between $t=15\text{min}$ to $t=23\text{min}$ . . . . .	77
4.19	Time evolution of local Richardson number between $t=15\text{min}$ to $t=23\text{min}$ . . . . .	78
4.20	Time evolution of zonal mean wind between $t=15\text{min}$ to $t=23\text{min}$ . . . . .	79
4.21	Time evolution of Reynolds stress between $t=15\text{min}$ to $t=23\text{min}$ . . . . .	80
4.22	Time evolution of horizontal and vertical wave numbers between $t=15\text{min}$ to $t=23\text{min}$ . . . . .	81
4.23	The existence of horizontal wave numbers in 9 equidistant vertical levels during one half period of the reversing mean flow. . . . .	82
4.24	The observed horizontal velocity data in comparison to the signal reconstructed from the dominant wave spectrum. . . . .	83
5.1	The quasi-biennial oscillation as analysed in ERA40 in a three dimensional time-height representation. . . . .	88
5.2	A QBO-like oscillation in a T63 IFS model simulation with 91 levels and no parametrized convection in the simulation. . . . .	92
5.3	Instantaneous horizontal distribution of the driving forces for the QBO-like oscillation in the T63 IFS model with 91 levels. . . . .	93
A.1	Relation between the stresses on the two sides of a boundary between two fluids. . . . .	104

# List of Tables

3.1	Summary of representative experiments for free surface flows in distinct flow regimes characterised by the dimensionless Froude number $F_u$ , normalised ridge height $z_{s0}/d_0$ and normalised half-width $a/d_0$ . . . . .	38
4.1	Quantitative comparison of the mean-flow oscillations in the laboratory experiments and the 3D numerical simulations. . . . .	47
4.2	Quantitative comparison of the mean-flow oscillations in the 3D laboratory experiments with the 2D numerical simulations. . . . .	48
A.1	Description of Abbreviations. . . . .	106
A.2	Description of symbols in the text. . . . .	106



# Zusammenfassung

Die vorliegende Dissertation beschreibt die Entwicklung eines neuen numerischen Verfahrens zur Untersuchung von grundlegenden atmosphärischen Vorgängen sowie deren numerischer Verwirklichbarkeit, welche weder aus hoch optimierten operationellen Wettervorhersagemodellen noch aus idealisierten Laboruntersuchungen abgeleitet werden können. Hierbei wird die theoretische Entwicklung und die numerisch effiziente Implementierung einer verallgemeinerten Koordinatentransformation beschrieben, welche es erlaubt, den Einfluss unterschiedlicher unterer und oberer Randbedingungen in atmosphärischen und ozeanischen Strömungssimulationen mit demselben numerischen Apparat zu untersuchen. Der technische Aspekt dieser Arbeit trägt dazu bei, die Anpassungsfähigkeit numerischer Modelle an äussere Antriebe, die sich aus Beobachtungen oder anderen Daten ergeben, zu erhöhen. Die theoretische Herleitung wird mit idealisierten numerischen Simulationen illustriert. Ein Beispiel einer praktischen Anwendung mit direkter Relevanz für ozeanische Simulationen wird beschrieben, in welcher die Randbedingung einer nicht notwendigerweise infinitesimalen freien Oberfläche durch eine Näherung, gültig für lange Wellen, approximiert wird.

Die verallgemeinerte Koordinatentransformation und ihre Anwendbarkeit für die Simulation von stabil geschichteten Strömungen mit komplizierten geometrischen, zeitabhängigen Randbedingungen wird in der direkten numerischen Simulation des Laborexperimentes, in Analogie zur “quasi-biennial oscillation” (QBO), der dominanten Variabilität in der äquatorialen Stratosphäre, unter Beweis gestellt. Obwohl das Laborexperiment den prinzipiellen Mechanismus der QBO widerspiegelt, und bereits viele numerische Studien dieser etwa zweijährigen Oszillation durchgeführt wurden, ist dieses tropische Phänomen nicht vollständig erklärt. Basierend auf den numerischen Ergebnissen dieser Arbeit folgt eine gegenüber der ursprünglichen Erklärung abweichende Beschreibung der Vorgänge im Laborexperiment. Die Ergebnisse unterstreichen die Nützlichkeit der in dieser Dissertation entwickelten Methode und rehabilitieren zudem auch die Wichtigkeit der Laboranordnung im Bezug auf seine fundamentale Ähnlichkeit zur Atmosphäre. Die hier präsentierte detaillierte Analyse der Abhängigkeit von den Parametern des Experimentes und der numerischen Einflüsse auf die Oszillation erlaubt es, Schlussfolgerungen über die erfolgreiche numerische Simulation sowie über die Theorie von äquatorialen Oszillationen zu ziehen.





# Abstract

This dissertation describes the development of a new numerical framework enabling the study of principal atmospheric mechanisms as well as aspects of numerical realisability that are neither easily deduced from highly optimised operational numerical weather prediction models nor idealised laboratory studies. The theoretical development and efficient numerical implementation of a generalised time-dependent coordinate transformation is demonstrated, creating a unified numerical framework for investigating the influence of upper and lower boundary conditions on atmospheric and oceanic flows. In technical terms, the dissertation also enhances the adaptivity of numerical models to boundary forcings determined by data. The theoretical development is illustrated with numerical simulations of idealised flows. An example of a practical application is given which incorporates a long-wave-approximation for a finite-amplitude free-surface upper boundary, directly relevant to ocean models.

Finally, the utility of the generalised vertical coordinate in simulating stratified flows with intricate geometric, time-dependent boundary forcings is demonstrated in the direct numerical simulation of the laboratory analogue of the quasi-biennial oscillation (QBO), the dominant variability in the equatorial stratosphere. While the laboratory experiment exhibits the principal mechanism of the QBO, and despite numerous studies of the stratospheric phenomenon, a complete understanding of the QBO eludes the efforts. On the basis of the numerical results presented in this thesis, the original explanation of the laboratory experiment is revised. The findings stress the utility of this numerical framework and further elevate the importance of the laboratory setup for its fundamental similarity to the atmosphere. A detailed study of parametric and numerical sensitivities of the oscillation is presented and implications on the successful simulation and on the existing theory of equatorial oscillations are discussed.



# Chapter 1

## Introduction

### 1.1 Preamble

The importance of an accurate representation of the upper boundary condition in meteorological models is well appreciated since it affects short- and medium-range weather prediction (Lindzen et al., 1968; Phillips, 1990), climate studies (Trenberth and Stepaniak, 2002), and predictability of chaotic systems in general (Chu, 1999). However, a unified numerical framework to investigate the influence of various upper boundary assumptions does not exist, because each model formulation favours a particular type of the upper boundary. For example, it is easy to impose a free-surface boundary condition in an isopycnic/isentropic model, but it is rather difficult to impose a rigid lid, easily applied in linear coordinates. Furthermore, there is an outstanding issue with modelling open boundaries that eludes a satisfactory solution in many areas of computational physics; cf. Givoli (1991) and references therein; for implementations of radiative boundary conditions in meteorology see (Klemp and Durran, 1983; Bougeault, 1983; Herzog, 1995). In particular, Grosch and Orszag (1977) investigated the utility of coordinate transformations to solve numerically problems in infinite regions. They concluded that stationary mappings onto finite domains are “useless for many important physical problems.”

Gal-Chen & Somerville provided a formulation of the Navier-Stokes equations in a generalised non Cartesian, nonorthogonal coordinate system suitable for numerical integration (Gal-Chen and Somerville, 1975). In this thesis <sup>1</sup>, the time-dependent extension by Prusa et al. (1996) of the Gal-Chen & Somerville transformation is generalised for curvilinear time-dependent boundaries at the top as well as the bottom of the model domain. Explicit formulae are provided for the relevant metric coefficients and the implementation is discussed in the context of a strong-conservation formulation of the nonhydrostatic anelastic equations of Lipps and Hemler (1982). The aim is to create a unified numerical framework for investigating the influence of upper boundary conditions on atmospheric

---

<sup>1</sup>The technical part of this thesis has been summarised and published in Wedi and Smolarkiewicz (2004a). A description of the experimental setup and preliminary results of the direct numerical simulation of the QBO analogue are given in Wedi and Smolarkiewicz (2004b).

and oceanic flows. In technical terms, this thesis enhances the adaptivity of numerical models to boundary forcings determined by data. To illustrate both aspects, simulations of an orographic flow in a homogeneous incompressible fluid (bounded by a rigid-lid or by a finite-amplitude free-surface) are compared with the simulation of an incompressible two-layer fluid with a density ratio 1/1000 at the interface. In the simulation with the free-surface, the time-dependent coordinate transformation is driven by the solution of the shallow-water equations, the lowest-order long-wave approximation to free-surface flows. The physics of this example is relevant to ocean models. In numerical simulations of ocean circulations “mode splitting” is often applied to accommodate surface gravity waves with propagation speeds much larger than velocities of internal flows (Madala and Piacsek, 1977; Higdon, 2002). The development in section 3.3 provides an alternative for incorporating a finite-amplitude free surface upper boundary in ocean models.

## 1.2 Numerical modelling of the atmosphere in curvilinear coordinates

In meteorology, continuous coordinate transformations using a general curvilinear framework are favoured, because they simplify theories and models by reflecting the natural material structure of atmospheres and oceans (Dutton, 1986). The latter exploits the notion of a “metric structure determined by data” — Riemann’s seminal idea on the foundations of geometry (Riemann, 1873), an inspiration behind the mathematical apparatus of general relativity (Freudenthal, 1980). For example, the density stratification and near hydrostatic balance of the Earth atmosphere favour pressure as a vertical coordinate of weather prediction models, assuring an approximate equipartition of mass and energy in computational cells (Phillips, 1957; Kasahara, 1974; Laprise, 1992). Similarly, the stable entropy [density] stratification in deep atmospheres [oceans] makes an isentropic [isopycnic] framework practical (Bleck, 1974; Hsu and Arakawa, 1990; Bleck and Smith, 1990; Higdon, 2002). Attempts to exploit the advantages of different curvilinear frameworks for various regions of a simulated atmosphere [ocean] have led to pressure- or entropy-based coordinate hybridisation (Ucellini et al., 1979; Simmons and Burridge, 1981; Suarez et al., 1983; Konor and Arakawa, 1997). The majority of currently-operational numerical weather prediction models are formulated in hybrid coordinates.

An important property of curvilinear coordinates is their ability to accommodate domains with irregular boundaries. In meteorology, these are typically associated with complex natural orography [bathymetry]. The accurate representation of the underlying metric structure is particularly important for modelling stably stratified rotating media, where the boundary forcing excites internal inertia-gravity waves affecting the far-field flow. For example, the (non-Boussinesq) amplification of vertically propagating gravity waves, due to the density decrease with altitude, can lead to clear-air turbulence (via wave steepening and subsequent breaking) in the middle atmosphere (Prusa et al., 1996). Weather prediction models have traditionally used pressure normalised by surface pressure in the definition

of the “vertical” coordinate to represent accurately the influence of the terrain variability on large-scale planetary flows (Phillips, 1957). Gal-Chen and Somerville (1975) were the first to incorporate terrain-following curvilinear coordinates in the nonhydrostatic anelastic Navier-Stokes equations appropriate for small-scale atmospheric and oceanic flows. They transformed a linear vertical coordinate (as opposed to pressure) and provided closed-form explicit formulae for the relevant metric terms and coefficients. By construction, their transformation separates all metric coefficients into products of 2D horizontal and 1D vertical fields, facilitating a computationally efficient implementation.

The Gal-Chen & Somerville development employed the classical coordinate-invariant tensor representation (a “weak-conservation formulation”) where the consistently transformed, dependent variables are solved in the framework of the transformed coordinates. While the invariance of the formulation is beneficial in theory, it has considerable disadvantages in the numerical implementation. Due to Christoffel terms arising in the transformed momentum equation, the conservation of physical (measurable) kinematic variables may be difficult to achieve. Furthermore, since Christoffel terms represent inertial accelerations due to the curvilinearity of the coordinates, they only affect flow direction but not the flow magnitude. To minimise truncation-error departures from this “inertness” in numerical algorithms, it is important to express the Christoffel terms centred-in-time. While straightforward in three-time-level centred-in-time-and-space (leapfrog) schemes, this leads in two-time level algorithms (forming the base of modern nonoscillatory methods) to an implicit nonlinear problem. Both issues are circumvented in the “strong-conservation formulation” advocated by Clark (1977) — a standard in computational aerodynamics (Anderson et al., 1984) — where the governing equations are solved in the framework of Gal-Chen & Somerville transformed coordinates, but for the untransformed physical velocity. However, the strong-conservation formulation adds some conceptual complexity in incompressible type models, due to the presence of several forms of velocity and an elaborate procedure for formulating the elliptic pressure equation (Prusa and Smolarkiewicz, 2003). The early contributions of Gal-Chen and Somerville (1975) and Clark (1977) were fundamental to the development of many small- and mesoscale models in meteorology (over 500 citations since 1975; (ISI, 2002)). More recently, the stationary terrain-following transformation of Gal-Chen and Somerville was extended in (Prusa et al., 1996) to allow for time-dependent lower boundaries. In this thesis the theory and the numerical implementation is further extended to allow for time-dependent upper boundaries and its usefulness is demonstrated in various applications. Both developments readily extend the range of applications of multiple scale models like MESOSCOP (Schumann et al., 1987) or GESIMA (Kapitza and Eppel, 1992), which already include the stationary terrain-following formalism of Clark (1977), to a class of important problems of internal wave phenomena driven by (time-dependent) boundary enforced wave motions.

In particular, the new development is shown to be useful for the investigation into poorly understood aspects of the quasi-biennial oscillation (QBO). The versatility of the framework is demonstrated in the direct numerical simulation (DNS) of the QBO analogue, a laboratory experiment by Plumb and McEwan (1978) that demonstrates the principle mechanism of this equatorial stratospheric phenomenon. The QBO represents a conspic-

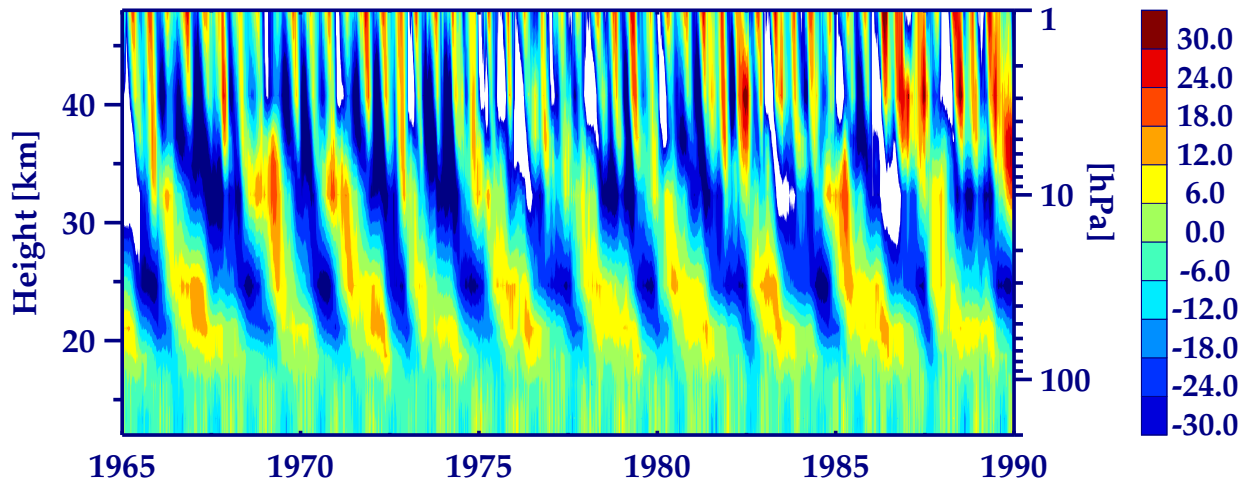


Figure 1.1: The quasi-biennial oscillation as analysed in ERA40 in a time-height representation. The figure shows the equatorial analysed (unfiltered) zonal mean zonal wind between 200hPa and 1hPa averaged between  $\pm 1$  degrees latitude for the period 1965-1990. The contour interval is  $6 \text{ ms}^{-1}$ .

uous example of a fundamental dynamical mechanism with challenging detail, which is difficult to deduce from experimental evidence alone. Here the conceptual simplicity of the experiment is used to provide a catalogue of sensitivities that can be employed in numerical weather prediction and climate models to facilitate a successful simulation of such a mean-flow oscillation.

### 1.3 The quasi-biennial oscillation

The quasi-biennial oscillation (QBO) of the zonal-mean zonal wind in the equatorial stratosphere is one of the few atmospheric examples exhibiting a periodic behaviour without the association of a periodic forcing function (like externally forced diurnal or annual components) (Holton, 1992). The observed features of the QBO can be seen in the time-height cross section of zonal wind speed at the equator from 25 years of the ERA40 dataset (Uppala et al., 2004) which is depicted in figure 1.1. The analysed QBO compares well with radiosonde and rocket sonde data from various tropical locations (Baldwin et al., 2001). The following features are observed:

- Zonally symmetric easterly and westerly wind regimes alternate quasi-regularly with periods varying from 24 – 30 month (Holton, 1992; Baldwin et al., 2001).
- Successive regimes of westward and eastward zonal mean zonal wind first appear somewhere around a height of 40 km and propagate downward at a rate of approximately  $1 \text{ km month}^{-1}$  (Holton, 1992).

- The downward propagation appears to proceed without loss of amplitude between 30 and 23 km, but there is rapid attenuation below 23 km (Holton, 1992).
- The oscillation is almost symmetric about the equator with a maximum amplitude of about 20 m s<sup>-1</sup> and approximately Gaussian distribution in latitude with a half-width of about 12 degrees latitude (Holton, 1992), see also figure 5.1.
- The westerly phases (eastward wind, positive with yellow-red shading in figure 1.1) of the QBO appear to propagate downward faster and more regularly. The easterly phases (westward wind, negative with green-blue in figure 1.1) are characterised by stronger intensity and longer duration (Baldwin et al., 2001; Gabis and Troshichev, 2004; and references therein).

The QBO represents the dominant variability in the equatorial stratosphere (Baldwin et al., 2001). It exhibits a fundamental dynamical mechanism with challenging detail. Lindzen and Holton (1968) and Holton and Lindzen (1972) were among the first to present a conceptual model of the QBO describing the oscillation as an interaction between the mean flow and propagating waves. In a viscous, non-rotating Boussinesq fluid, the interaction can be described by the averaged momentum equations in a horizontally periodic domain as

$$\frac{\partial U}{\partial t} - \nu \frac{\partial^2 U}{\partial z^2} = - \sum_i \frac{\partial F_i}{\partial z}, \quad (1.1)$$

where  $U := \overline{u^{xy}}$  denotes the horizontally averaged (mean) flow,  $\nu$  denotes the kinematic viscosity and  $F := \overline{u'w'^{xy}}$  expresses the averaged nonlinear momentum flux. Most atmospheric research of the QBO is devoted to finding the precise physical origins of the right-hand side of equation (1.1) and their numerical realisability in the context of numerical weather prediction and climate modelling. In spite of numerous studies, see Baldwin et al. (2001) for a recent comprehensive review, a complete understanding of the QBO eludes the efforts.

The principal mechanism of the QBO was demonstrated in the laboratory experiment of Plumb and McEwan (1978). The laboratory setup consists of a cylindrical annulus (figure 1.2) filled with density-stratified salty water, forced at the lower boundary by an oscillating membrane. At sufficiently large forcing amplitude the wave motion generates an oscillation in the zonal mean zonal flow with relatively long periods compared to the period of the forcing oscillations. The laboratory experiment is often employed to explain the basic mechanism of the atmospheric QBO (Baldwin et al., 2001). However, it also has been criticised for its apparent fundamental difference to the QBO. In the laboratory, the averaged momentum-flux  $F$  has been attributed to viscous and thermal internal wave dissipation (Plumb, 1977; Plumb and McEwan, 1978). In the atmosphere, a competing explanation states wave transience as the chronologically more important primary cause of the oscillation (McIntyre, 1994; Dunkerton, 1981). Consequently, a direct application of the analysis of the laboratory results to atmospheric observations has been questioned (Dunkerton, 1981).

In the context of the atmospheric QBO it was first suggested by Lindzen and Holton in 1968 that the stratospheric mean flow oscillation is driven by critical layer absorption



Figure 1.2: A picture of the cylindrical annulus used for the QBO experiments at the university of Kyoto ([www.gfd-dennou.org](http://www.gfd-dennou.org), 2004). In the picture the oscillating membrane can be seen at the top of the annulus, while in the original experiment of Plumb and McEwan the membrane was mounted at the bottom.

of a spectrum of gravity waves. Later in 1972 Holton and Lindzen updated their theory discarding critical level influence since they could not observe a precise, pre-existing critical level for the waves they considered most likely responsible, i.e. equatorial Kelvin and Rossby-gravity waves. Instead they argued that the upward propagating waves are attenuated primarily by infrared cooling. Plumb (1977) presented the corresponding theory in the context of an idealised Boussinesq fluid and later Plumb and McEwan (1978) conducted the aforementioned laboratory experiment that seemed to agree with this theory. Their conceptual model together with the theories presented in Lindzen and Holton (1968) and Holton and Lindzen (1972) established the fundamental picture of the QBO as forced by upward-propagating waves. The rate of downward propagation of the QBO is determined by the intensity of the upward-propagating waves, while the amplitude of the QBO is largely determined by the phase speeds of the upward-propagating waves (Lindzen, 1987). This is still the accepted basic theory for the principal mechanism of the atmospheric QBO. McIntyre (1994) and Dunkerton (1981) argued that not radiative damping but wave-interactions are the chronologically more important cause of the oscillation. Furthermore, Dunkerton (1997) showed that the tropical upwelling, a climatic mean upward motion of the tropical atmosphere, necessitates contributions of other wave types to the mean flow momentum budget. He argued that gravity waves contribute up to 50 percent to the forcing. However, there is still considerable uncertainty about the precise origin and the nature of the waves responsible for driving the QBO. In Horinouchi (2003) a spectral analysis of several global models appears to confirm the relative unimportance of equatorial Kelvin and Rossby-gravity waves as the primary source of the QBO. Furthermore, the authors show a correlation to convective processes and associated gravity waves. Also the reanalysis dataset ERA15 (Gibson et al., 1999) does not show significant spectral



signals for single wave types currently thought to be responsible for the QBO (Tindall, 2003).

There have been a number of 2D mechanistic models (based on the horizontally averaged momentum equations) successful in simulating a QBO-like oscillation but 3D modelling of the QBO has largely been unsuccessful. The reasons are not entirely clear. Nevertheless, QBO-like oscillations in 3D have recently been successfully modelled by (Takahashi, 1999; Giorgetta et al., 2002; Untch, 1998). It appears from these studies, that a successful model of the atmospheric QBO requires sufficient vertical resolution, some “tuning” with respect to horizontal and vertical diffusion parameters and in particular a parametrization or other means to produce a sufficiently broad spectrum of vertically propagating gravity waves. The ECMWF model has apparently lost its ability to successfully model a QBO like oscillation despite recent resolution enhancements. A better understanding of the underlying processes may help to explain this “feature” of the ECMWF model.

Reviewing the current theory of the stratospheric QBO and its numerical realisability one may ask the following questions:

- Where is and what determines the upper and lower boundaries of the QBO in the real atmosphere?
- What is the precise mechanism that dissipates one phase of the QBO near the tropopause and when does the next phase start aloft?
- Which waves drive the QBO in the real atmosphere and how are they generated?
- What is required in global circulation models to reproduce a wave-driven zonal mean zonal flow oscillation like the QBO in the atmosphere?

The last two of above questions have also been addressed in Horinouchi and Yoden (1998) using a simplified “aquaplanet” global circulation model with constant sea surface temperature and parametrized convection.

In this thesis, a direct numerical simulation of the QBO laboratory analogue is employed to resolve the apparent difference in interpretation with respect to the primary cause of the oscillation. In chapter 4 it is demonstrated that the described numerical model is able to reproduce the laboratory results while allowing a detailed analysis of the precise origin of the averaged momentum flux. In analogy to the process of wave transience put forward by Dunkerton (1981), we find that wave-wave interactions, as described in Galmiche et al. (2000), are the chronologically more important primary cause of the zonal mean zonal flow oscillation in the laboratory experiment. Furthermore, a different oscillation mechanism is found than the one originally described by Plumb (Plumb, 1977; Plumb and McEwan, 1978). The simplicity of the laboratory experiment coupled with the exploitation of the available information from the numerical simulations allows further insight into a mechanism that is likely to be responsible also for the atmospheric QBO. It is shown that the laboratory experiment of Plumb and McEwan is primarily driven by wave momentum flux convergence in a critical layer. This result confirms the conclusions

of [Horinouchi and Yoden \(1998\)](#) for the atmospheric QBO, where they find contributing waves primarily similar to the suggestion in [Lindzen and Holton \(1968\)](#) rather than as assumed in [Holton and Lindzen \(1972\)](#). However, here the accuracy of the direct numerical simulation removes the uncertainty with respect to the approximate nature of the model simulation in [Horinouchi and Yoden \(1998\)](#).

## 1.4 Linear internal wave theory of Boussinesq flow

Here the linear theory of waves in a Boussinesq fluid is reviewed. The derivations form a necessary pre-requisite to the new theoretical considerations of sub-chapter 4.5 explaining the arising mean-flow oscillation in the laboratory experiment by non-linear interaction of waves which are solutions of the linearised Boussinesq approximated, Navier-Stokes equations.

A weakly density-stratified, non-rotating, viscous fluid is well approximated by the following Boussinesq equations ([Gill, 1982](#)):

$$\begin{aligned}\nabla \cdot (\rho_0 \mathbf{v}) &= 0, \\ \rho_0 \frac{D\mathbf{v}}{Dt} &= -\nabla p + \rho \mathbf{g} + \nabla \cdot \boldsymbol{\tau}, \\ \frac{D\rho}{Dt} &= \kappa \nabla^2 \rho.\end{aligned}\tag{1.2}$$

Here,  $\nabla$  is the gradient and  $D/Dt \equiv \partial/\partial t + \mathbf{v} \cdot \nabla$  symbolises the material derivative <sup>2</sup>  $\mathbf{v}$  denotes the velocity vector;  $\rho$  and  $p$  denote density and pressure;  $\mathbf{g}$  symbolises the gravity vector;  $\rho_0$  denotes a constant reference density, which is used in the Boussinesq approximation of the equations to linearise the pressure gradient term and to simplify the continuity equation, obtaining an incompressible form;  $\nabla \cdot \boldsymbol{\tau}$  is the divergence of the viscous stress tensor  $\tau_{ij} \propto \nu$  (see appendix for details), with  $\nu$  specifying the kinematic viscosity and  $\kappa$  the diffusivity <sup>3</sup>.

Introducing perturbations around a hydrostatically balanced ambient state  $(\bar{\rho}, \bar{p})$  using

---

<sup>2</sup>Throughout this thesis a material derivative  $D/Dt$  includes the derivatives with respect to space and time of the basis vectors. A total derivative  $d/dt$  is used with fixed (invariant) basis vectors. In the Cartesian framework  $D/Dt \equiv d/dt$ ; in a general, time-dependent coordinate framework in the non-conservation formulation the relation is derived in the appendix ([A.20,A.21](#)).

<sup>3</sup>In the laboratory experiment  $\kappa$  specifies the diffusivity of salt in water, in the atmosphere it specifies the diffusivity of heat in dry air.

the following notations and assumptions

$$\begin{aligned}
u' &:= u - U(z, t) , \\
w' &:= w , \\
\rho' &:= \rho - \bar{\rho}(z) , \\
\pi' &:= \frac{1}{\rho_0}(p - \bar{p}(z)) , \\
b' &:= -\frac{\rho'}{\rho_0}g , \\
N^2 &:= -\frac{g}{\rho_0}\frac{\partial\bar{\rho}}{\partial z} , \\
\frac{\partial\bar{p}}{\partial z} &= -\bar{\rho}g ,
\end{aligned} \tag{1.3}$$

and linearising the equations (1.2) by neglecting products of perturbations, while limiting the analysis to the 2-dimensional x-z plane, one obtains

$$\begin{aligned}
\partial_t U + \partial_t u' + w' \partial_z U + U \partial_x u' &= -\partial_x \pi' + \nu (\partial_x^2 + \partial_z^2) u' + \nu \partial_z^2 U , \\
\partial_t w' + U \partial_x w' &= -\partial_z \pi' + b' + \nu (\partial_x^2 + \partial_z^2) w' , \\
\partial_t b' + N^2 w' &= \kappa (\partial_x^2 + \partial_z^2) b' - U \partial_x b' , \\
\partial_x u' + \partial_z w' &= 0 ,
\end{aligned} \tag{1.4}$$

where  $u'$  and  $w'$  are the perturbations of the horizontal and vertical components of the velocity vector with zonal background flow  $U \equiv U(z, t)$ ;  $\rho', \pi', b'$  denote density, density-normalised pressure and buoyancy perturbations, respectively, and  $N$  is the Brunt-Väisällä frequency.  $\partial_t, \partial_x, \partial_x^n, \partial_z$  and  $\partial_z^n$  symbolise the n-th partial derivatives with respect to  $t, x$ , and  $z$ , respectively. Through successive elimination it is possible to reduce the set of equations (1.4) into a single differential equation for the vertical velocity  $w'$

$$\begin{aligned}
(\partial_t + U \partial_x)^2 \Delta w' + N^2 \partial_x^2 w' - \partial_z^2 U (\partial_t + U \partial_x) \partial_x w' - \partial_t \partial_z^2 U \partial_x w' \\
+ \kappa \partial_x w' \partial_z^4 U + \nu \kappa \Delta^3 w' - (\nu + \kappa) (\partial_t + U \partial_x) \Delta^2 w' = 0,
\end{aligned} \tag{1.5}$$

where  $\Delta \equiv \partial_x^2 + \partial_z^2$  symbolises the Laplacian operator. By introducing the stream function  $\psi$  one can express the velocity components in accord with the continuity equation in (1.2) as

$$\begin{aligned}
u' &= -\frac{\partial\psi}{\partial z} , \\
w' &= \frac{\partial\psi}{\partial x} = ik\psi ,
\end{aligned} \tag{1.6}$$

where the stream function has been postulated as

$$\psi(x, z, t) := \hat{\psi}(z, t) e^{ikx} \tag{1.7}$$

with  $k$  denoting a horizontal wave-number. This assumes the separability of vertical and horizontal motions, which is a common approach in classical normal mode analysis (Daley, 1988; Kasahara, 1974; Phillips, 1990), given a horizontal scale much larger than the vertical scale (Gill, 1982), pp.159.

Inserting relation (1.7) using (1.6) into equation (1.5) leads to the following differential equation, supporting oscillatory (i.e. sinusoidal-like) and non-oscillatory (exponential-like) solutions:

$$\begin{aligned} &(\partial_t + iUk)^2(\partial_z^2 - k^2)\hat{\psi} - N^2k^2\hat{\psi} - ik\partial_z^2U(\partial_t + iUk)\hat{\psi} - ik\hat{\psi}\partial_t\partial_z^2U \\ &+ ik\hat{\psi}\kappa\partial_z^4U + \nu\kappa(\partial_z^2 - k^2)^3\hat{\psi} - (\nu + \kappa)(\partial_t + iUk)(\partial_z^2 - k^2)^2\hat{\psi} = 0. \end{aligned} \quad (1.8)$$

While the complete equation (1.8) may be solved numerically in some time interval given appropriate initial and boundary conditions, it is instructive to consider the following important special cases, which on their own have been subject to intense research (Drazin and Reid, 1981). For example, neglecting stratification,  $N^2 = 0$ , the time dependency of the background flow,  $U = U(z)$  and neglecting higher order terms (i.e.  $\partial_z^4U$  and  $(\partial_z^2 - k^2)^3$ ) one obtains the Orr-Sommerfeld equation, representing an eigenvalue solution of the Navier-Stokes equations for viscous parallel channel flow (a canonical problem for studies of the laminar- turbulent transition in pipe or channel flows)

$$(\partial_t + iUk)(\partial_z^2 - k^2)\hat{\psi} - ik\partial_z^2U\hat{\psi} - (\nu + \kappa)(\partial_z^2 - k^2)^2\hat{\psi} = 0. \quad (1.9)$$

A comprehensive discussion of the solutions can be found in Drazin and Reid (1981) pp.156 and references therein.

With stratification and assuming instead a zero background flow for all time,  $U(t) = 0$ , one obtains

$$(\partial_z^2 - k^2)\partial_t^2\hat{\psi} - N^2k^2\hat{\psi} + \nu\kappa(\partial_z^2 - k^2)^3\hat{\psi} - (\nu + \kappa)(\partial_z^2 - k^2)^2\partial_t\hat{\psi} = 0. \quad (1.10)$$

Given a monochromatic vertical wave structure with wave-number  $m$  and frequency  $\omega$

$$\hat{\psi}(z, t) := \psi_0(z)e^{-i\omega t} = w_0e^{i(mz - \omega t)} \quad (1.11)$$

equation (1.10) can be solved analytically to obtain the simpler dispersion relation

$$\omega^2 - i(\sigma_\kappa + \sigma_\nu)\omega + \sigma^2 + \sigma_\kappa\sigma_\nu = 0, \quad (1.12)$$

with  $\sigma_\nu := \nu(m^2 + k^2)$ ,  $\sigma_\kappa := \kappa(m^2 + k^2)$  and the inviscid Boussinesq dispersion relation (for  $\kappa = \nu = 0$ )

$$\sigma^2 := N^2k^2/(m^2 + k^2). \quad (1.13)$$

The wave frequency  $\omega$  for  $\kappa \neq 0, \nu \neq 0$  can be obtained from equation (1.12)

$$\omega = i\frac{(\sigma_\kappa + \sigma_\nu)}{2} \pm \frac{1}{2}\sqrt{4\sigma^2 - (\sigma_\nu - \sigma_\kappa)^2}. \quad (1.14)$$

Inserting (1.14) into (1.11) shows that viscosity results in an exponential decay of the waves with time

$$\propto e^{-(\sigma_\kappa + \sigma_\nu)t/2} \quad (1.15)$$

and a phase distortion

$$\propto e^{i/2(\sqrt{4\sigma^2 - (\sigma_\nu - \sigma_\kappa)^2})}, \quad (1.16)$$

if  $|\sigma| > |(\sigma_\nu - \sigma_\kappa)/2|$ , which is typically the case for atmospheric applications; see for example [Lignieres \(1999\)](#) for an application with large thermal diffusion as in stellar radiative zones or inside the sun. It should be noted that the indirect effect of viscosity and diffusion on the waves in different regimes can also be destabilising in contrast to the described stabilisation and decay. The effect of viscosity in the QBO analogue will be discussed in more detail in chapter 4.

Another important special case of equation (1.8) is derived by neglecting the influence of viscosity and diffusivity,  $\nu \equiv \kappa \equiv 0$ , and neglecting the time-dependency of the mean flow, but retaining its variation with height,  $U = U(z)$ . The resulting equation

$$(\partial_t + iUk)^2(\partial_z^2 - k^2)\hat{\psi} - N^2k^2\hat{\psi} - ik\partial_z^2U(\partial_t + iUk)\hat{\psi} = 0 \quad (1.17)$$

can be transformed by inserting (1.11) and assuming  $(U - c) \neq 0$ , where  $c := \omega/k$  denotes the wave's horizontal phase speed, to give

$$(U - c)^2 \left[ \partial_z^2 \psi_0 + \underbrace{\left\{ \frac{N^2}{(U - c)^2} - \frac{\partial_z^2 U}{(U - c)} - k^2 \right\}}_{l^2(z)} \psi_0 \right] = 0. \quad (1.18)$$

In comparison, for inviscid Boussinesq flow with constant mean wind  $U = \text{const.}$  one obtains directly from equation (1.17) with (1.13)

$$(\omega + Uk)^2 = \sigma^2. \quad (1.19)$$

Equation (1.18) is often referred to as the Taylor-Goldstein equation ([Drazin and Reid, 1981](#); [Baines, 1995](#)). In the literature on mountain waves  $l^2(z)$  defines the Scorer parameter. The size and sign of the term  $(l^2(z) - k^2)$  determines the behaviour of flows over mountain ridges (see [Smith \(1979\)](#); [Egger and Hoinka \(1992\)](#); [Baines \(1995\)](#); [Leutbecher \(1998\)](#) and references therein for a comprehensive discussion on flows past mountains). Most notably equation (1.18) has a regular singularity when the magnitude of the background flow is equal to the horizontal phase speed,  $(U - c) = 0$ , and when  $\partial_z^2 U \neq 0$  ([Miles, 1961](#)). The height at which the background flow (in the direction of wave propagation) is equal to the horizontal phase speed of the wave, is called a critical level for this wave. Critical level behaviour of monochromatic waves or groups of waves has been elucidated by [Bretherton and Booker \(1966; 1967\)](#). They found that waves are attenuated as they approach a critical level and momentum carried by the waves is transferred to the mean flow at and below that height. The behaviour of a monochromatic wave can be estimated by inserting  $\psi_0 = e^{imz}$

into equation (1.18) and considering the limit  $\epsilon_0 := (U - c) \rightarrow 0$ . Solving for the vertical wave-number  $m$  we obtain the condition

$$m = \pm \lim_{\epsilon_0 \rightarrow 0} \sqrt{\frac{N^2}{\epsilon_0^2} \pm \frac{\partial_z^2 U}{\epsilon_0} - k^2} = \infty, \quad (1.20)$$

which implies a rapidly decaying vertical wave structure  $\psi_0$  as  $(U - c) \rightarrow 0$ . Further theoretical investigations together with laboratory studies have been conducted by (Koop, 1981; Baines, 1995; Teoh et al., 1997). All of these studies typically assume a given constant background shear flow. Another mechanism for wave momentum flux to the mean flow is given through the non-Boussinesq amplification of the waves and subsequent wave breaking (Baines, 1995; Prusa et al., 1996). The mechanisms leading to gravity wave instability and subsequent turbulence is comprehensively reviewed in (Staquet and Sommeria, 2002). The three dimensional propagation of orographic gravity waves into the stratosphere and corresponding wave momentum flux divergences through wave breaking near the tropopause has been discussed in (Leutbecher, 1998). The formation of critical layers in the context of the QBO analogue and details of the related wave-wave and wave-mean flow interaction in this context is discussed in section 4.5.

## 1.5 Wave propagation and the relevance of boundary conditions

The propagation of waves in limited domains is mathematically described by the solution of a set of partial differential equations with appropriate initial and boundary conditions. Many waves can be described as solutions to hyperbolic partial differential equations (Durrant, 1999), thus it is possible to transform into an equivalent system of equations, in which each differential equation contains only differentiations in one ‘‘characteristic’’ direction, see Courant and Hilbert (1989), chapter 5. The hyperbolicity expresses the finiteness of the propagation speed of phenomena governed by such hyperbolic systems (Courant and Hilbert, 1989). It provides, in principle, a complete set of real-valued curves along which a solution may be locally determined given appropriate initial conditions<sup>4</sup>. These curves are called characteristic to the given hyperbolic problem. It is sometimes thought that these characteristics, together with appropriate boundary conditions, provide sufficient information to solve the given initial value problem. However, the standard concept of characteristic curves does not necessarily fully determine the propagation of all admissible waves in the system. In systems with more than one dimension, the lines of constant phase speed or group velocity of some wave disturbances (most notably internal gravity waves and Rossby waves) do not follow the characteristic curves (e.g., the linearised shallow water equations with a Coriolis force, or the Euler equations governing an inviscid, isentropic motion in a density stratified fluid (Durrant, 1999)). This is the case,

<sup>4</sup>Even though the initial data on such characteristic curves cannot be prescribed freely, but must satisfy a compatibility condition, see Courant and Hilbert (1989), chapter 5 for a discussion.

because the physical processes underlying the deviating wave propagation are mathematically represented by zero-order terms in the equations (the Coriolis term or buoyancy in the previous examples), which do not influence the standard determination and shape of the characteristics (see [Durrant \(1999\)](#) for a discussion). Moreover, filtered equations, resulting from approximations with the intent to simplify the system to be solved numerically, or, historically, with the intent to filter certain “un-interesting” (e.g. acoustic) waves, are not hyperbolic in general.

Most physical phenomena of interest take place in a portion of space limited by boundaries ([Courant and Hilbert, 1989](#)). Boundary conditions in numerical simulations are only models of their physical counterparts. The validity of such boundary models has to be evaluated for each given problem. Often the equations are solved in artificially constrained domains to save computational expense, which necessitates the choice of appropriate boundary conditions. In meteorology, vanishing pressure at infinity of the Earth’s atmosphere is often assumed, which results in an increasingly unresolved upper atmosphere given a finite number of discrete model levels. The well-mixed boundary layers in oceanic or global atmospheric models are a challenge due to the inherently different scales of motion that they involve, in contrast to the stratified flow above. It is, however, through the given complexity of the numerical models themselves that an accurate incorporation of boundary conditions is often further complicated. For example, the anelastic set of equations requires the solution of an elliptic equation for pressure and therefore the solution for this part of the model depends “explicitly” on the choice of boundary conditions. In another example, with semi-Lagrangian models there is an open question how to best treat boundaries in complex terrain. The examples, which will be discussed in this section, illustrate that the choice of boundary conditions depends on the physical problem at hand but is often determined by the modelling framework, favouring a particular boundary condition type. The following paragraphs address different boundary conditions used for the numerical modelling of the continuous spectrum of horizontally and vertically propagating atmospheric waves. Some example problems arising from the inappropriate choice of boundary conditions are shown. Specific vertical boundary conditions are discussed to introduce the terminology used in later chapters.

### 1.5.1 Rigid surface

First consider as the bounding surface a fixed rigid surface  $F(x, y, z) = 0$ , either at the top or at the bottom of the fluid — an elementary *rigid lid*. At this type of boundary the normal velocity to the bounding surface is imposed to be zero:

$$\mathbf{v} \cdot \mathbf{n}|_{F(x,y,z)=0} = 0 \quad (1.21)$$

where  $\mathbf{n}$  denotes the local normal to the surface  $F$ . The shape of the bounding surface  $F$  is fixed for all time. In the special case of a horizontally flat surface at the bottom,  $z = 0$ , and at the top,  $z = H_0$ , of the model domain one obtains in Cartesian coordinates

$$w|_{z=0; z=H_0} = 0, \quad (1.22)$$

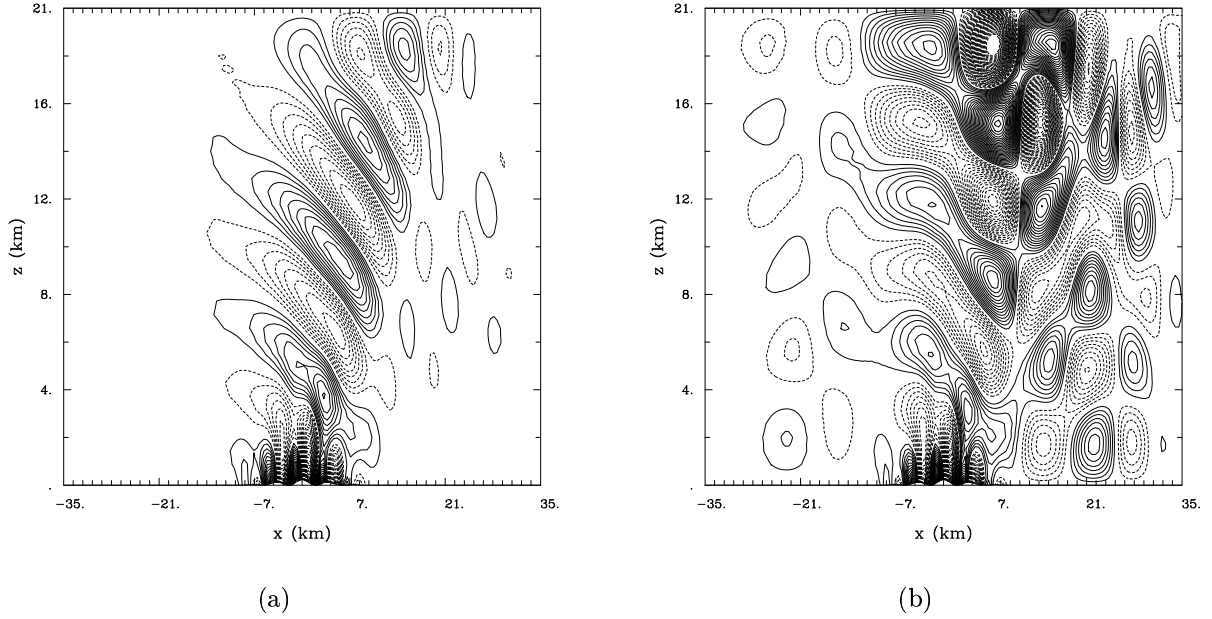


Figure 1.3: An example of fully reflected gravity waves from the top of a computational domain. Plate (a) shows the vertical velocity in a simulation with an absorbing layer starting at 10km height. Plate (b) shows the reflective effect on the vertically propagating gravity waves when the absorption is switched off and the waves reach the rigid lid at the top of the computational domain. The contour interval in both plates is the same as in [Klemp et al. \(2003\)](#),  $0.05 \text{ ms}^{-1}$  (zero contour lines not shown).

where  $w$  is the physical vertical velocity. Propagating waves are reflected from a rigid lid, leading to standing wave patterns as a result of the interference of incident and reflected waves. An example of fully reflected gravity waves in a numerical simulation (see section 3.2 for the details of the computation) with imposed rigid lid boundary conditions is given in figure 1.3.

### 1.5.2 Pliant and free surface

Here, the word “pliant” refers to a moving or time-dependent boundary which bends but does not break. [Baines \(1995\)](#) specifies two conditions for the definition of a *pliant surface*. The first condition marks it as a material (impermeable) interface between two (Boussinesq) fluids, where the lower fluid represents the domain of interest and the upper fluid represents a deep homogenous layer with vanishing vertical velocity at infinity. The impermeability translates into the kinematic condition of no normal flow through the bounding interface  $F$  between the two fluids which can be written as

$$\mathbf{v} \cdot \mathbf{n}|_{F(x,y,z,t)=0} = 0, \quad (1.23)$$



where  $\mathbf{n}$  denotes the normal to the surface  $F$ , which is now time-dependent in contrast to (1.21). The system with a time-dependent boundary may be transformed via a coordinate transformation  $\xi := H_0 z/H$  into a system with rigid boundaries  $\xi = 0$  and  $\xi = H_0$ , where it may be easily shown that the vanishing normal velocity component  $d\xi/dt = 0$  at the upper boundary implies in Cartesian coordinates

$$\left. \frac{dH}{dt} \right|_{z=H(x,y,t)} = w, \quad (1.24)$$

where  $H(x, y, t)$  denotes the height of the interface and  $w$  denotes the vertical velocity. The pliant surface  $F$  may be expressed through  $F := H(x, y, t) - z = 0$ , and since we require the integrity of the surface  $F$  to hold for all time it follows  $dF/dt = 0$  (and vice versa, see Lamb (1975), pp.7 for a proof), which is an equivalent derivation of (1.24) found in the literature. Transforming  $dF/dt$  one finds  $|\nabla F|^{-1} \partial F / \partial t = \mathbf{v} \cdot \mathbf{n}$ , which implies the continuity of the normal velocity components across the interface. Constant pressure at the air sea interface in oceanic flows or potential temperature in adiabatic atmospheric flows may be regarded as idealised material surfaces (ignoring diabatic fluxes, the effects of surface tension and external wind stress). In contrast, pressure surfaces in atmospheric flows are not normally material surfaces.

The second condition of a pliant surface is given by Baines (1995) as the requirement for pressure to be continuous and in the special case of a *free surface* vanishing pressure at the interface. However, this represents only a special case of a more general class of boundary conditions balancing the stresses on either side of the interface (Batchelor, pp.149-150, 1967). In particular the notion of a *free surface* is not clearly defined in the literature and depends on the context (see for example Dutton (1986); Lamb (1975); Batchelor (1967)). The *free surface* boundary is therefore discussed in more detail in the appendix A.1.6, once the tensorial form of the stress in the Navier-Stokes equations has been introduced.

The above material properties are exploited in numerical models of the atmosphere or ocean by defining coordinate surfaces of constant pressure, density or potential temperature since such surfaces follow the adiabatic motion of the fluid at all times. For example in adiabatic atmospheric flows potential temperature, defined as  $\theta \equiv T(p/p_0)^{-R/c_p}$ , is commonly associated with the surface function  $F$  as

$$\frac{dF}{dt} := \frac{d\theta}{dt} = 0, \quad (1.25)$$

which is the thermodynamic equation stating that isentropic surfaces are naturally material surfaces. In the preceding,  $T$  is temperature,  $p_0$  is a constant reference pressure,  $R$  is the gas constant for dry air and  $c_p$  is the specific heat at constant pressure. Alternatively, one could incorporate the height (and its change in time) of these natural material surfaces at the boundaries of the numerical domain in the definition of metric coordinate surfaces. Given the a priori knowledge of such a material surface height in time and space, in the absence of wave breaking and critical layer effects or discontinuities near the boundary, it can be shown that the use of these coordinate surfaces will then naturally not reflect waves

and thus avoid the corruption of the numerical solution through artificial wave reflection. This is demonstrated in this thesis by applying a generalised coordinate transformation.

In pressure coordinate models a *free surface* upper boundary is trivially applied through the assumption  $p \equiv 0$  at infinity. For atmospheric applications constant pressure surfaces are not natural material surfaces (i.e.  $dp/dt \neq 0$ ) other than at infinity where  $p \equiv 0$ . Since numerical models have only a finite number of levels, the atmosphere towards  $p = 0$  is only poorly resolved. As a result some upward propagating waves may be obscured for numerical reasons since the undulation of the bounding material surface does not exactly follow the flow. Furthermore, the free-surface concept is strictly valid only in the absence of diabatic forcings.

Figure 1.4 shows an example of a flow past the Scandinavian peninsula simulated by the hybrid coordinate model of ECMWF (Simmons and Burridge, 1981; Temperton et al., 2001) with pure pressure levels in the top 23 layers with formally  $p = 0$  at infinity. Some larger scale standing wave patterns can be seen, which extend in some parts quite far down into the model domain. These patterns form through interference of incoming waves and waves reflected at the upper boundary.

A *free-surface*, characterised by above kinematic condition of no normal flow (1.23) and a dynamic condition utilising pressure continuity across the boundary, supports fast propagating surface gravity waves. In ocean models, it typically adds an additional prognostic equation for the surface height which is implicit with respect to the advecting velocities (Namin et al., 2001). Both aspects, the implicitness and the fast propagation speed render free surfaces a challenging problem in oceanic (Madala and Piacsek, 1977; Higdon, 2002; Iskandarani et al., 2003) and in engineering flows (Casulli and Cheng, 1992; Casulli, 1999; Namin et al., 2001). In sub-chapter 3.3 of this thesis an alternative incorporation of free surfaces is discussed that avoids the numerical limitation of fast propagating surface gravity waves.

### 1.5.3 Free-slip and no-slip velocity boundary conditions

In the context of boundaries for the inviscid or viscous numerical formulations of the Euler or Navier-Stokes equations the terminology of *free-slip* and *no-slip* boundary conditions is often used. These refer to explicit boundary conditions on the velocity components tangential to the bounding surface. The physical constraint of assuming no tangential deviatoric stresses (the stress tensor without the normal pressure force) at the boundary is called the *free-slip* boundary condition. In inviscid formulations there is zero deviatoric stress by definition everywhere in the fluid including at the boundary. Therefore, inviscid formulations are always associated with *free-slip* boundaries.

The physical effects of boundary layers, the effect of viscosity and the generation of turbulence near boundaries has been investigated extensively by Prandtl (Prandtl, 1961). For a viscous fluid, fluid-wall particle interactions are at least as strong as fluid-fluid particle interactions and, as a result, the fluid's velocity field is assumed continuous at the boundary. This physically motivated assumption translates into the *no-slip* velocity boundary condition of the continuity of the tangential velocity component at the fluid-solid interface

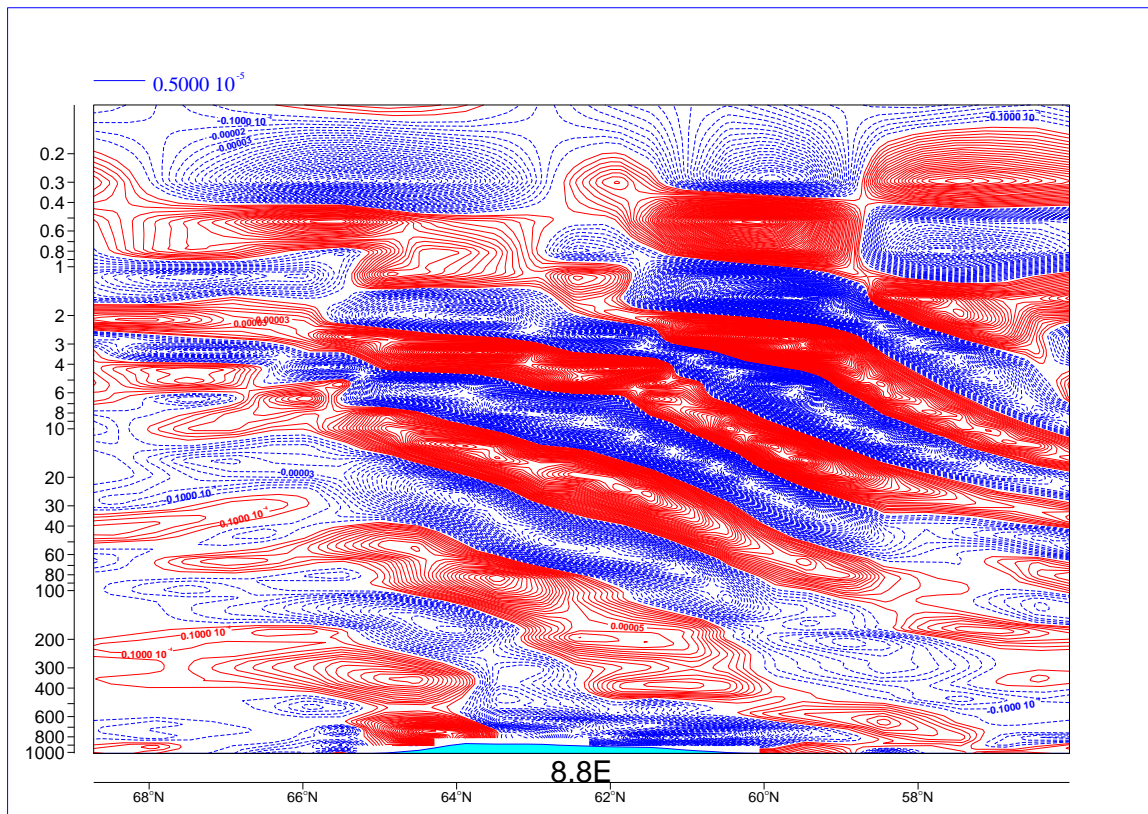


Figure 1.4: Example of gravity wave reflection from the model top in the ECMWF forecast model. The figure shows the divergence of the velocity field in a north-westerly flow over the Scandinavian peninsula on March 17th 1998 after 60 hours of simulation. The model uses pure pressure levels in the top 23 layers with formally  $p = 0$  at infinity.

(Batchelor, 1967), pp.149. Note, that the continuity of the normal component of velocity resulted from the material surface property. This gives  $v = const$  or zero at the boundary, which effectively defines the deviatoric stress there. However, viscous fluid flows are not always associated with no-slip conditions (in contrast to inviscid and free-slip). A viscous fluid may be held in place by something other than a rigid wall (for example, gravity). In such cases, it is reasonable to assume that the fluid has zero tangential deviatoric stresses at that boundary, ie. a *free-slip* condition applies. This is for example the case at an idealised (surface tension ignored) *free surface*, where the tangential deviatoric stress is assumed zero and the normal component of the stress (ie. pressure) is constant.

The boundary conditions are related to the creation of vorticity in a fluid (Wu and Wu, 1998). In Helmholtz' vorticity equation for an incompressible homogeneous fluid there are no true generation terms for vorticity and sources of vorticity must lie in the boundaries (Morton, 1984; Greiner and Stock, 1991). It is the *no-slip* condition that provides a mechanism for vorticity production at a rigid boundary (Batchelor, pp.277, 1967). Batchelor also describes the generation of a boundary layer at a free surface of a viscous fluid resulting

from the particular free surface boundary conditions (Batchelor, pp.364, 1967). Baroclinicity, i.e.  $\nabla\rho\times\nabla p\neq 0$ , and associated nonlinear surface accelerations at free surfaces provide another source for vorticity (Rotunno and Smolarkiewicz, 1995; Wu and Wu, 1998). In inviscid simulations the condition of zero tangential deviatoric stress at the boundary may be used to analyse the accuracy of the numerical implementation by examining spurious vorticity production at the boundary (see Morton (1984) for a discussion).

Atmospheric models typically solve an averaged set of (inviscid) equations and parametrize the boundary layer effects (of the original viscous problem) by means of a frictional drag coefficient, which acts over some given timescale. Furthermore, since there are no side walls in global atmospheric flows, this eliminates the need for explicit tangential velocity boundary conditions in the adiabatic part of such a numerical model.

#### 1.5.4 “Infinite depth”

Often a simple (flat) upper boundary shape is assumed at which its reflective effects are diluted by carefully designed dissipative layers below. Such dissipation of upward propagating wave energy might arguably happen naturally near the top of the mesosphere as a result of high altitude wave breaking, where the flow due to the low density is effectively described by Stokes flow (Prusa et al., 1996). One technique is to use *wave absorbing layers* (“sponge”), where multiple computational layers are added to the model domain together with frictional or viscous damping terms, which are added to the equations within those layers. If the model domain reaches high enough the addition of those terms may have a physical meaning. However, in many applications *wave absorbing layers* require an engineering effort for each specific problem to ensure the effectiveness of the absorbing layer. In general the addition of diffusive terms ( $\propto\nabla^2\psi$ ) for an arbitrary prognostic variable  $\psi$  is scale selective since the diffusion may only be applied to a part of the wave spectrum. In contrast an additional Rayleigh friction term ( $\propto\alpha\psi$ ) will damp all waves equally. In global atmospheric models like the ECMWF model, Rayleigh friction is often applied for a different reason. It is applied only on the zonal mean zonal wind part of the flow (spectrally, wave number 0) to simulate the physical (unresolved) process of large scale high altitude wave-breaking and subsequent slowing of the mean flow. The absorbing effect of applying Rayleigh damping on the perturbations in an idealised flow simulation can be seen in the left panel of figure 1.3. The absorbing (scale selective) effect of applying an increased horizontal diffusion in the uppermost layers of the ECMWF forecast model can be seen by comparing figure 1.4 with figure 1.5.

An alternative technique utilises *radiation boundary conditions* ensuring an outward directed wave energy flux. The applicability, as before, depends on the investigated problem since reflections or inward travelling wave disturbances may be part of the solution. A review of radiation boundary conditions is given in Givoli (1991). For implementations of radiative boundary conditions in meteorology see Klemp and Durran (1983); Bougeault (1983); Herzog (1995). These are strictly valid only for the linearised Boussinesq system for which they were derived. However, the authors show their utility beyond the Boussinesq framework. This approach has a strong computational advantage over the previous class

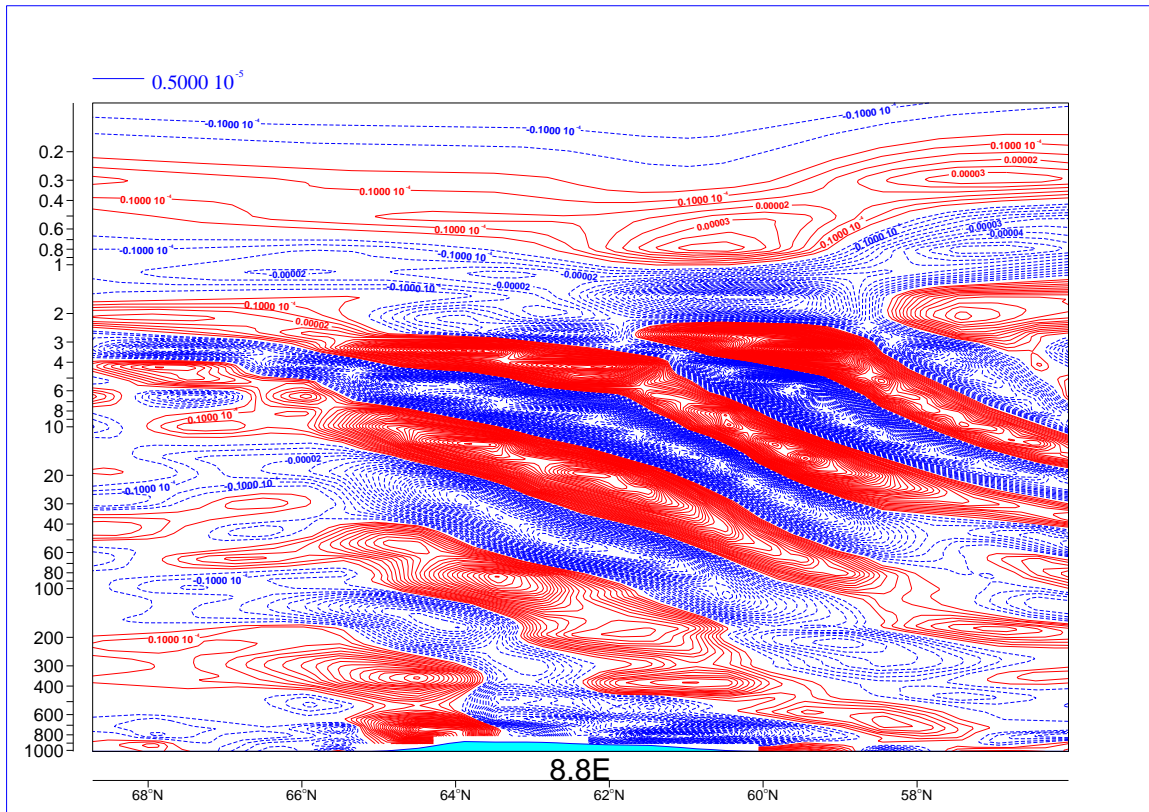


Figure 1.5: Example of (artificial) wave absorption at the model top in the operational ECMWF forecast model. Compare to figure 1.4 where horizontal diffusion is not enhanced in the uppermost layers. In both cases some reflectivity effects remain.

of boundary conditions since it avoids the domain extension of sometimes many more additional computational layers.

It may also be possible to combine the approaches described in section 1.5.4 and section 1.5.2 to appropriately address a spectrum of waves.

## 1.6 Methodology and thesis questions

The introduction addressed issues arising from the numerical modelling of internal waves and their interactions with each other or with a background flow, and interactions with various artificial or natural boundary representations and forcings relevant to many areas of atmospheric and oceanic flows. This thesis seeks a better understanding of such interactions and develops a theoretical and numerical framework to aid the adaptation of numerical algorithms to time-dependent boundaries. Furthermore, this thesis investigates the mechanism of the QBO and its numerical realisability, which represents a particular challenging case in the class of problems with time-dependent (boundary) forcings.

In the first part of this thesis a unified framework is developed for investigating the influence of different upper boundaries on atmospheric and oceanic flows. Central to this new development is the analytical derivation and the numerically efficient implementation of the generalised time-dependent Gal-Chen coordinate transformation described in chapter 2. Subsequently, the correctness of implementation and theory is verified with selected examples of applications in two and three dimensions. A first practical result of the development provides an alternative for incorporating a finite-amplitude free surface upper boundary in ocean models.

In the second part of this thesis this framework is used in the direct numerical simulation of the quasi-biennial oscillation (QBO) analogue. The ability of the newly developed coordinate transformation is utilised to accommodate intricate geometric, time-dependent boundary forcings, either at the top or at the bottom of the model domain. The linear theory of internal waves, reviewed in section 1.4, facilitates a theoretical analysis of the numerical results presented in chapter 4. These findings provide new insights into the mechanism of the quasi-biennial oscillation and may facilitate the numerical realisability in weather prediction and climate simulations, which currently fail to simulate the QBO satisfactorily. Some implications for atmospheric equatorial zonal mean zonal flow oscillations are discussed in chapter 5.

# Chapter 2

## Modelling framework

### 2.1 Model summary

The explicit solution of the generic fully compressible equations is prohibitively expensive for many applications. As a result, numerical models employ either split-explicit or semi-implicit solution procedures, or the equations are simplified beforehand by a variety of analytic approximations (e.g. hydrostatic, elastic, anelastic, or Boussinesq approximations) justified on the basis of scale analysis or based on the physicality of the problem.

In the following a viscous, adiabatic, density-stratified fluid is discussed whose undisturbed, balanced ambient (or environmental) state is described by the potential temperature  $\theta_e = \theta_e(\mathbf{x})$ <sup>1</sup> and the velocity  $\mathbf{v}_e = \mathbf{v}_e(\mathbf{x})$  using the anelastic approximation (e.g. (Lipps and Hemler, 1982)). This approximation extends the previously used Boussinesq formulation of equation (1.2) by allowing for a vertically varying reference state  $\rho_b(z)$ ,  $\theta_b(z)$ . In comparison to the general fully compressible equations, it linearises the pressure gradient term in the momentum equation and maintains the incompressible character of the continuity equation which is advantageous for the numerical formulation. A comprehensive discussion of the anelastic model can be found in Prusa and Smolarkiewicz (2003) and references therein. To facilitate the distinction between physical aspects of the anelastic system versus mathematical aspects of the transformation, it is started with a compact, symbolic vector-form of the anelastic equations (Lipps and Hemler, 1982)

$$\begin{aligned}\nabla \cdot (\rho_b \mathbf{v}) &= 0 , \\ \frac{D\mathbf{v}}{Dt} &= -\nabla \pi' - \mathbf{g} \frac{\theta'}{\theta_b} + \mathbf{F} + \mathcal{V} , \\ \frac{D\theta'}{Dt} &= -\mathbf{v} \cdot \nabla \theta_e + \mathcal{H} .\end{aligned}\tag{2.1}$$

Here, the operators  $D/Dt$ ,  $\nabla$ , and  $\nabla \cdot$  symbolise the material derivative, gradient, and divergence;  $\mathbf{v}$  denotes the velocity vector;  $\mathbf{F}$  symbolises inertial forces (e.g., Coriolis and met-

---

<sup>1</sup>Near equation (1.25) potential temperature is defined.

ric forces of the geo-spherical physical system, cf. [Smolarkiewicz et al. \(1999\)](#)<sup>2</sup>, whereas  $\mathcal{V}$  and  $\mathcal{H}$  symbolise viscous dissipation of momentum and diffusion of heat, respectively;  $\theta$ ,  $\rho$ , and  $\pi$  denote potential temperature, density, and a density-normalised pressure; and  $\mathbf{g}$  symbolises the gravity vector. Primes denote deviations from the environmental state. The subscript  $_b$  refers to the basic state, i.e., a horizontally homogeneous hydrostatic reference state of the Boussinesq expansion around a constant stability profile (see section 2a in [Clark and Farley \(1984\)](#), for a discussion).

The time-dependent coordinate transformation is embedded into the theoretical framework of [Prusa and Smolarkiewicz \(2003\)](#), where the authors considered a general three dimensional, time-variable homeomorphic mapping from a physical system<sup>3</sup>  $(t, \mathbf{x})$  to an arbitrary system  $(\bar{t}, \bar{\mathbf{x}})$

$$(\bar{t}, \bar{x}, \bar{y}, \bar{z}) \equiv ( t, E(x, y, t), D(x, y, t), C(x, y, z, t) ) . \quad (2.2)$$

Since  $(\bar{x}, \bar{y})$  do not depend upon the vertical coordinate  $z$  — preserving the primary hydrostatic structure of atmospheres and oceans, and simplifying the metric terms — the development of a particular  $C(x, y, z, t)$  readily applies and is described in detail in section 2.2.

Given (2.2), the symbolic vector-form equations (2.1) can be expressed as

$$\begin{aligned} \frac{\partial(\rho^* \bar{v}^{s^k})}{\partial \bar{x}^k} &= 0 , \\ \frac{d\bar{v}^j}{d\bar{t}} &= - \tilde{G}_j^k \frac{\partial \pi'}{\partial \bar{x}^k} + g \frac{\theta'}{\theta_b} \delta_3^j + F^j + \mathcal{V}^j , \\ \frac{d\theta'}{d\bar{t}} &= - \bar{v}^{s^k} \frac{\partial \theta_e}{\partial \bar{x}^k} + \mathcal{H} . \end{aligned} \quad (2.3)$$

Here,  $\rho^* := \rho_b \bar{G}$ , with  $\bar{G}$  denoting the Jacobian of the transformation, and  $j, k = 1, 2, 3$  correspond to the  $\bar{x}, \bar{y}, \bar{z}$  components, respectively. Summation is implied by repeated indices, unless stated otherwise. On the right hand side of the momentum equation,  $\tilde{G}_j^k := \sqrt{g^{jj}} (\partial \bar{x}^k / \partial x^j)$  are renormalised elements of the Jacobian (summation not implied over  $j$ ); the coefficients  $g^{jj}$  are the diagonal elements of the conjugate metric tensor of the (not necessarily Cartesian) physical system  $(t, \mathbf{x})$  (see appendix A.1.5 for an example),<sup>4</sup> and  $\delta_3^j$  is the Kronecker delta. The transformation coefficients  $\tilde{G}_j^k \neq \tilde{G}_k^j$  are not to be confused with the elements of the metric tensor of the transformation  $\bar{g}^{jk} = \bar{g}^{kj} = g^{pq} (\partial \bar{x}^k / \partial x^p) (\partial \bar{x}^j / \partial x^q)$  with  $\bar{G} = |\bar{g}^{jk}|^{-1/2}$ . The scalar diffusion of heat is computed as  $\mathcal{H} = 1/\rho^* \partial / \partial \bar{x}^j (\kappa \rho^* \bar{g}^{jk} \partial \theta' / \partial \bar{x}^k)$ . The expression for the viscous terms  $\mathcal{V}$  is given in the appendix. Furthermore, three different representations of velocity appear in (2.3). In the

<sup>2</sup>In general,  $\mathbf{F}$  may also include external forcings.

<sup>3</sup>Only curvilinear coordinate descriptions of a flat (locally Lorentz) space with a zero Riemann curvature tensor are considered.

<sup>4</sup>In general the components of the conjugate metric tensor follow from the definition of the fundamental metric  $ds^2 = g_{pq} dx^p dx^q$  and the linear system  $g_{pk} g^{kq} \equiv \delta_p^q$ , cf. [Prusa and Smolarkiewicz \(2003\)](#).



total derivative  $d/d\bar{t} = \partial/\partial\bar{t} + \bar{v}^{*k}(\partial/\partial\bar{x}^k)$ , the *contravariant velocity*  $\bar{v}^*$  is used

$$\bar{v}^{*k} := d\bar{x}^k/d\bar{t} := \dot{\bar{x}}^k ; \quad (2.4)$$

whereas on the left hand side of the momentum equation, the *physical velocity*  $v^j$ , specified in the physical system  $(t, \mathbf{x})$ , is advected by  $\bar{v}^{*k}$ . The *solenoidal velocity* appearing in the mass continuity and potential temperature equations is given as

$$\bar{v}^{sk} := \bar{v}^{*k} - \frac{\partial\bar{x}^k}{\partial t}, \quad (2.5)$$

with the name originating from the form the continuity equation takes with it. The relations, allowing to express each velocity (solenoidal, contravariant, or physical) in terms of the others, have been discussed in Prusa and Smolarkiewicz (2003). The two relations important for the numerical solution procedure are (2.5) and

$$\bar{v}^{sj} = \tilde{G}_n^j v^n . \quad (2.6)$$

The simultaneous use of the contravariant and the physical velocity eliminates Christoffel terms of the transformation (proportional to products of contravariant velocity components) from the momentum equation; the use of the solenoidal velocity is advantageous in the formulation of the elliptic pressure equation (Prusa et al., 2001).

## 2.2 Generalised Gal-Chen & Somerville vertical coordinate

Starting from the physical system  $(t, \mathbf{x})$ , the general dependence of  $\bar{z}$  on  $(x, y, z, t)$  in (2.2) is collapsed into a similarity transformation

$$\begin{aligned} \bar{z} &= C(\xi) \\ \xi &= \xi(x, y, z, t) := H_0 \frac{z - z_s(x, y, t)}{H(x, y, t) - z_s(x, y, t)}, \end{aligned} \quad (2.7)$$

with the inverse relationship

$$\begin{aligned} z &= \frac{\xi}{H_0}(H - z_s) + z_s, \\ \xi &= C^{-1}(\bar{z}). \end{aligned} \quad (2.8)$$

The functions  $z_s(x, y, t)$  and  $H(x, y, t)$  denote horizontally and time varying lower and upper boundaries in the physical system. The function  $C$  conveniently admits a class of vertically stretched coordinates. In particular, it enables the simulation of the vertical coordinate spacing of pressure or sigma levels (Smolarkiewicz et al., 2001), common in atmospheric or oceanic applications. The transformation in (2.7) retains the computational

advantage of separability into one- and two-dimensional fields. In particular, the Jacobian of the transformation is given as

$$\begin{aligned}\bar{G} &= \left( \frac{dC}{d\xi} \frac{\partial \xi}{\partial z} \right)^{-1} \left( \frac{\partial E}{\partial x} \frac{\partial D}{\partial y} - \frac{\partial E}{\partial y} \frac{\partial D}{\partial x} \right)^{-1} \\ &\equiv \left( \frac{dC}{d\xi} \right)^{-1} \bar{G}_0 \bar{G}_{xy},\end{aligned}\quad (2.9)$$

with

$$\bar{G}_0 \equiv \left( \frac{\partial \xi}{\partial z} \right)^{-1} = \frac{H(x, y, t) - z_s(x, y, t)}{H_0} \quad (2.10)$$

reminiscent of the original Gal-Chen & Somerville Jacobian

$$\bar{G}_0 = \frac{H_0 - z_s(x, y)}{H_0} \quad (2.11)$$

with constant upper boundary and stationary lower boundary.

The transformation coefficients  $\tilde{G}_j^k$  — defined following (2.3) — affected by the vertical transformation (2.7) are

$$\begin{aligned}\tilde{G}_1^3 &= \sqrt{g^{11}} \frac{dC}{d\xi} \frac{\partial \xi}{\partial x}, \\ \tilde{G}_2^3 &= \sqrt{g^{22}} \frac{dC}{d\xi} \frac{\partial \xi}{\partial y}, \\ \tilde{G}_3^3 &= \sqrt{g^{33}} \frac{dC}{d\xi} \frac{\partial \xi}{\partial z},\end{aligned}\quad (2.12)$$

where

$$\begin{aligned}\frac{\partial \xi}{\partial x} &= \frac{1}{\bar{G}_0} \left[ \frac{\partial z_s}{\partial x} \left( \frac{z - H}{H - z_s} \right) - \frac{\partial H}{\partial x} \left( \frac{z - z_s}{H - z_s} \right) \right], \\ \frac{\partial \xi}{\partial y} &= \frac{1}{\bar{G}_0} \left[ \frac{\partial z_s}{\partial y} \left( \frac{z - H}{H - z_s} \right) - \frac{\partial H}{\partial y} \left( \frac{z - z_s}{H - z_s} \right) \right], \\ \frac{\partial \xi}{\partial z} &= \frac{1}{\bar{G}_0}.\end{aligned}\quad (2.13)$$

To solve the governing equations (2.3) in the transformed space, the coefficients  $\tilde{G}_j^k$  must be expressed as functions of  $(\bar{t}, \bar{\mathbf{x}})$ . In numerical models using the Gal-Chen & Somerville transformation, the coefficients (2.13) are typically evaluated using a direct differentiation of  $z_s(x, y)$ . From experience, however, an alternative approach, tailored to the numerical differentiation of  $\bar{G}_0$ , has been found computationally beneficial (e.g., for minimising spurious vorticity generation at free-slip boundaries (Prusa and Smolarkiewicz, 2003;

(Smolarkiewicz and Prusa, 2004)). The following expressions are defined as

$$\begin{aligned}
h_{13} &:= \frac{1}{\overline{G}_0} \frac{\partial H}{\partial x} = \left[ \frac{1}{\overline{G}_0} \frac{\partial H}{\partial \bar{x}} \right] \frac{\partial E}{\partial x} + \left[ \frac{1}{\overline{G}_0} \frac{\partial H}{\partial \bar{y}} \right] \frac{\partial D}{\partial x}, \\
h_{23} &:= \frac{1}{\overline{G}_0} \frac{\partial H}{\partial y} = \left[ \frac{1}{\overline{G}_0} \frac{\partial H}{\partial \bar{x}} \right] \frac{\partial E}{\partial y} + \left[ \frac{1}{\overline{G}_0} \frac{\partial H}{\partial \bar{y}} \right] \frac{\partial D}{\partial y}, \\
s_{13} &:= \frac{1}{\overline{G}_0} \frac{\partial \overline{G}_0}{\partial x} = \left[ \frac{1}{\overline{G}_0} \frac{\partial \overline{G}_0}{\partial \bar{x}} \right] \frac{\partial E}{\partial x} + \left[ \frac{1}{\overline{G}_0} \frac{\partial \overline{G}_0}{\partial \bar{y}} \right] \frac{\partial D}{\partial x}, \\
s_{23} &:= \frac{1}{\overline{G}_0} \frac{\partial \overline{G}_0}{\partial y} = \left[ \frac{1}{\overline{G}_0} \frac{\partial \overline{G}_0}{\partial \bar{x}} \right] \frac{\partial E}{\partial y} + \left[ \frac{1}{\overline{G}_0} \frac{\partial \overline{G}_0}{\partial \bar{y}} \right] \frac{\partial D}{\partial y}.
\end{aligned} \tag{2.14}$$

The formulae in (2.14) are written as implemented in the numerical model described in section 2.3, with the  $[ ]$  terms referring to the numerical differentiation.<sup>5</sup> Second, note that the definition of  $\overline{G}_0$  in (2.11) implies

$$\begin{aligned}
\frac{1}{\overline{G}_0} \frac{\partial \overline{G}_0}{\partial x} &= \frac{1}{H - z_s} \left( \frac{\partial H}{\partial x} - \frac{\partial z_s}{\partial x} \right), \\
\frac{1}{\overline{G}_0} \frac{\partial \overline{G}_0}{\partial y} &= \frac{1}{H - z_s} \left( \frac{\partial H}{\partial y} - \frac{\partial z_s}{\partial y} \right), \\
\frac{1}{\overline{G}_0} \frac{\partial \overline{G}_0}{\partial t} &= \frac{1}{H - z_s} \left( \frac{\partial H}{\partial t} - \frac{\partial z_s}{\partial t} \right).
\end{aligned} \tag{2.15}$$

Manipulating (2.13), (2.15), and the definitions (2.14), the coefficients (2.12) are expressed solely in  $(\bar{t}, \bar{\mathbf{x}})$

$$\begin{aligned}
\tilde{G}_1^3 &= \sqrt{g^{11}} \frac{dC}{d\xi} [s_{13} (H_0 - C^{-1}(\bar{z})) - h_{13}], \\
\tilde{G}_2^3 &= \sqrt{g^{22}} \frac{dC}{d\xi} [s_{23} (H_0 - C^{-1}(\bar{z})) - h_{23}], \\
\tilde{G}_3^3 &= \sqrt{g^{33}} \frac{dC}{d\xi} \frac{1}{\overline{G}_0}.
\end{aligned} \tag{2.16}$$

The *kinematic boundary condition* at an impermeable (e.g. material) surface (at the top,  $dH/dt = w$ , or at the bottom boundary,  $dz_s/dt = w$ ; cf. Lamb (1975)) follows from  $\dot{\bar{x}}^3 \equiv 0$  in (2.4), hence specifying the boundary conditions for the solenoidal velocity defined in (2.5). Given all transformation coefficients and  $\partial \bar{x}^k / \partial t$  expressed in transformed coordinates, the solenoidal velocity components are readily determined from (2.6), while the contravariant velocity components  $\bar{v}^{*j}$  defined in (2.4) are determined from (2.5). Manipulating the third relationship in (2.15), the inverse transformation (2.8), and the definition

<sup>5</sup>The elements of the Jacobi matrix  $\partial(E, D)/\partial(x, y)$  are evaluated in  $(\bar{t}, \bar{\mathbf{x}})$  by computing the inverse of the Jacobi matrix  $\partial(x, y)/\partial(\bar{x}, \bar{y})$ .

of  $\bar{G}_0$  in (2.11), the derivative

$$\frac{\partial \xi}{\partial t} = \frac{1}{\bar{G}_0} \left[ \frac{\partial z_s}{\partial t} \left( \frac{z - H}{H - z_s} \right) - \frac{\partial H}{\partial t} \left( \frac{z - z_s}{H - z_s} \right) \right] \quad (2.17)$$

is expressed in  $(\bar{t}, \bar{\mathbf{x}})$

$$\frac{\partial \xi}{\partial t} = \frac{1}{\bar{G}_0} \frac{\partial \bar{G}_0}{\partial t} (H_0 - C^{-1}(\bar{z})) - \frac{1}{\bar{G}_0} \frac{\partial H}{\partial t}, \quad (2.18)$$

leading to the following expression of the boundary conditions for the solenoidal velocity

$$\left\{ \frac{1}{v^{s3}} = -\frac{dC}{d\xi} \left[ \frac{1}{\bar{G}_0} \frac{\partial \bar{G}_0}{\partial t} (H_0 - C^{-1}(\bar{z})) - \frac{1}{\bar{G}_0} \frac{\partial H}{\partial t} \right] \right\}_{\bar{z}=0, H_0}. \quad (2.19)$$

For non-trivial horizontal transformations, the Jacobian (2.9) and all relations in (2.12-2.16) contain multiplicative factors that are only functions of  $(\bar{x}, \bar{y}, \bar{t})$ , uniquely determined from  $\bar{x} = E(x, y, t)$  and  $\bar{y} = D(x, y, t)$ . In Prusa and Smolarkiewicz (2003) the authors focused on horizontal transformations for mesh adaptivity. Throughout this thesis the identity transformation is assumed in the horizontal,  $\bar{x} \equiv x$  and  $\bar{y} \equiv y$ , since it does not compromise the generality of the approach (2.2) while stressing the utility of the generalised Gal-Chen & Somerville vertical coordinate in (2.7). Furthermore, the stretching function  $C(\xi)$  is taken as the identity in the examples. Consequently,  $\tilde{G}_1^2 = \tilde{G}_2^1 = \tilde{G}_3^1 = \tilde{G}_3^2 = 0$  and  $\tilde{G}_1^1 = \tilde{G}_2^2 = 1$ , while  $h_{ij}$  and  $s_{ij}$  are simplified accordingly.

### 2.3 The numerical approximation

The nonhydrostatic anelastic equations (2.3) are solved numerically using a second-order-accurate nonoscillatory forward-in-time (NFT) approach (Smolarkiewicz and Margolin, 1993). “Nonoscillatory” refers to monotone schemes, e.g. total variation diminishing (TVD), flux-corrected transport (FCT), and various flux-limited and sign-preserving schemes, that suppress/reduce/control numerical oscillations characteristic of higher order linear schemes (Smolarkiewicz and Prusa, 2002; Durran, 1999). “Forward-in-time” labels a class of generalised Lax-Wendroff<sup>6</sup> type methods (Tremback et al., 1987; Smolarkiewicz and Prusa, 2002). Below it is briefly commented on the essential aspects of the numerical solution procedure while referring the reader to earlier works for further details.

The prognostic equations in (2.3) can be written in a compact conservation-law form

$$\frac{\partial \rho^* \psi}{\partial \bar{t}} + \bar{\nabla} \cdot (\rho^* \bar{\mathbf{v}}^* \psi) = \rho^* R, \quad (2.20)$$

<sup>6</sup> Taylor series are used to develop the finite-difference scheme.

where  $\bar{\nabla} := (\partial/\partial\bar{x}, \partial/\partial\bar{y}, \partial/\partial\bar{z})$ , and  $\psi$  symbolises a velocity component or potential temperature. In (2.20),  $R$  summarises the right hand side of the equations in (2.3). Alternatively, the same prognostic equations can be cast in Lagrangian form

$$\frac{d\psi}{d\bar{t}} = R. \quad (2.21)$$

On a discrete mesh, the NFT approximation of either formulation — flux-form Eulerian (Smolarkiewicz and Margolin, 1993) for (2.20), or semi-Lagrangian (Smolarkiewicz and Pudykiewicz, 1992) for (2.21) — can be written compactly as

$$\psi_{\mathbf{i}}^{n+1} = LE_{\mathbf{i}}(\tilde{\psi}) + 0.5\Delta t R_{\mathbf{i}}^{n+1}. \quad (2.22)$$

Here,  $\psi_{\mathbf{i}}^{n+1}$  denotes the solution at the grid point  $(\bar{t}^{n+1}, \bar{\mathbf{x}}_{\mathbf{i}})$ ;  $\tilde{\psi} := \psi^n + 0.5\Delta t R^n$ ; and  $LE$  denotes a NFT transport operator. In the Eulerian scheme,  $LE$  integrates the homogeneous transport equation (2.20), i.e.,  $LE$  advects  $\tilde{\psi}$  using a fully second-order-accurate MPDATA scheme (multidimensional positive definite advection transport algorithm) (Smolarkiewicz and Margolin, 1998; Smolarkiewicz and Prusa, 2002). In the semi-Lagrangian algorithm,  $LE$  remaps transported fields, which arrive at the grid points  $(\bar{t}, \bar{\mathbf{x}}_{\mathbf{i}})$ , to the departure points of the flow trajectories  $(\bar{t}^n, \bar{\mathbf{x}}_o(\bar{t}^{n+1}, \bar{\mathbf{x}}_{\mathbf{i}}))$  also using MPDATA type advection schemes (Smolarkiewicz and Grell, 1992; Smolarkiewicz and Pudykiewicz, 1992). MPDATA is a finite-difference algorithm for approximating the advective terms in fluid equations. The solution procedure of MPDATA is iterative with a first pass using a simple donor cell approximation which is positive definite but only first order accurate. In one dimension equation (2.20) (assuming  $R = 0$ ,  $\rho^* = 1$  for simplicity) takes the form

$$\psi_i^{n+1} = \psi_i^n - [F(\psi_i^n, \psi_{i+1}^n, \mathcal{C}_{i+1/2}) - F(\psi_{i-1}^n, \psi_i^n, \mathcal{C}_{i-1/2})], \quad (2.23)$$

where the flux function  $F$  is defined in terms of the local Courant number  $\mathcal{C} \equiv u\Delta t/\Delta x$  by

$$F(\psi_L, \psi_R, \mathcal{C}) \equiv [\mathcal{C}]^+ \psi_L + [\mathcal{C}]^- \psi_R, \quad (2.24)$$

with  $[\mathcal{C}]^+ \equiv 0.5(\mathcal{C} + |\mathcal{C}|)$  and  $[\mathcal{C}]^- \equiv 0.5(\mathcal{C} - |\mathcal{C}|)$ . The second pass increases the accuracy by estimating and compensating the truncation error of the first pass to higher order. The scheme is reapplied using antidiffusive advective velocities, which are derived analytically from the advected field, and based on the truncation error analysis of the donor cell scheme (Smolarkiewicz and Margolin, 1998).

The overall model algorithm (2.22) represents a system of equations implicit with respect to all dependent variables in (2.3), since all forcings  $R_{\mathbf{i}}^{n+1}$  are assumed to be unknown at  $n+1$ . For the potential temperature equation, the right hand side includes the complete convective derivative, ensuring an adequate treatment of the impermeability condition at the lower boundary and the conservation of  $\theta'$ , regardless of details of the transformation (2.2) (see Smolarkiewicz et al. (2001), for discussions). The implicitness of the pressure gradient forces in the numerical approximation of the momentum equation conveniently enables the projection of preliminary values  $LE(\tilde{\psi})$  in (2.22) to solutions of the continuity

equation in (2.3). First, the system of simultaneous equations resulting from (2.22) is algebraically inverted to construct expressions for the discrete solenoidal velocity components using (2.6). Then, the resulting solenoidal velocity is substituted in the discrete form of the mass continuity equation in (2.3), forming an elliptic equation for pressure (see Appendix A in Prusa and Smolarkiewicz (2003) for the complete development). The elliptic pressure equation is solved (stressing the need for appropriate boundary conditions) using the generalised conjugate-residual approach — a preconditioned nonsymmetric Krylov-subspace solver (Smolarkiewicz and Margolin, 1994, 1997; Skamarock et al., 1997). Given the updated pressure, and hence the updated solenoidal velocity, the updated physical and contravariant velocity components are constructed from the solenoidal velocities inverting the relations in (2.6) and (2.5), respectively. Nonlinear terms in  $R^{n+1}$  (e.g., metric terms arising in a geo-spherical physical system) may require outer iteration of the system of equations generated by (2.22) — see the Appendix of Smolarkiewicz et al. (2001) for a discussion. When included, diabatic viscous or subgrid-scale forcings may be explicitly added to first-order accuracy assuming  $SGS(\psi^{n+1}) = SGS(\psi^n) + \mathcal{O}(\Delta t)$ ; see section 3.5.4 in Smolarkiewicz and Margolin (1998).

# Chapter 3

## Examples of applications

Here the theory outlined in the preceding chapter is supplemented with three examples, validating both the conceptual and numerical aspects of the approach while illustrating the utility of the generalised vertical coordinate. In the first example, the use of time-dependent lower and upper boundaries with finite curvature is illustrated in three spatial dimensions, in the context of a homogeneous Boussinesq fluid enclosed by oscillating membranes. This demonstrates the capability to incorporate large amplitude boundary variations, testing the accuracy of the boundary conditions, which directly impact the convergence of the elliptic pressure solver. Furthermore, the approach complements biomedical numerical studies such as vascular flows, where an accurate description of a three-dimensional fluid flow bounded by undulating arterial walls is required, given accurate lateral boundary conditions already considered in [Nicoud and Schönfeld \(2002\)](#). The second example stresses the accuracy of the approach in the context of stably stratified atmospheric flows, supporting vertically propagating gravity waves, and shows the potential for alternative formulations of nonreflective upper boundaries. Finally, the third example illustrates the utility of the generalised Gal-Chen & Somerville coordinate transformation for numerical adaptivity to boundary forcings determined by data. In particular, an alternative for incorporating a finite-amplitude free-surface upper boundary is discussed in the context of a nonhydrostatic oceanic flow. A more complex application of nonlinear internal gravity wave processes in stably stratified flow, forced by a time-dependent boundary condition, will be presented in [chapter 4](#).

### 3.1 Boundary forced oscillating flow

Initially stagnant, adiabatic 3D flow of a homogeneous Boussinesq fluid is forced by oscillating impermeable free-slip upper and lower boundaries (“membranes”), with their shape prescribed as

$$\begin{aligned} z_s(r(x, y), t) &= \begin{cases} z_{s0} \cos^2(\pi r/2L) \sin(2\pi t/T) & \text{if } r/L \leq 1, \\ 0 & \text{otherwise,} \end{cases} \\ H(x, y, t) &= H_0 - z_s(x, y, t), \end{aligned} \quad (3.1)$$

with  $r = \sqrt{x^2 + y^2}$ , oscillation period  $T = 48\Delta t$ , amplitude  $z_{s0} = 48\Delta z$ , and the membranes' half-width  $L = 48\Delta x$ , where  $\Delta x = \Delta y = \Delta z$ . The computational domain consists of  $150 \times 150 \times 120$  grid intervals, in the horizontal and vertical, respectively. The advection scheme is semi-Lagrangian (Smolarkiewicz and Pudykiewicz, 1992). Note that after  $t = T/4$ , the upper and lower boundaries are separated merely by one fifth of the vertical extent of the model. In relation to geophysical scenarios, the present example is representative of steep (yet well resolved) orographies. The magnitude of the induced flow and its variation is approximately 5 and 0.5, respectively, as measured by  $\mathcal{C} \equiv \|\Delta t \bar{\mathbf{v}}^* / \Delta \bar{\mathbf{x}}\|$  and  $\mathcal{L} \equiv \|\Delta t \partial \bar{\mathbf{v}}^* / \partial \bar{\mathbf{x}}\|$  — the (maximal) Courant and “Lipschitz” numbers (cf. Smolarkiewicz and Pudykiewicz (1992) for a discussion).

Figure 3.1 illustrates the results. The flow vectors with imposed contour lines of the normalised perturbation pressure  $\pi'$  are shown at two phases of the simulation ( $t/T = 5/48$ , and  $t/T = 22/48$ ) which convey particularly well the reversing inward/outward flow patterns between the upward/downward oscillating membranes. Flow vectors are multiplied by  $\Delta t / \Delta x$  to acquire the sense of local Courant numbers; whereas  $\pi'$  is multiplied by  $2(\Delta t / \Delta x)^2$  relating to the squared lengths of the displayed vectors (via Bernoulli equation). Lacking diabatic forces, boundary friction, and buoyancy, the experimental setup implies a potential flow solution past oscillating membranes. The accuracy of the numerical solution can be assessed by examining the net pressure drag — i.e., the horizontal component of the integral pressure force on the bounding walls — that should vanish in consequence of the flow irrotationality (D'Alembert paradox, cf. section I.92 in Milne-Thomson (1968))<sup>1</sup>. Indeed, the model predicted net drag is of the order of round-off errors. The root mean square error of residual vorticity ( $\times \Delta t$ ), attributed primarily to the truncation errors of evaluating vorticity itself, is a few tenths of a percent of the flow variation measure  $\mathcal{L}$ . Finally, consider the Lagrangian form of the mass continuity equation  $\rho^* = \rho_o^* J^{-1}$  — readily available in semi-Lagrangian models (Smolarkiewicz et al., 2001) — where  $\rho_o^*$  refers to  $\rho^*$  at the departure point  $\bar{\mathbf{x}}_o$  of the trajectory arriving at a grid point  $\bar{\mathbf{x}}$ , and where  $J^{-1}$  denotes the inverse flow Jacobian,  $J^{-1} \equiv |\partial \bar{\mathbf{x}}_o / \partial \bar{\mathbf{x}}|$ . Subsequently, the density-normalised inverse flow Jacobian  $\mathcal{J} := (\rho_o^* / \rho^* J^{-1}) \equiv 1$  can be employed to assess the accuracy of the computations<sup>2</sup>. The model predicted, domain-averaged values of  $\mathcal{J}$  are between 0.99 and 1.01, with standard deviations 0.02 – 0.03. Summarising, we have found this experiment a convenient tool to validate the correctness of implementation of the solenoidal velocity boundary conditions (implying Neumann boundary conditions for pressure), ensuring the integrability condition of the elliptic pressure equation.

## 3.2 Orographically-forced atmospheric gravity waves

To illustrate the accuracy and practicality of the generalised coordinate transformation for atmospheric applications, a fully anelastic flow past a given terrain profile is considered

<sup>1</sup>For a discussion of *form drag* in the geophysical context of stratified flows see sections 6.8 and 8.7 in Gill (1982); for a derivation from the momentum budget cf. Clark and Miller (1991); Welch et al. (2001).

<sup>2</sup>In general, for a flow to be realizable (topological),  $0 < \mathcal{J} < \infty$ .



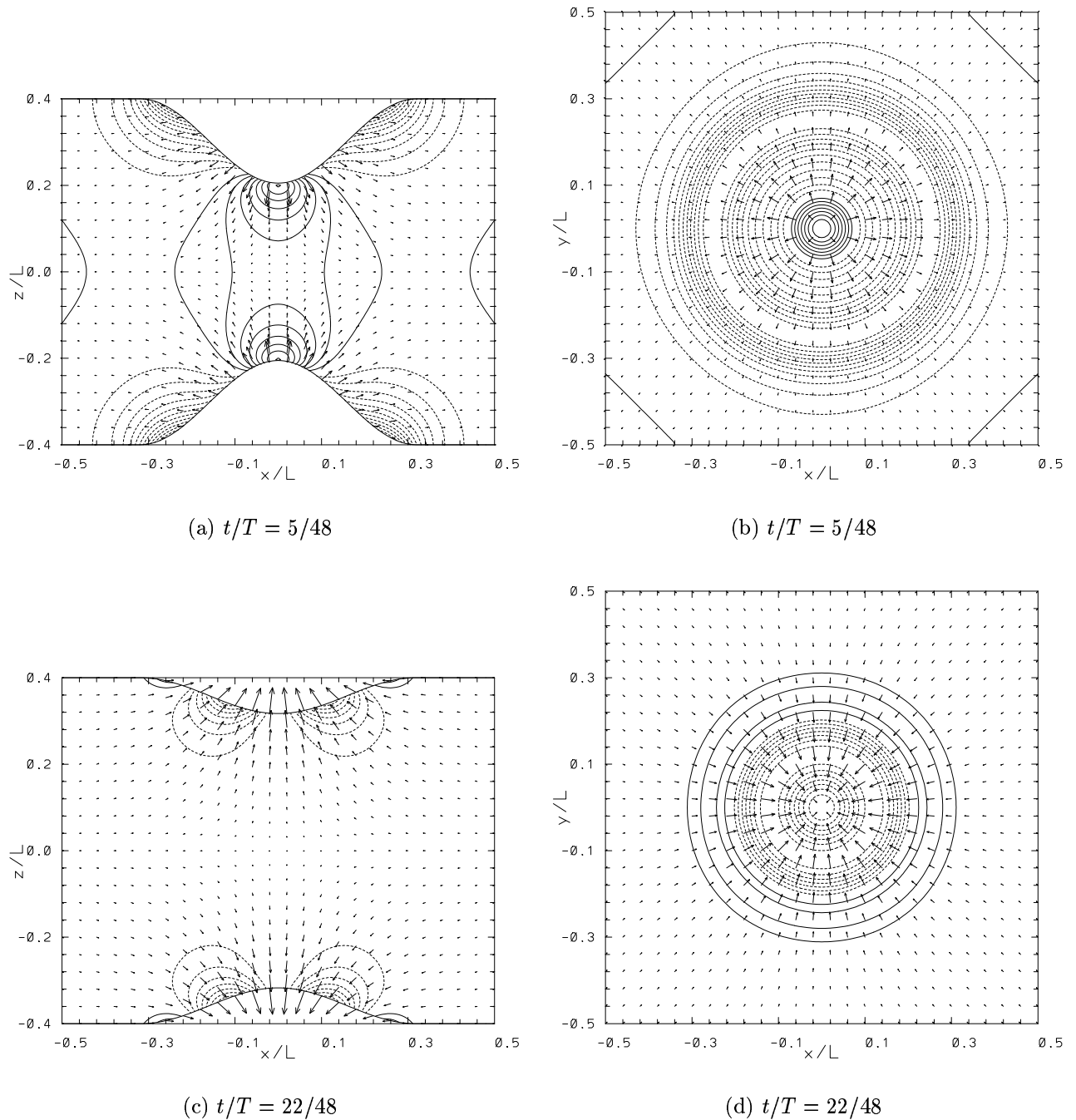


Figure 3.1: Oscillating membranes bounding a homogeneous Boussinesq fluid. The figure shows the vectors of local Courant numbers and contour lines of the normalised pressure (see the text for the normalisation details) in two distinct phases of the induced flow, outflow (plates a and b) and inflow (plates c and d). Plates (a) and (c) show vertical  $xz$  cross sections at  $y = 0$ ; whereas plates (b) and (d) display the solution at  $z = z_s$ , defined in (3.1). The contour intervals are 2 (zero contour lines are not shown), and the arrow length equal to the distance of two minor axis tickmarks is 4.

under stably stratified atmospheric conditions — a canonical problem in meteorological studies. A suite of classical problems with flows past a bell-shaped mountain has been simulated and compared against identical but “upside-down” experiments with a bell-shaped valley at the upper boundary, gravity and stratification reversed. Such experiments validated the correctness of the generalised vertical coordinate, both theoretically and with respect to the numerical implementation.

In the following the special benchmark problem proposed recently by Schär et al. (2002) is discussed, stressing numerical implementations of the classical Gal-Chen & Somerville transformation in the limit of marginally resolved orographic features. The selected parameters of the problem favour bifurcation into a qualitatively incorrect solution (Klemp et al., 2003). To emphasise the robustness of the generalised transformation, the Schär et al. calculations are repeated while storing the instantaneous heights of a selected isentropic (material) surface, so as to create a time-dependent upper boundary for the subsequent simulation with a domain of approximately half the vertical extent. The terrain profile is given as

$$z_s(x) = z_{s0} \exp\left(\frac{-x^2}{a^2}\right) \cos^2\left(\frac{\pi x}{\lambda}\right), \quad (3.2)$$

with  $z_{s0} = 0.25 \text{ km}$ ,  $a = 5 \text{ km}$  and  $\lambda = 4 \text{ km}$ . Ambient conditions consist of the uniform wind profile  $u_e(z) = U = 10 \text{ ms}^{-1}$ , ( $v_e = 0, w_e = 0$ ) and a Brunt-Väisälä frequency  $N = 0.01 \text{ s}^{-1}$ . The domain is  $70 \times 21 \text{ km}$ , with a horizontal and vertical grid spacing of  $500 \text{ m}$  and  $300 \text{ m}$ , respectively. The integration time is  $5 \text{ h}$  with a time step  $\Delta t = 10 \text{ s}$ . The upper  $11 \text{ km}$  of the model domain are designated to an absorbing layer, to simulate an infinite atmosphere and to suppress spurious wave reflection from the upper rigid-lid. Lateral absorbers extend for  $10 \text{ km}$  away from the boundaries.

Figure 3.2(a) shows the vertical velocity in the reference solution. This is the correct solution in agreement with the linear analytic result. For bifurcated, incorrect solutions see Klemp et al. (2003). The result in Figure 3.2(a) has been obtained using the Eulerian option of the model with the MPDATA advection scheme. However, the same results have been reproduced using the semi-Lagrangian option. The line at  $z \approx 9.6 \text{ km}$  in the figure marks the height of an isentrope that has been extracted (by means of interpolation) and stored at each time step of the reference run. Here we exploit the material property (viz. impermeability) of isentropic surfaces in adiabatic flows, to create a time-dependent upper boundary condition for the finite domain simulation, without absorbing layer. This height data has been used in the coordinate transformation at each time step, to prescribe numerically  $H(x, y, t)$  and  $\partial H(x, y, t)/\partial t$ . In (2.19), these determine uniquely the solenoidal velocity consistent with zero normal flow through the boundary.

Figure 3.2(b) shows the vertical velocity in the reduced-domain simulation. This solution reproduces the reference result in Figure 3.2(a) in the overlapping domain, despite spatial interpolation and finite time-differencing used to determine  $H(x, y, t)$  and  $\partial H(x, y, t)/\partial t$  from the reference run, and despite the sensitivity of the problem to numerical details (Klemp et al., 2003). Furthermore, the entire time evolution of both solutions has been found to be the same.

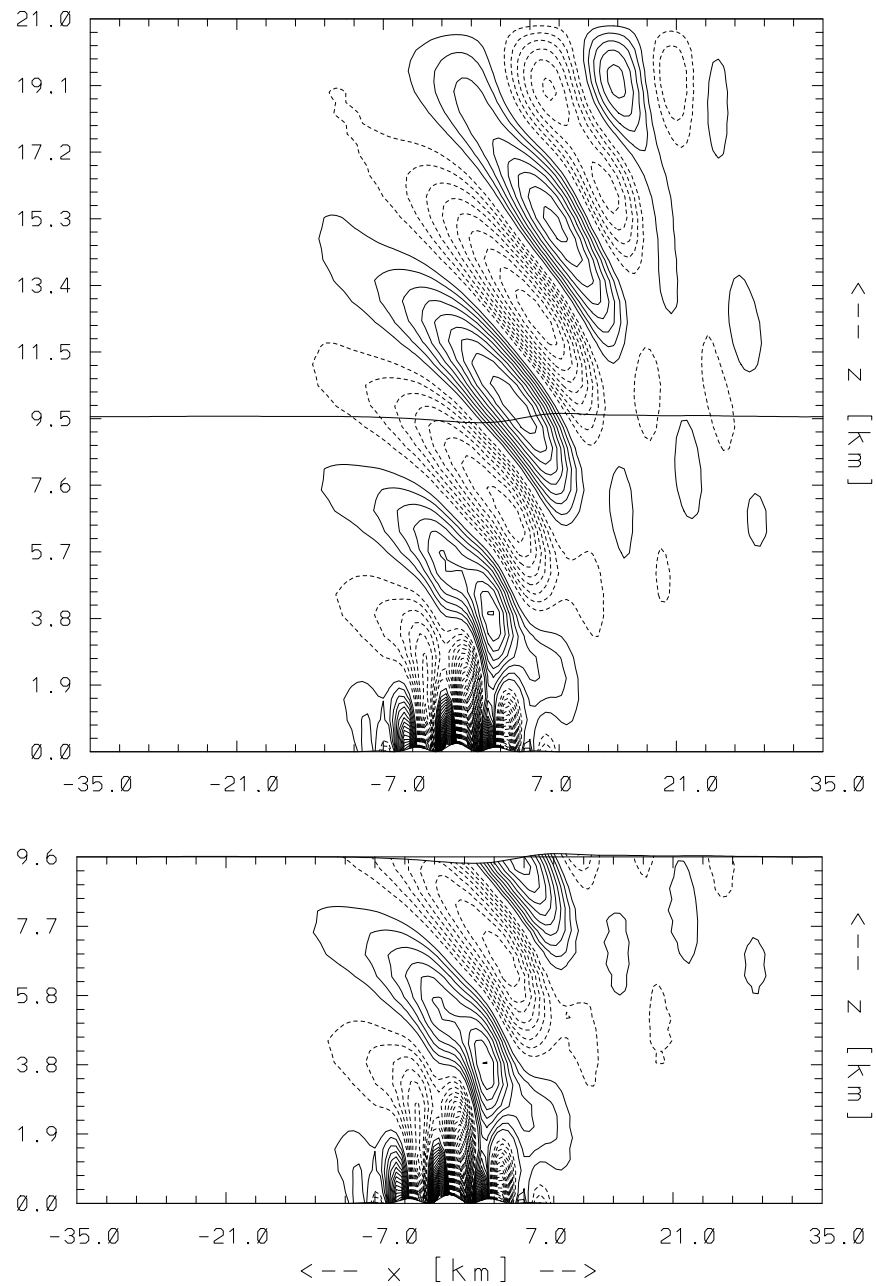


Figure 3.2: Vertical velocity for the flow past the terrain profile given in (3.2) after 5 hours of simulation when the fields have essentially reached a steady state. The upper plate represents the reference solution with a sponge layer. The indicated isentropic surface (at an undisturbed height  $9.6 \text{ km}$ ) has been extracted from this run at each time-step and served as the material upper boundary for the reduced-domain simulation shown in the lower plate. The contour interval in both plates is the same as in Klemp et al. (2003),  $0.05 \text{ m s}^{-1}$  (zero contour lines not shown).

The reduced-domain simulation did not require any absorbing layer or other form of radiative boundary condition, using 36% less CPU time than the reference run. Although designed as a reflexivity test, this experiment appears to indicate the potential for alternative formulations of nonreflective upper boundaries via a generalised (non-stationary) vertical coordinate. This contrasts Grosch and Orszag’s (1977) conclusions on the uselessness of (stationary) mappings for numerically solving problems in infinite regions. In general, the proposed framework eases the incorporation of any external boundary condition, e.g. by estimating the shape of the upper boundary using auxiliary models, like isentropic models for atmospheric applications, or, as demonstrated in the next example, a shallow-water model for oceanic applications.

### 3.3 Finite amplitude free surface flow

The numerical framework described in this thesis enables in principle the specification of the upper surface by arbitrary means (either approximated or exactly prescribed). However, the aim is to use approximations that preserve the computational cost-effectiveness compared to other approaches, while relevant to geo-physical applications. In this example, the practicality of incorporating an approximate free-surface boundary in nonhydrostatic ocean models is documented. The time-dependent coordinate transformation is driven by the solution of the shallow-water equations, a lowest-order long-wave approximation to free-surface flows; cf. Nadiga et al. (1996) for a discussion. A series of simulations in different flow regimes have been performed, to assess the physical applicability of this auxiliary boundary model. Following the methodology in Rotunno and Smolarkiewicz (1995); Nadiga et al. (1996), the results are compared against “two-layer” simulations with a density ratio 1/1000, defined continuously over a thin interfacial layer within the same fluid.

To accommodate the physics of the problem the incompressible Euler equations are solved as

$$\begin{aligned} \frac{\partial(\overline{Gv^{sk}})}{\partial \bar{x}^k} &= 0, \\ \frac{dv^j}{d\bar{t}} &= -\frac{1}{\rho} \tilde{G}_j^k \frac{\partial \phi'}{\partial \bar{x}^k} - g \left(1 - \frac{\rho_e}{\rho}\right) \delta_3^j, \\ \frac{d\rho}{d\bar{t}} &= 0, \end{aligned} \tag{3.3}$$

where  $\phi'$  denotes the pressure perturbation from a hydrostatically balanced environment characterised by a density profile  $\rho_e = \rho_e(z)$ . In the “two-layer” simulations the profile with a density “discontinuity” at the representative (undisturbed) fluid depth  $d_0$  is prescribed as

$$\rho_e(z) = \rho_r \left[1 - 0.5\Delta\rho \left(1 + \tanh \frac{z - d_0}{\gamma}\right)\right], \tag{3.4}$$

where  $\rho_r = 1$ ,  $\Delta\rho = 0.999$ , and  $\gamma = \Delta z$ . The reduced domain simulations assume  $\rho_e = \rho_r$ , with a time-dependent upper boundary approximated by the nonlinear hydrostatic shallow-

water equations

$$\begin{aligned}\frac{\partial d_1}{\partial t} + \frac{\partial(v^j d_1)}{\partial x^j} &= 0, \\ \frac{dv^j}{dt} &= -g^* \frac{\partial H}{\partial x^j},\end{aligned}\tag{3.5}$$

where  $d/dt = \partial/\partial t + v^j \partial/\partial x^j$  with  $j = 1, 2$ , the reduced gravity  $g^* = g\Delta\rho/\rho_r$  (Rottunno and Smolarkiewicz, 1995) and the density-weighted, normalised fluid depth  $d_1 \equiv \rho\overline{G}_0 = \rho(H - z_s)/H_0$ .<sup>3</sup> The reduced-domain experiments are complemented with a series of runs using a flat rigid-lid upper boundary, to illustrate the influence of different boundary conditions common in oceanic applications.

All the “two-layer” and reduced-domain experiments simulate the flow past a 2D ridge of the form

$$z_s(x) = z_{s0}(1 + (x/a)^2)^{-1.5}.\tag{3.6}$$

The different flow simulations are uniquely characterised by particular choices of the environmental Froude number  $F_u = U/\sqrt{gd_0}$ , the normalised ridge height  $z_{s0}/d_0$  and the normalised half-width  $a/d_0$ . For a given half-width  $a$ , the flow regime of a shallow fluid over an obstacle is uniquely determined by  $F_u$  and  $z_{s0}/d_0$  (Houghton and Kasahara, 1968). Consequently, ensembles of runs have been performed, categorising each run with respect to  $F_u$  and  $z_{s0}/d_0$ . The scenarios summarised in Table 3.1 are representative of these experiments for the three distinct flow regimes and are marked in the regime diagram, Figure 3.3, as in Houghton and Kasahara (1968); Nadiga et al. (1996)<sup>4</sup>. The numerical setup follows Nadiga et al. (1996). All lengths in the computations are in units of the representative fluid depth  $d_0$  and time is expressed in terms of  $\sqrt{d_0/g}$ . All simulations assume free-slip at the lower boundary. At the lateral boundaries, the solution is attenuated towards the ambient conditions with an inverse time-scale that increases linearly from 0 at the distance  $26\Delta x \approx 2d_0$  to  $(16\Delta t)^{-1} \approx (3a/U)^{-1}$  at the boundary. In the “two-layer” simulations the model domain  $(x, z) \in [-20d_0, 20d_0] \times [0, 3d_0]$  is resolved with  $NX \times NZ = 512 \times 96$  uniform grid increments  $\Delta x = 5/64$  and  $\Delta z = 2/64$ . In the (vertically) reduced domain simulations the time-dependent upper boundary is placed at the height of the undisturbed interface layer, equivalent to the representative fluid depth  $d_0$ . The semi-Lagrangian option of the model algorithm has been used for these simulations, cf. Nadiga et al. (1996); whereas the shallow-water equations (3.5) have been integrated with the Eulerian NFT scheme (Smolarkiewicz and Margolin, 1993). The time-step in both the “two-layer” simulation and the reduced-domain simulation was  $\Delta t = 2/64$ . The explicit shallow water model was integrated with  $1/10\Delta t$  due to the fast surface gravity wave mode.

Figure 3.4 compares the flat rigid-lid and the shallow-water approximated upper boundary simulations with the “two-layer” runs, for the different flow regimes summarised in

<sup>3</sup>Here,  $d_1 \sim (H - z_s)$ ; for a discussion linking the incompressible Euler equations (3.3) and the shallow water equations in (3.5) see Gill (1982), chap.5.6 pp.107.

<sup>4</sup>The solid line in the regime diagram represents equation (3.5) in Houghton and Kasahara (1968), the dashed line dividing region II is found using a multivariate Newton-Raphson method to solve the set of non-linear algebraic equations (3.8)-(3.17) in Houghton and Kasahara (1968) for  $c_r = 0$ .

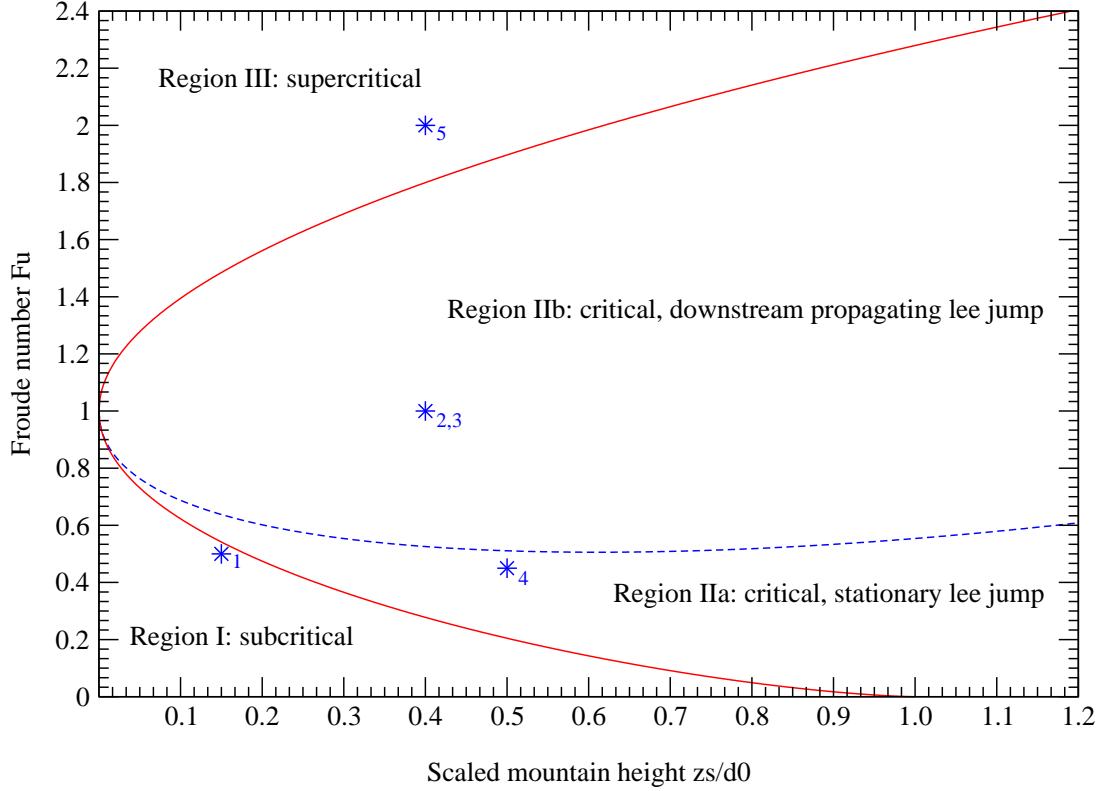


Figure 3.3: The regime diagram for the hydrostatic shallow-water equations (Houghton and Kasahara, 1968). The x-axis is the dimensionless ridge height and the y-axis is the undisturbed Froude number  $F_u = U/\sqrt{gd_0}$ . Region I is entirely subcritical, and the free surface dips symmetrically about the obstacle. Region III is entirely supercritical, and the free surface rises symmetrically about the obstacle after some time. In region IIa, there is an upstream-propagating hydraulic jump and a stationary lee-side hydraulic jump. In region IIb, there is an upstream-propagating and a downstream-propagating hydraulic jump. Parameters corresponding to the 5 cases discussed in this paper are marked with an asterisk (\*).

Table 3.1. Despite the exaggerated bathymetric forcing in the examples — as opposed to bottom profiles typically used in ocean models — the comparison in subcritical, critical, and supercritical conditions shows good agreement between the long-wave approximation to a free-surface and the “two-layer” simulation. In contrast, the flat upper boundary results in a diverse solution throughout the interior domain, impacting the flow not only above the mountain but also upstream and downstream of the obstacle.

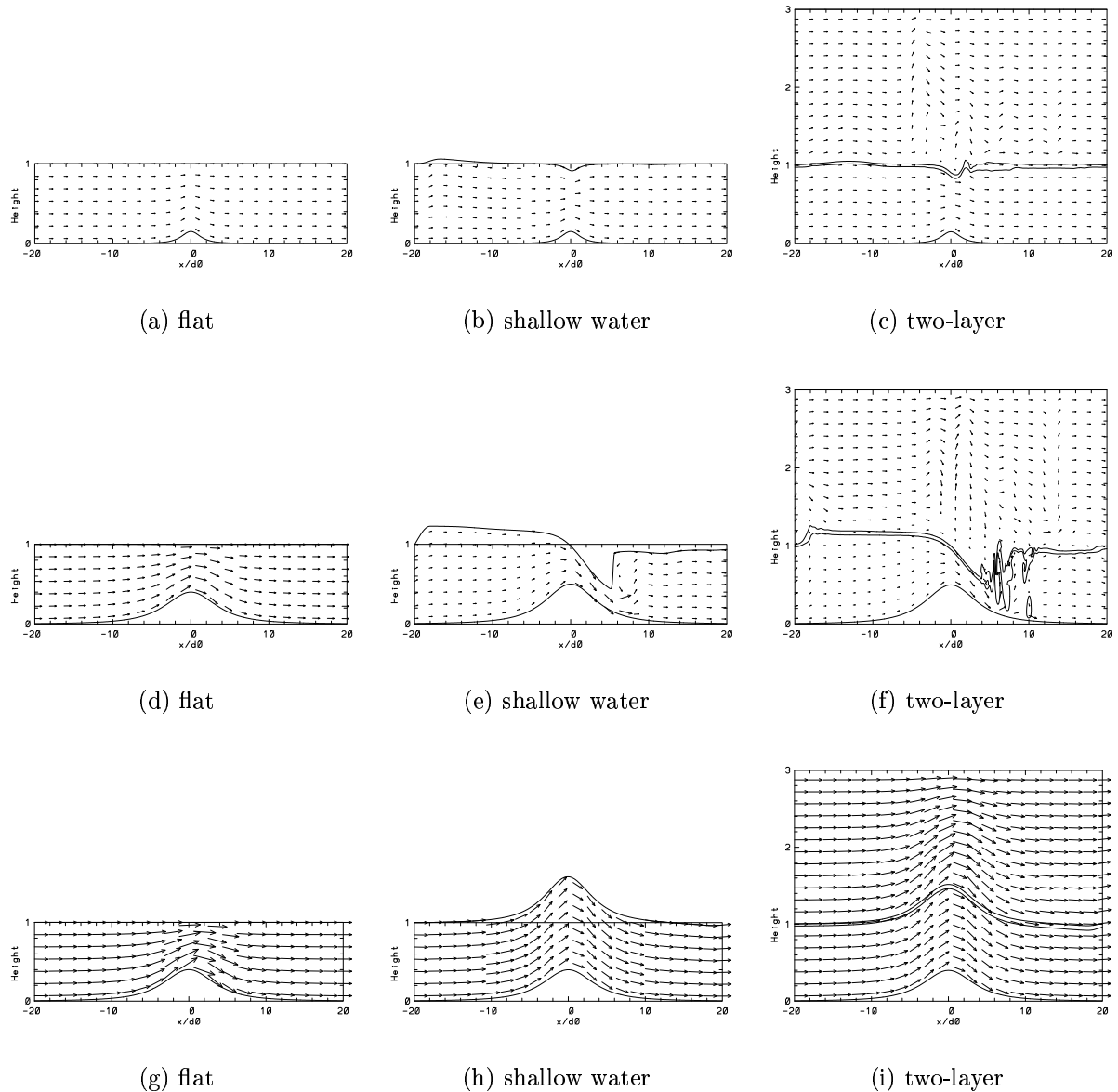


Figure 3.4: Summary of the solutions with a gentle slope for subcritical (a)-(c), critical (d)-(f) and supercritical (g)-(i) flow conditions at time  $t = 0.5$  (indices 1,4 and 5 in Table 3.1, respectively). Results are shown for the simulations with a flat rigid-lid (flat), a predicted shallow-water upper surface (shallow-water) and a “two-layer” simulation (two-layer). The arrow length equal to the distance of two minor x-axis tickmarks is 2. The two contour lines in the two-layer plot are at 0.105 and 0.905 times the density of the lower layer, indicating the position of the density discontinuity between the two layers.

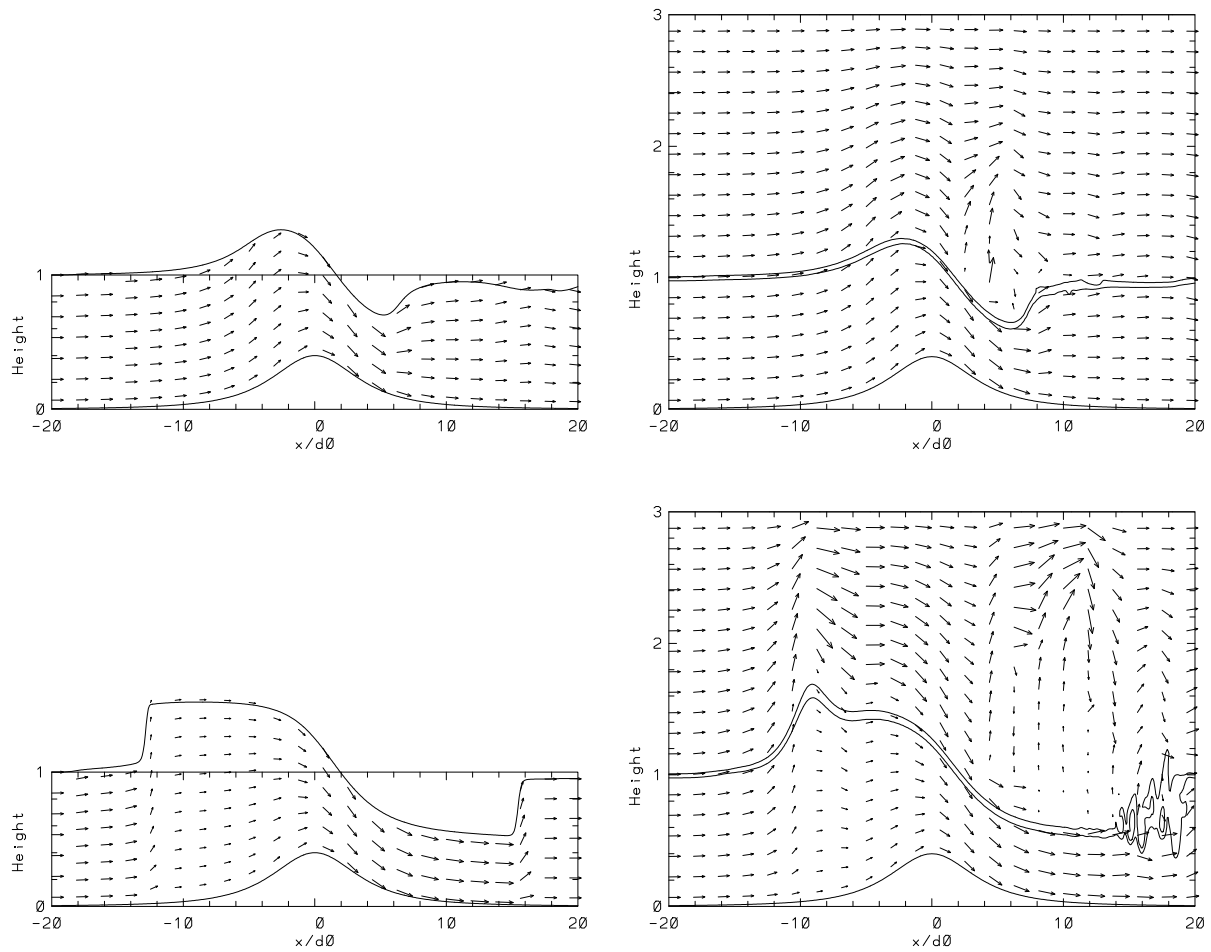


Figure 3.5: Time evolution of a critical flow (case 3 in Table 3.1) at time  $t = 0.15$  and  $t = 0.5$ , respectively, for a predicted shallow-water upper surface (left plates) and a “two-layer” simulation (right plates). Contours and arrow lengths are as in figure 3.4.

Table 3.1: Summary of representative experiments for free surface flows in distinct flow regimes, characterised by the dimensionless Froude number  $F_u$ , normalised ridge height  $z_{s0}/d_0$  and normalised half-width  $a/d_0$ .

<i>index</i>	<i>regime</i>	$F_u$	$z_{s0}/d_0$	$a/d_0$	<i>mountain</i>
1	subcritical	0.5	0.15	1.875	gentle
2	critical	1.0	0.4	1	steep
3	critical	1.0	0.4	5	gentle
4	critical	0.45	0.5	5	gentle
5	supercritical	2.0	0.4	5	gentle



Both the sub- and supercritical solutions reach a steady state, whereas under critical conditions the flow is inherently transient (Houghton and Kasahara, 1968). Figure 3.5 summaries the time evolution of a critical flow. It can be seen in the figure as the time progresses that both the upwind propagating bore and the hydraulic lee jump steepen. The detailed comparison deteriorates, but the qualitative behaviour of the fluid in the interior of the domain remains in agreement with the “two-layer” simulation. The deterioration is not surprising due to the breakdown of the hydrostatic assumption, underlying the shallow-water equations in (3.5); cf. Nadiga et al. (1996) for a discussion. To illustrate this effect further, Figure 3.6 shows a complete breakdown of the postulated auxiliary boundary model for the (no longer) continuously bounding surface in the special case of a critical flow past a steep mountain (about 50 degrees maximum slope). The observed breakdown does not imply a conceptual shortcoming of the method, but rather indicates the need for more accurate auxiliary boundary models. For example, the generalised-Boussinesq or Green-Naghdi nonhydrostatic equations may be considered for higher-order asymptotic approximations, cf. Nadiga et al. (1996). In some applications it may suffice to regularise boundary discontinuities by artificial dissipation, cf. section 12.10 in Richtmyer and Morton (1967).

The explicit auxiliary boundary model based on the simple shallow water equations captures the physical nature of finite-amplitude free-surface flows, given a gentle bathymetry (slopes of up to 13 degrees have been successfully tested<sup>5</sup>). This shows the potential for alternative means of incorporating free-surface boundaries in meso- and large-scale oceanic models, where infinitesimal-amplitude surface elevations are typically assumed for simplicity (Iskandarani et al., 2003). Given suitable higher-order asymptotic approximations, the approach in this thesis may complement inherently implicit methods (in all model variables)<sup>6</sup>, typically used in engineering applications involving free-surface flows (Casulli and Cheng, 1992; Casulli, 1999).

The preceding examples have illustrated the correct numerical implementation and the utility of the generalised vertical coordinate in the context of canonical problems of atmospheric and oceanic flows. The next chapter illustrates its use and resulting new insights into the physics of the problem in a real application of great importance for tropical predictability: the direct numerical simulation of the quasi-biennial oscillation analogue.

---

<sup>5</sup>In comparison, resolved topographic slopes typically found in operational, high resolution global numerical weather prediction models are about 3-4 degrees (e.g., ECMWF)

<sup>6</sup>Vertical integrals over the nonhydrostatic interior domain are employed to obtain an additional equation for  $H(x, y, t)$  while assuming the validity of a hydrostatic representation of pressure in the top layer. Despite the complexity of the resulting implicit formulation, it enables the prediction of the impact of the internal flow on phase and amplitude of surface waves, and vice versa, simultaneously (Namin et al., 2001).

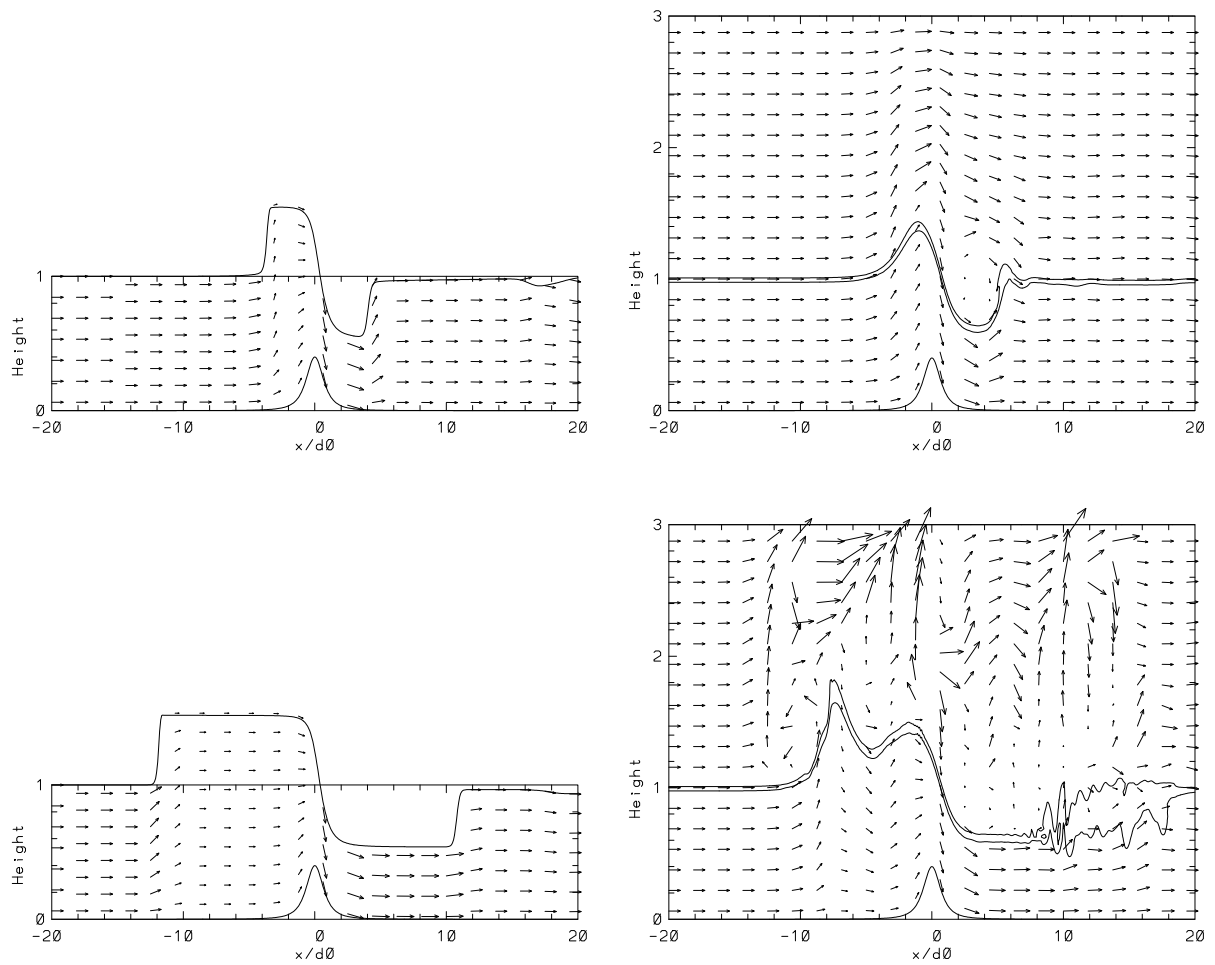


Figure 3.6: Solutions for a critical flow past a steep mountain (case 2 in Table 3.1) at time  $t = 0.15$  and  $t = 0.5$ , respectively, for a predicted shallow-water upper surface (left plates) and a “two-layer” simulation (right plates). Contours and arrow lengths are as in figure 3.4.

# Chapter 4

## The numerical equivalent to the quasi-biennial oscillation analogue

The previous chapter demonstrated the ability of the numerical framework to simulate unstratified or weakly-stratified fluids while adapting to complicated time-dependent boundaries. In this chapter the newly developed framework is applied to a particular challenging case in the class of problems with time-dependent (boundary) forcings: the laboratory analogue of the quasi-biennial oscillation. As will be shown, this case exhibits a number of internal gravity wave processes, wave interference, wave-mean flow interaction, critical layer formation and subsequent wave breaking. All of these processes are found in the atmosphere but their distinction is difficult to deduce from observations alone. In contrast to atmospheric modelling studies, the forcing wave spectrum is explicitly known in this case and in contrast to laboratory experiments far more information is available from the numerical simulation for process identification. It is therefore that the numerical framework presented here becomes a useful tool as a confined numerical “laboratory” environment to study internal wave processes.

First, a detailed description of the laboratory experiment and of its numerical setup is presented in section 4.1. The 3D and 2D numerical simulations which have been performed are summarised in section 4.2 and table 4.1 and table 4.2, respectively. Then a number of parametric sensitivities, i.e. to viscosity, diffusivity, stratification, and amplitude and frequency of the external (boundary) forcing are investigated in section 4.2.1. Subsequently in section 4.2.2, numerical influences and (artificial) boundary effects are further explored in view of the direct comparability to the laboratory equivalents. In section 4.3 a comprehensive energy analysis is used to verify a closed energy budget, accounting for all physical processes and to clarify the role of numerical dissipation. The spectral analysis presented in section 4.4 is used to identify the simulated internal wave spectra and their respective spatial and temporal distribution. Theoretical considerations in section 4.5 complement the data analysis leading to the detailed description in section 4.6 of the evolution and the internal wave processes exhibited in the QBO analogue simulation. This chapter concludes with a summary of the presented results in section 4.7. The implications of the findings for atmospheric equatorial zonal mean flow oscillations are then discussed in chapter 5.

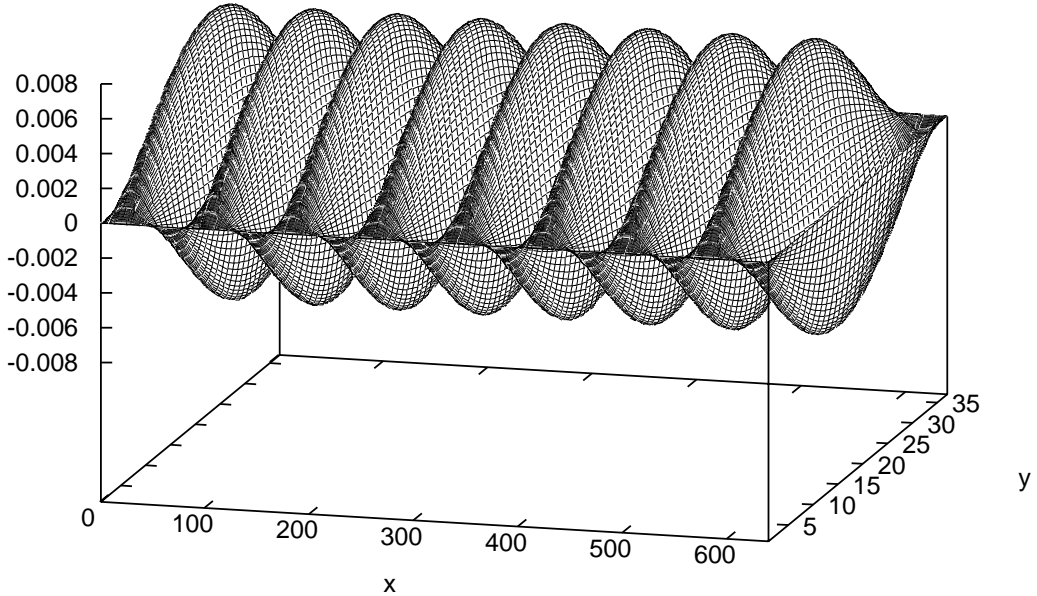


Figure 4.1: The shape of the oscillating membrane as described by equation (4.1).

## 4.1 Experimental setup

The laboratory experiment of Plumb and McEwan has been conducted in a transparent cylindrical annulus (radii  $a = 0.183 \text{ m}$  and  $b = 0.3 \text{ m}$ ) filled with density-stratified salty water to a height of  $z_{ab} = 0.43 \text{ m}$ . The lower boundary consisted of a thin rubber membrane whose amplitude oscillated with a constant frequency  $\omega_0 = 0.43 \text{ s}^{-1}$  (Plumb and McEwan, 1978). In the numerical simulation of their laboratory setup an initially stagnant, viscous Boussinesq fluid is assumed which is forced by an oscillating impermeable lower (upper) boundary. The cylindrical setup of the laboratory tank is replaced with a zonally-periodic, rectangular computational domain consisting of  $639 \times 38 \times 188$  grid intervals with  $L_x = 2\pi(a + b)/2$ ,  $L_y = b - a$ ,  $L_z = 0.6 \text{ m}$  and no-slip boundaries. The lower boundary shape (illustrated in figure 4.1)<sup>1</sup> is specified as

$$z_s(x, y, t) = \epsilon \sin\left(\frac{\pi}{L_y}y\right) \sin\left(\frac{2\pi s}{L_x}x\right) \sin(\omega_0 t) \quad (4.1)$$

with  $s = 8$  and forcing amplitude  $\epsilon = 0.008 \text{ m}$ . The initial condition is assumed identical to the static ambient state with a range of buoyancy frequencies  $N = 1.37\text{--}1.88 \text{ s}^{-1}$ . The integration time was several hours with a time-step  $dt = 0.05 \text{ s}$ . In some experiments the distance  $L_z - z_{ab}$  is designated to an absorbing layer, which suppresses spurious wave reflection from the upper rigid-lid, simulating a vertically infinite water tank. The influence of different upper boundary conditions is discussed in more detail in the next section. It

<sup>1</sup>The shape is a solution of the two-dimensional wave-equation in a rectangular domain with the appropriate boundary conditions (Bronstein and Semendjajew, 1987), pp.484.

is found, however, that in 3D simulations reflections from the upper boundary appear to be negligible in agreement with laboratory observations (Plumb and McEwan, 1978).

Starting from a zero background flow symmetrical, upward propagating, but horizontally standing gravity waves are observed. After approximately 1-2 hours (in agreement with laboratory observations (Plumb and McEwan, 1978), but see also the discussion in section 4.2.2)<sup>2</sup> the wave-field distorts and spatial wave interference is observed. Subsequently, the coherent wave structures break down and a “critical layer” forms, giving rise to an apparent downward propagation of a mean flow pattern which reverses sign in a periodic manner. This process can be seen in figure 4.3. Figure 4.2 shows time-height cross-sections of the zonal-mean flow for two representative simulations. Table 4.1 summarises the quantitative comparison between the 3D numerical simulations and the laboratory analogue of Plumb and McEwan. The table also shows results of the experiment performed by the university of Kyoto ([www.gfd-dennou.org](http://www.gfd-dennou.org), 2004) where the oscillating membrane was placed at the top of an annulus (figure 1.2) initiating an oscillation with an apparent upward propagation of the mean flow. In this case the correct physical lower boundary is a rigid lid and the upper boundary entering the transformation in (2.7) is given as

$$H(x, y, t) = H_0 - z_s(x, y, t). \quad (4.2)$$

The following chapter discusses in detail various aspects of the simulated mean flow oscillations.

## 4.2 Summary of the numerical simulations

It is found that all numerical and parametric influences on the dispersion and dissipation of internal gravity waves change the observed mean flow oscillation, rendering a near infinite list of effective possibilities for the variability and realisability in numerical simulations. In part this may explain the difficulty in accurately modelling a QBO in three dimensions.

Both, parametric and numerical sensitivities with respect to the period influence in particular two aspects of the oscillation: the height at which sufficient zonal mean-flow is generated, to initiate an enhanced convergence of wave-induced stress and mean flow reversal; and the speed of the apparent downward propagation by continued wave momentum flux convergence below the initial level. The sensitivities can further be grouped into two categories, sensitivities with respect to the onset of the mean flow oscillation and sensitivities with respect to its period. It is possible to separate the latter two problems since one could prescribe an initial constant environmental zonal wind in the lowest 1 – 6 cm (depending on the problem with free-slip or no-slip boundary conditions) which is equivalent to starting with a first phase of the oscillation (see section 4.6 for an explanation). This

<sup>2</sup>If the initial fields are disturbed using random white noise it is possible to accelerate the onset of the oscillation. However, substantial CPU time can be saved (without affecting the results) by forcing an oscillation with a background flow in the near-membrane layers ( $d_0 = 0.06$  m) using  $u_e = u_0[1 - 0.5\delta(1 + \tanh(z - d_0)/\gamma)]$  with  $u_0 = 0.01$   $ms^{-1}$ ,  $\delta = 0.9999999$ , and  $\gamma = \Delta z$ . This mechanism has been used in almost all simulations summarised in table 4.1.

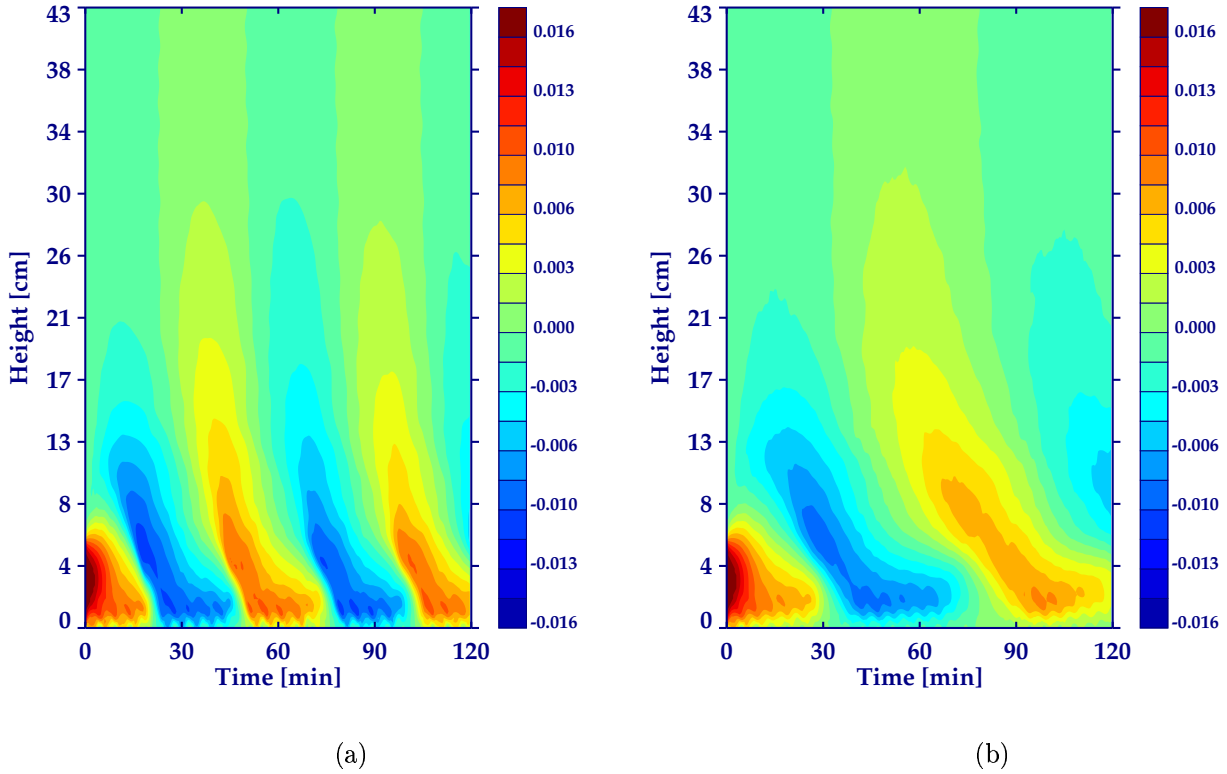


Figure 4.2: Time-height cross-section of the zonal-mean zonal flow velocity component at  $y = L_y/2$  in the 3D numerical simulation of the original Plumb and McEwan setup. Plate a [case (u) in Table 4.1] shows the results with a regular forcing membrane. Plate b [case (v) in Table 4.1] shows the numerical result with an “imperfect” membrane, when two arbitrarily chosen parts of the 16 oscillating membrane chambers oscillated only with half the amplitude. Plate b readily compares with the observation, left plate of Fig.10 in [Plumb and McEwan \(1978\)](#). Units are in  $m s^{-1}$ .

substantially reduced the required overall computing time. If the simulation is not started with an initial zonal wind it is not possible a priori to predict the onset of a positive or a negative mean flow. An initial oscillation then typically develops after 1-3 hours of simulation time. However, later a coding error has been found in the parallelisation creating an asymmetry in the zonal periodicity. In a subsequent 3D simulation with no initial random noise it failed to initiate an oscillation even after 4.5 hours of simulation. This suggests that in Nature an asymmetry in the wave field is responsible for the first initiation of the mean flow oscillation in the tank. The importance of this asymmetry is further discussed in section 4.2.2. It appears that the initial difficulty to create an oscillation in the laboratory of the university of Kyoto may be for the same reason ([www.gfd-dennou.org](http://www.gfd-dennou.org), 2004). Interestingly, it was solved through the addition of “dirty water” adding a disturbance to the stable stratification.

Some of the sensitivities mentioned here are investigated in the equivalent two dimen-

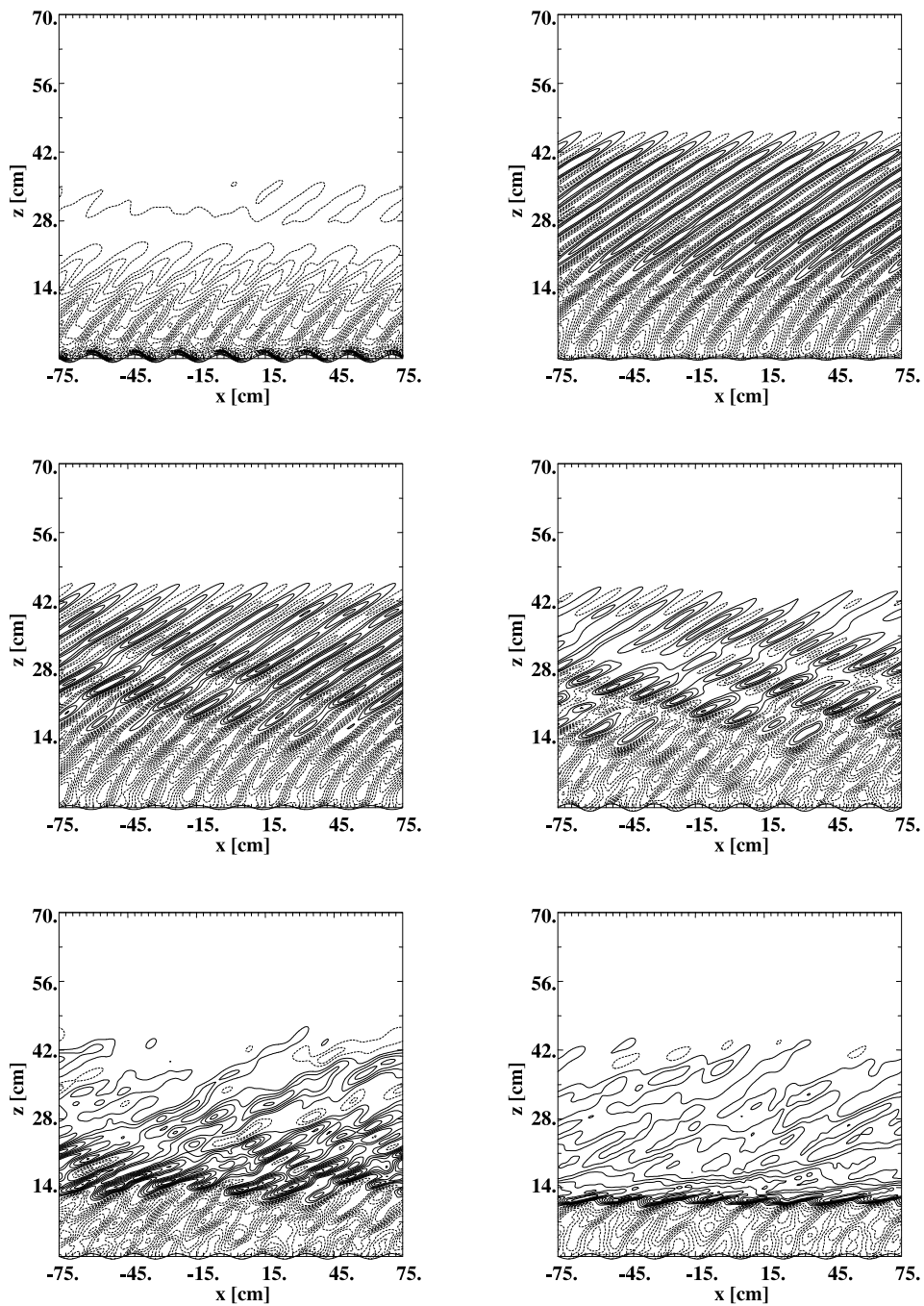


Figure 4.3: Numerical simulation of the Plumb-McEwan laboratory experiment. Different phases during the numerical 2D simulation of the quasi-biennial oscillation (QBO) analogue show propagating waves excited by the oscillating membrane at the bottom of the water tank, vertical wave interference and dispersion and the breakdown of coherent wave patterns by subsequent absorption of the upward propagating waves at the newly formed critical layer resulting in a 'descending' mean wind pattern.

sional problem. To enhance the comparability to the 3D simulations, energetically only the averaged effect of the three-dimensional oscillation is considered by reducing the effective forcing amplitude. 2D simulations agree with the three-dimensional simulation in the vertical structure only approximately, when compared with an infinite membrane of uniform shape in the meridional direction. As long as influences by the upper boundary play no role, the same behaviour in otherwise equivalent 2D and 3D simulations is found. However, since the upward energy propagation of two dimensional and three-dimensional internal gravity waves, due to the existence of a meridional flow, fundamentally differs (Smith, 1980), the vertical extent of the mean flow pattern in the two-dimensional case grows whereas in the three-dimensional case remains finite. Since the upward wave propagation speed is fairly fast, compared to the time it takes for the waves to interact, one would require a very deep water tank or perfect radiation boundary conditions, to exclude upper boundary effects. The different vertical extent and mean-flow oscillation period between the two-dimensional and the three-dimensional case is evident in Figure 4.4. The original upper boundary in the laboratory was an open water surface. Experiments in 2D show a significant difference depending on the type of upper boundary (free-slip rigid, no-slip rigid, free-slip shallow water) applied. This sensitivity results from reflected gravity waves that additionally interact with the original waves, effectively controlling the height of maximum zonal mean flow generation and controlling the period of the oscillation. However, the behaviour is far less obvious in three-dimensions. In the experiment setup of the university of Kyoto, the bottom of the tank represents a rigid-lid. The downward propagating gravity waves reflect from the bottom and additionally interact with the original waves, which appears to contribute to the relatively larger vertical extent of their observed mean flow oscillation.

The Tables 4.1 and 4.2 summarise all conducted three-dimensional and two-dimensional numerical experiments and compare them to the laboratory studies of Plumb and McEwan and the experiments at the university of Kyoto.

Notable in the results of Table 4.1 is the inability to reproduce the precise period of the original Plumb and McEwan experiment with the originally described setup in Plumb and McEwan (1978); yet by doubling the frequency or the physical domain (viz. the horizontal wave length) or by decreasing the stratification comparable periods are obtained. The stratification  $N = 1.88s^{-1}$  as obtained from the derived values of Fig.10 in Plumb and McEwan (1978),  $T_0 = 476$ ,  $d_0 = 0.17$ , and their formulas 4.10-4.12 appears inconsistent with their specifications in an original movie of their experiment and the explanations in the text. Therefore, a value of  $N = 1.57 s^{-1}$  as quoted in the original movie of the Plumb and McEwan experiment has been adopted for subsequent experiments. However, this is insufficient to resolve the difference, and the influence of the upper boundary used as well as other possible sensitivities are discussed in more detail at the end of section 4.2.2. It is noted here, that the largest sensitivity arises from the forcing wavelength. In the numerical simulation, assuming a small uncertainty ( $< 6$  percent) in its experimental realization, approximately reproduces the experimental result of a zonal mean flow oscillation with approximately 80 minutes period. The numerical results using an “imperfect” and a “perfect” membrane are compared in figure 4.2. In the right plate, two arbitrarily



<i>description</i> <sup>3</sup>	$n_x \times n_y \times n_z$	$L_x[m]$	$L_y[m]$	$L_z[m]$	$\epsilon[mm]$	$\omega_0[s^{-1}]$	$N[s^{-1}]$	$T_0[min]$	$z_0[m]$	$A_0[mm]$
a) lab: P+E	$\infty$	1.52	0.117	0.43	8.0	0.43	1.88	82	0.2	8.5
b) lab: P+E	$\infty$	1.52	0.117	0.43	8.0	0.44	1.57	85	–	–
c) lab: P+E	$\infty$	1.52	0.117	0.31	11.0	0.43	1.71	46	0.12	3.5
d) lab: Kyoto	$\infty$	3.14	0.2	0.6	11.0	0.40	1.60	80	–	–
e) lab: Kyoto	$\infty$	1.50	0.115	0.5	–	0.40	1.60	45 – 120	0.2	9
f) num: P+E, no slip	$384 \times 18 \times 189$	1.52	0.117	0.6(0.43)	8.0	0.37	1.88	25	0.11	6
g) num: P+E, no slip	$384 \times 18 \times 189$	1.52	0.117	0.6(0.43)	8.0	0.43	1.88	28	0.2	10
h) num: P+E, no slip	$384 \times 18 \times 189$	1.52	0.117	0.6(0.43)	8.0	0.61	1.88	50	0.3	15
i) num: P+E, free slip	$384 \times 18 \times 189$	1.52	0.117	0.6(0.43)	8.0	0.43	1.88	10	0.15	8
j) num: P+E, free slip vert	$640 \times 39 \times 189$	1.52	0.117	0.6(0.43)	8.0	0.43	1.88	15	0.15	12
k) num: P+E, no slip	$640 \times 39 \times 189$	1.52	0.117	0.6(0.43)	8.0	0.43	1.88	32	0.18	9
l) num: P+E, no slip	$640 \times 39 \times 189$	1.52	0.117	0.6(0.43)	8.0	0.43	1.57	52	0.2	9
m) num: P+E, no slip	$640 \times 39 \times 189$	1.52	0.117	0.6(0.43)	8.0	0.43	1.37	–	–	–
n) num: P+E, free slip vert	$640 \times 39 \times 189$	1.52	0.117	0.6(0.43)	8.0	0.55	1.88	24	0.2	17
o) num: P+E, free slip vert	$640 \times 39 \times 189$	3.14	0.2	0.6(0.43)	8.0	0.43	1.88	100	0.4	22
p) num: P+E, free slip vert	$384 \times 18 \times 189$	1.52	0.117	0.6(0.43)	8.0	0.86	1.88	106	0.4	25
q) num: Kyoto, no slip	$640 \times 39 \times 189$	3.14	0.2	0.6	11.0	0.40	1.60	> 100	0.4	24
r) num: Kyoto, free slip memb	$640 \times 39 \times 189$	3.14	0.2	0.6	11.0	0.40	1.60	76	0.3	23
s) num: P+E, free slip inviscid	$640 \times 39 \times 189$	1.52	0.117	0.6(0.43)	8.0	0.43	1.88	–	0.12	12
t) num: P+E, free slip rigid top	$640 \times 39 \times 189$	1.52	0.117	0.43	16.0	0.43	1.57	–	–	9
u) num: P+E, $\sim$ , perfect	$640 \times 39 \times 189$	1.52	0.117	0.43	8.0	0.43	1.57	50	0.2	9
v) num: P+E, $\sim$ , imperfect	$640 \times 39 \times 189$	1.52	0.117	0.43	8.0	0.43	1.57	85	0.2	8.5
w) num: P+E, $\sim$ , imperfect	$384 \times 39 \times 189$	1.52	0.117	0.43	11.0	0.43	1.57	48	0.1	9
x) num: P+E, $\sim$ , imperfect	$384 \times 39 \times 189$	1.52	0.117	0.43	11.0	0.31	1.57	26	0.1	4.5
y) num: P+E, $\sim$ , perfect	$384 \times 39 \times 189$	1.52	0.117	0.43	11.0	0.31	1.57	22	0.1	5.5

Table 4.1: Quantitative comparison of the mean-flow oscillations in the laboratory experiments [lab] (by Plumb and McEwan [P+E] and repeated by the university of Kyoto [Kyoto]) and in the 3D numerical simulations [num].  $T_0$ ,  $z_0$  and  $A_0$ , respectively, symbolise the period, the vertical depth and the amplitude of the oscillation for the given domain (alias wave number), forcing frequency  $\omega_0$ , forcing amplitude  $\epsilon$  and stratification  $N$ . – denotes no oscillation or unknown; *ir* denotes an irregular pattern or magnitude of the respective quantity; > indicates that the oscillation period was still growing (in particular typical for 2D simulations) but the simulation was not continued (the absolute value is not of interest in those cases since only sensitivities against an equally long reference run have been investigated).

<sup>3</sup>The value for  $T_0$  in the Kyoto setup is deduced from the movie found at [www.gfd-dennou.org](http://www.gfd-dennou.org) (2004). The value for  $N$  in the P+E setup is obtained from the derived values of Fig.10 ( $T_0 = 476$  s,  $d_0 = 0.17$  m) and Fig.11 ( $T_0 = 133$  s,  $d_0 = 0.082$  m) in Plumb and McEwan (1978), and their formulas 4.10-4.12. All other values are taken as stated in the cited references.

<i>description</i>	$n_x \times n_z$	$L_x[m]$	$L_z[m]$	$\epsilon[mm]$	$\omega_0[s^{-1}]$	$N[s^{-1}]$	$T_0[min]$	$z_0[m]$	$A_0[mm]$
a) lab: P+E	$\infty$	1.52	0.43	8.0	0.43	1.88	82	0.2	8.5
b) lab: P+E	$\infty$	1.52	0.43	8.0	0.44	1.57	85	–	–
c) lab: Kyoto	$\infty$	3.14	0.6	11.0	0.40	1.60	80	–	–
d) num: P+E	$640 \times 189$	1.57	0.6(0.43)	8.0	0.31	1.88	8 – 10	0.06	8
e) num: P+E	$640 \times 189$	1.57	0.6(0.43)	8.0	0.37	1.88	20 – 30	0.2	12
f) num: P+E	$640 \times 189$	1.57	0.6(0.43)	8.0	0.43	1.88	50	0.4	14
g) num: P+E	$640 \times 189$	1.57	0.6(0.43)	8.0	0.55	1.88	170	0.4	17
h) num: P+E	$640 \times 189$	1.57	0.6(0.43)	8.0	0.61	1.88	> 200	0.4	19
i) num: P+E	$384 \times 189$	1.52	0.6(0.43)	8.0	0.86	1.88	> 255	0.4	26
j) num: P+E	$640 \times 189$	1.57	0.6(0.43)	11.0	0.43	1.88	50 – 60	0.3	15
k) num: P+E mixed freq	$640 \times 189$	1.57	0.6(0.43)	8.0	0.31/0.37/0.43	1.88	25	0.2	11
l) num: P+E mixed $s = 4/8/16$	$640 \times 189$	1.57	0.6(0.43)	8.0	0.43	1.88	15 – 20	0.1	8
m) num: P+E mixed $s = 4/8/16$	$640 \times 189$	1.57	0.6(0.43)	8.0	0.43/0.37/0.31	1.88	<i>ir</i>	<i>ir</i>	21
n) num: Kyoto	$640 \times 189$	3.14	0.6	11.0	0.40	1.60	> 120	0.6	27
o) num: P+E free-slip rigid top	$384 \times 189$	1.52	0.43	8.0	0.43	1.57	<i>ir</i>	<i>ir</i>	11
p) num: P+E no-slip rigid top Eul.	$384 \times 189$	1.52	0.43	8.0	0.43	1.57	165	0.4	11
q) num: P+E no-slip rigid top Eul. $s = 8/12/3.2$	$384 \times 189$	1.52	0.43	8.0	0.43/0.645/0.172	1.57	130 – 140	0.4	12 – 13
r) num: P+E no-slip rigid top SL.	$384 \times 189$	1.52	0.43	8.0	0.43	1.57	<i>ir</i>	<i>ir</i>	10
s) num: P+E free-slip shallow	$384 \times 189$	1.52	0.43	8.0	0.43	1.57	<i>ir</i>	0.3	11
t) num: P+E no-slip shallow	$384 \times 189$	1.52	0.43	8.0	0.43	1.57	165	0.4	11
u) num: P+E inviscid	$640 \times 189$	1.52	0.43	8.0	0.43	1.88	–	<i>ir</i>	17
v) num: P+E near inviscid	$640 \times 189$	1.52	0.43	8.0	0.43	1.88	–	<i>ir</i>	17
w) num: P+E no-slip rigid top Eul. $s = 2$	$384 \times 189$	1.52	0.43	8.0	0.43	1.57	–	<i>ir</i>	12
x) num: P+E spectral anal	$640 \times 295$	1.52	0.7(0.4)	8.0	0.43	1.47	–	–	13
y) num: P+E irr forcing	$384 \times 189$	1.52	0.43	8.0	0.43	1.57	–	0.4	60
r1) num: P+E	$640 \times 295$	1.52	0.7(0.4)	8.0	0.43	1.47	> 20 – 30	0.3	14
r2) num: P+E	$640 \times 105$	1.52	0.7(0.4)	8.0	0.43	1.47	> 10 – 15	0.3	13
r3) num: P+E	$640 \times 53$	1.52	0.7(0.4)	8.0	0.43	1.47	–	–	–

Table 4.2: Quantitative comparison of the mean-flow oscillations in the 3D laboratory experiments with 2D numerical simulations. Notations are as described in table 4.1. The amplitude of the forcing in the 2D simulations has been reduced by the averaged effect of the 3D membrane shape resulting in  $\epsilon_{eff} = 0.64 \times \epsilon$ .

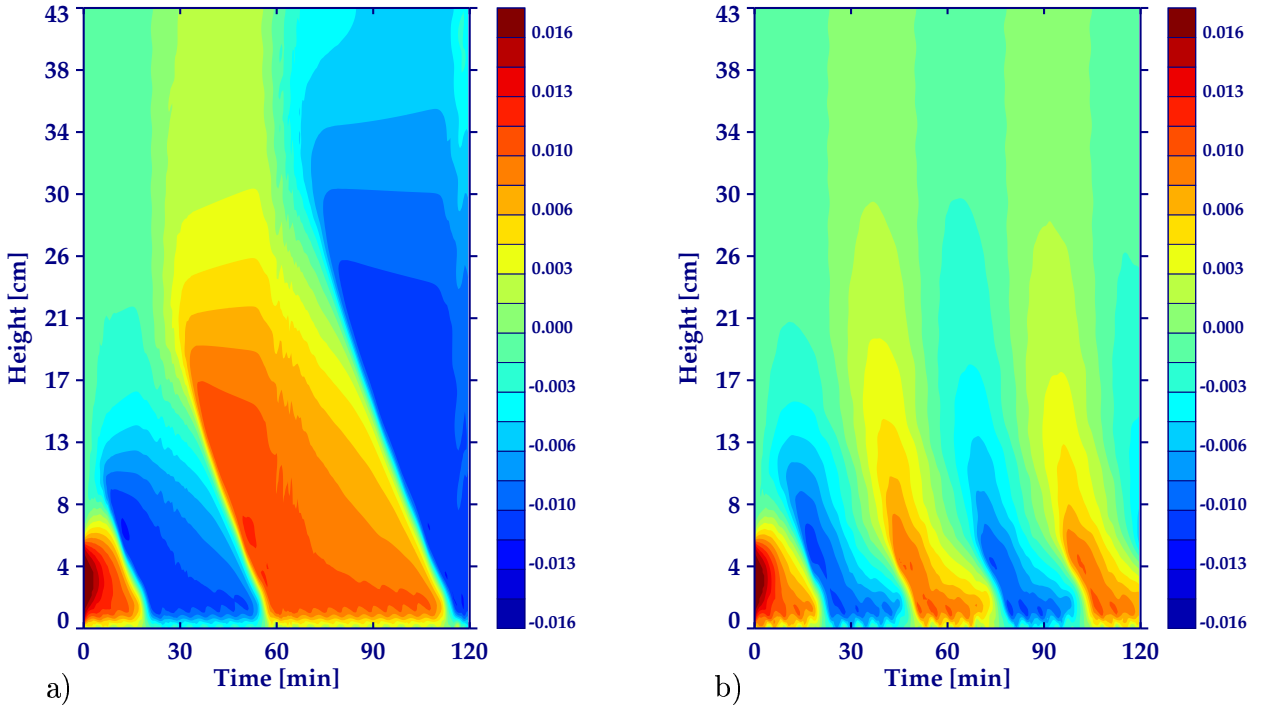


Figure 4.4: Time-height cross-sections of the zonal-mean flow velocity at  $y = L_y/2$  in the 3D numerical simulation in comparison to the corresponding 2D simulation. Plate a shows the 2D and plate b the corresponding 3D result. Units are in  $ms^{-1}$ .

chosen parts of the 16 oscillating membrane chambers oscillated only with half the amplitude. The Kyoto experiment setup is described in detail in [Otoabe et al. \(1998\)](#) and in ([www.gfd-dennou.org, 2004](#)) [ case (d) and (e) in table 4.1]. Several water tank sizes were available for their experimentation (S. Yoden, personal communication). The experiments in [Otoabe et al. \(1998\)](#) exhibit a range of mean flow oscillation periods of 45 – 120 minutes for similar experimental parameters. In particular, a water tank with similar dimensions as in Plumb and McEwan generated periods of approximately 50 minutes in the beginning, indicating further the correctness of the numerical simulations with “perfect” forcing membrane. The numerical analogue of the Kyoto experiment [cases (q) and (r) in table 4.1] compares favourably with the setup described in ([www.gfd-dennou.org, 2004](#)). In particular, the filmed time evolution of the experiment ([www.gfd-dennou.org, 2004](#)) agrees well with the result of the numerical simulation which can be seen in figure 4.5. In all experiments the observed mean flow magnitude is consistent with predictions from linear theory of critical levels (i.e., postulated by the singularity of the Taylor-Goldstein equation (1.17), see also [Drazin and Reid \(1981\)](#), pp.320-324)

$$U_{crit} = \frac{\omega_0}{(2\pi s/L_x)}, \quad (4.3)$$

and it is found that the period of the oscillation is sensitive to  $U_{crit}$ . Note, that despite the existence of explicit viscosity and the time dependence of the mean flow one obtains

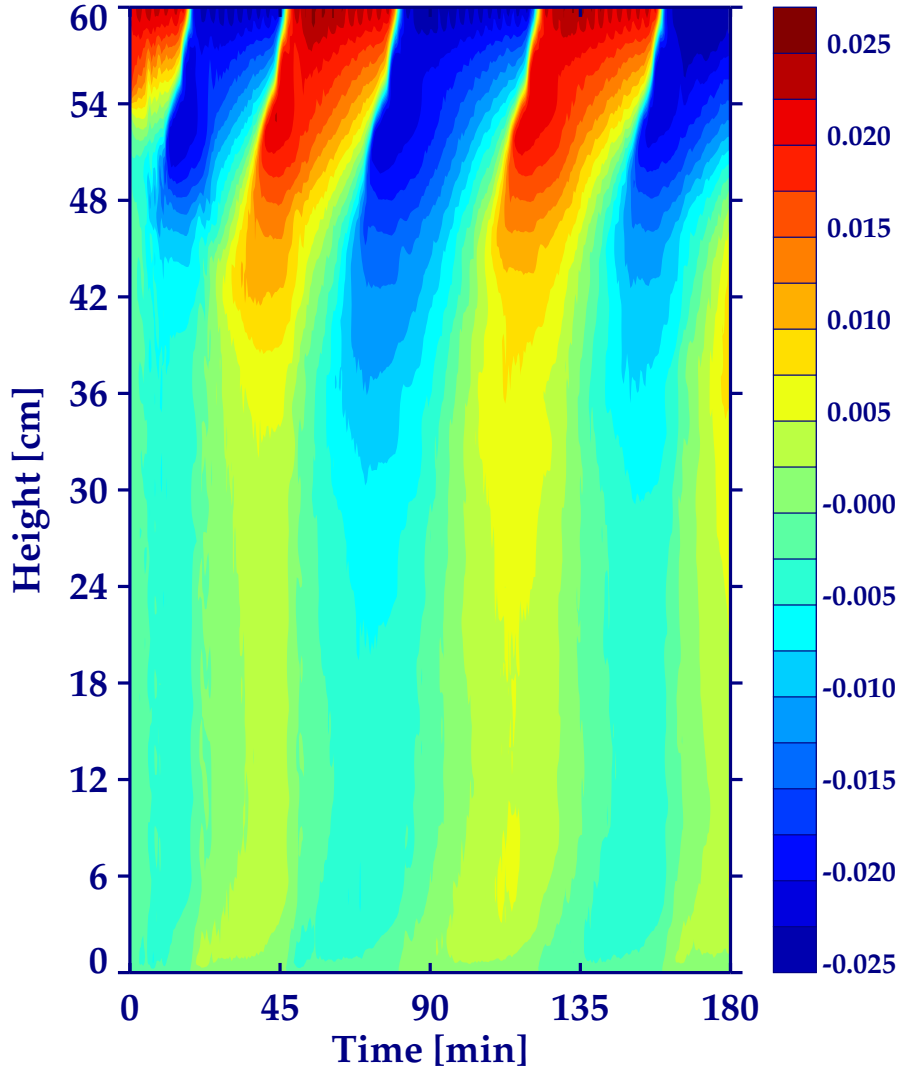


Figure 4.5: Time-height cross-section of the zonal-mean flow velocity at  $y = L_y/2$  in the numerical simulation of the laboratory setup at the university of Kyoto [case (r) in Table 4.1]. The results compare favourably with the animation available at [www.gfd-dennou.org](http://www.gfd-dennou.org) (2004). Units are in  $ms^{-1}$ .

approximately a mean flow magnitude as predicted by (4.3). In three dimensions (Baines, 1995) the mean flow becomes critical to the corresponding waves if

$$\omega_0 = \mathbf{k} \cdot \mathbf{V}_{\text{crit}} = kU_{\text{crit}} + lV_{\text{crit}}, \quad (4.4)$$

where  $\mathbf{k} = (k, l, m)$  denotes the three dimensional wave vector and  $\mathbf{V}_{\text{crit}}$  a background flow of critical magnitude. However, the meridional mean flow  $V$  developing in the simulations is approximately one order of magnitude smaller than the zonal mean flow. Equation (4.4) may however be relevant for variations of the period in the case of the atmospheric QBO.

In section 4.5 some theoretical aspects are further discussed together with a detailed

schematic description of the sequence of events during the flow reversal in section 4.6. In the following paragraphs the parametric and numerical sensitivities are investigated in more detail.

### 4.2.1 Parametric sensitivities

#### Viscosity/diffusivity

Kinematic viscosity  $\nu$  influences both, the vertical extent of the oscillation and the speed of the apparent downward propagation. In particular, lower values of  $\nu$  increase the period and limit the vertical extent which is in agreement with Plumb (1977). This is taken to its extreme in the inviscid case where strongly elongated mean flow layers develop. In this case an oscillation is observed only if forced in the beginning and after that stable layers of mean positive and negative mean flow on top of each other develop, which remain stable. Interestingly, when a friction term of the form  $-\alpha\rho$  with sufficiently large  $\alpha$  ( $1/180\text{ s}^{-1}$ , whereas  $1/1800\text{ s}^{-1}$  was not sufficient) is added on the right hand side of the thermodynamic equation (without any physical motivation at this point), the stratified layers are broken up and a regular mean-flow oscillation starts. Imposing instead an additional friction term of the form  $-\alpha u$  in the momentum equation would suppress even the initially enforced oscillation. Notably in the viscous problem, also too large values of kinematic viscosity (ratio of kinematic viscosity vs. salt diffusivity  $\equiv$  Prandtl number  $< 10$ ) suppress an oscillation, in accordance with an overwhelming effect of the viscous term in equation (1.1) in comparison to the wave momentum flux. There is some indication that the effect of viscosity is primarily to act as an “agent” to enhance the wave momentum flux convergence and to promote the subsequent apparent downward propagation of the shear layer in a region of strong nonlinearity and wave breaking. This effect is in contrast to the stabilising effect when the viscosity term in equation (4.20) dominates.

In comparison, for all investigated cases even large changes in the diffusivity of salt  $\kappa$  had little impact on the oscillation but may be explained through the three orders of magnitude difference between  $\nu$  and  $\kappa$  and their appearance as a sum in the linearised or “slowly varying” equations (e.g. (1.8), (4.34)).

The analysis of the energy budget in section 4.3 together with the spectral analysis of the zonal flow component suggests that numerical dissipation can be discarded as a likely cause for the oscillation onset and the switching to the next phase. It may however contribute to the alteration of the period if the problem is poorly resolved or the numerical scheme inadequate (see section 4.2.2).

#### Stratification

The stratification of the fluid influences and limits the period. In the range  $1.37\text{ s}^{-1} \leq N \leq 1.57\text{ s}^{-1}$  investigated by Plumb and McEwan (1978) their findings  $T \propto 1/N$  can be confirmed. However, when half the Brunt-Väisälä frequency  $N = 0.685\text{ s}^{-1}$  is used there is no mean flow oscillation. After the initially enforced oscillation a single mean flow layer

of uniform magnitude develops. However, it may be possible that the simulation was not continued long enough to find another oscillation with an unproportionally (and not twice) long period (beyond the integration time of 6 hours, where the computation was stopped due to the computational expense).

The qualitative influence of vertically varying stratification has been investigated by means of two layers with a continuous but sharp transition between the two stratification regimes. In both cases, stronger stratification in the upper or in the lower layer, it is found that the internal gravity waves reflect and interfere with the incoming waves resulting in zonal mean-flow generation. The corresponding influence on the period is similar as in the case of rigid boundaries or the influence of a non-perfect artificially placed absorber at the boundary. The findings with respect to wave reflection at the interface of differently stratified fluids agree well with laboratory experiments (Koop, 1981) and theory (Baines, 1995). It is conjectured from this sensitivity that in the atmosphere continuous changes in stratification change the period length of the QBO. Furthermore, the change in stratification at the interface between the stratosphere at the stratopause may limit the vertical extent of the equatorial QBO through reflection and wave interaction. However, observations are still very limited and inaccurate in this region and disturbed by other phenomena like the semi-annual oscillation to allow the verification of this conjecture. Furthermore, due to the amplitude growth of wave disturbances in the upper atmosphere wave breaking may be an equally likely vertically limiting mechanism.

### The external forcing

The shape and amplitude ( $s, \epsilon$ ) of the initial forcing is important for the period. In particular one finds the period  $T \propto 1/\epsilon$ . The findings are in agreement with Plumb (1977). Some of the differences between 2D and 3D with respect to the oscillation period can be explained through the application of an averaged effect of a particular 3D membrane shape translating into a smaller effective  $\epsilon$  (at least for the initial reversals).

There is considerable uncertainty with respect to the forcing of the atmospheric QBO. Therefore, the effect of various combined wave-number/frequency forcing pairs on the oscillation period have been explored. When a mixture of various forcing frequencies or a mixture of horizontal wave-numbers with constant frequency is used, the highest critical mean flow velocity that is reached for any of the participating waves or frequencies dominates the mean flow oscillation period. This is also the case when one mixes both wave-numbers and frequencies in the same simulation, where the mean flow oscillation period behaves highly non-regular until  $U_{crit}$  for the highest possible  $U = \omega/k$ -combination is reached. This can be seen in Figure 4.6 where the system was forced with ( $s = 4, \omega_0 = 0.43s^{-1}$ ), ( $s = 8, \omega_0 = 0.37 s^{-1}$ ), and ( $s = 16, \omega_0 = 0.31 s^{-1}$ ). Initially the flow becomes critical to the higher wave-number/lower frequency pairs since the required mean flow magnitude is lower. But when the mean flow reaches a critical magnitude equivalent to  $U = 0.43/(2\pi 4/L_x)$  only these waves dominate the mean flow oscillation. It should be noted, that the shorter (with respect to wave-length) waves have larger phase speeds. It is however not that these shorter waves create a critical mean flow layer through wave

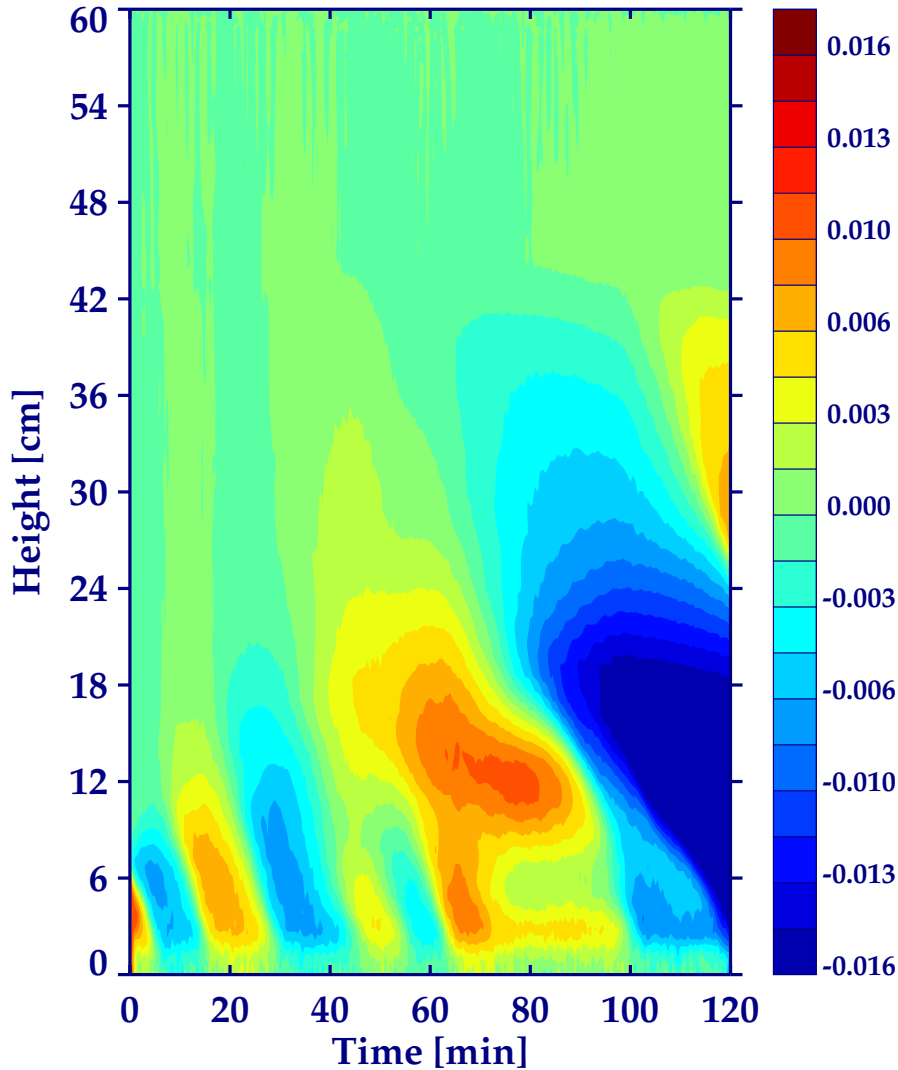


Figure 4.6: Time height cross section of the zonal mean flow for a mixed wavenumber/frequency forcing with  $(s = 4, \omega_0 = 0.43 \text{ s}^{-1})$ ,  $(s = 8, \omega_0 = 0.37 \text{ s}^{-1})$ , and  $(s = 16, \omega_0 = 0.31 \text{ s}^{-1})$ .

breaking somewhat ahead of the longer waves, but rather they form mean flow layers that are critical to themselves. As this happens well below the observed formation of a critical mean flow for the longer waves, the influence of the shorter waves on the initial mean flow development aloft is negligible, since they do not reach as high due to the existence of their “own” critical layers. Once the larger mean flow propagates downward all critical layers for shorter waves disappear and a single dominant oscillation (driven by the longer waves) remains. In another experiment it is verified that when the wave interference cannot generate a sufficiently large mean flow for a particular  $(s, \omega_0)$  combination, the corresponding waves appear to play no role in the generation of the mean flow oscillation. The result has also been confirmed for odd (non-multiple) wavenumber frequency pairs.

Note, that other waves may change the mean flow magnitude locally but do not alter the

main oscillation period until the mean flow becomes critical for them. However, this may never happen as in the case (m) of table 4.2, where the period continues to be dominated by  $(k = 2\pi 8/L_x, \omega = 0.37 \text{ s}^{-1})$  and not  $(k = 2\pi 4/L_x, \omega = 0.43 \text{ s}^{-1})$ . In contrast, when multiple combinations  $\omega_1/k_1 = \omega_2/k_2 = \omega_3/k_3 = 0.013 \text{ m s}^{-1}$  with  $(\omega_i, s_i) = (0.43 \text{ s}^{-1}, 8) = (0.645 \text{ s}^{-1}, 12) = (0.172 \text{ s}^{-1}, 3.2)$  exist, all waves contribute to the apparent downward propagation and the resulting oscillation has a much shorter period due to the increased availability of momentum carried by the waves.

In another experiment an irregularly shaped forcing of four oscillating mountains has been imposed of the form

$$z_s(x, y, t) = \sum_i z_{si} \sin(\omega t + \phi_i) = \sum_i \epsilon_i \frac{1}{2} (1 + \cos(\pi r_i)) \sin(\omega t + \phi_i) \quad (4.5)$$

with the same frequency  $\omega = 0.43$ , and  $r_i = |x - x_{0i}|/a_i$  with  $(x_{0i}, a_i, \epsilon_i) = (0.225, 0.15, 0.008), (0.5, 0.2, 0.011), (0.85, 0.17, 0.009), (1.25, 0.19, 0.013)$ . The oscillations of the individually distributed (arbitrarily shaped) cosine mountains were shifted by a continuous phase  $\phi_i = (i - 1)\pi/4$ . Also in this case a long period mean flow oscillation is generated. It is conjectured that in resemblance of convectively forced gravity waves in the atmosphere a somewhat random forcing is able to create a regular mean flow oscillation. Interestingly from a numerical point of view, the integrability condition of the (incompressible) Boussinesq setup has been maintained by shifting the height of the rigid upper boundary in this simulation by the equivalent residual volume (or surface area in 2D) of the lower boundary disturbance. Without the time-dependent coordinate transformation of the upper boundary a more complicated inflow/outflow upper boundary would have to be designed for this (arbitrary shape) setup.

These results may elucidate the combination of waves responsible for the atmospheric QBO. In the atmosphere only the mean flow  $U$  is known but can be matched in principle by many possible  $\omega_i/k_i$  combinations. It remains to be seen if it is possible to identify dominant pairs, i.e. a spectrum of waves with the same  $\omega_i/k_i = \text{const}$  relation responsible for the atmospheric oscillation.

It is also interesting to note that a membrane shape with  $s = 2$  and otherwise unchanged parameters (the depth of the tank has been increased by a factor of 4 to obtain a similar vertical wave number) does introduce a strong positive wave momentum transfer to the mean flow but only a small negative mean flow (both layered on top of each other). It does not initiate an oscillation even if a positive mean flow is enforced initially. The reason for no oscillation (after 4.5 hours of simulation) may be given by equation (4.3) with  $\omega_0 = 0.43 \text{ s}^{-1}$ ,  $s = 2$  and the fact that the observed mean flow speed never reaches the necessary ‘‘critical’’ magnitude. It is speculated that this is due to insufficient amplitude of the forcing membrane in this case.

## 4.2.2 Numerical sensitivities, linearisation and boundary effects

It is found that initially an asymmetric excitation is required to start the oscillation. This may be as small as asymmetrically accumulated numerical errors, as in the case, where a



bug in the parallelisation created a continuous but tiny asymmetry in the zonal periodicity. Without initial noise or other asymmetry the simulation with a forcing amplitude  $\epsilon = 0.008 m$  failed to initiate an oscillation. However, in a 3D simulation with twice the forcing amplitude,  $\epsilon = 0.016 m$ , an asymmetry develops after only 20 minutes and a mean flow oscillation starts. Because of the earlier results it is speculated that in the latter case the increased nonlinearity (turbulence) induces either a numerically enforced asymmetry or an inherent asymmetry of the nonlinear terms. In any case, it indicates that a small excitation suffices, whether resulting from the inherent nonlinearity or from an external source.

In some 2D cases, random initial noise accelerated the onset of the oscillation but the onset was equally dependent on different numerical approximations. Substantial variations in the onset of the oscillation are found for example with first order accurate advection which starts an oscillation almost immediately (albeit an unrealistic period and time evolution). Variations in the onset were also found between semi-Lagrangian and flux-form Eulerian advection.

Numerical sensitivities with respect to the period are found in particular when using more diffusive numerical methods. Increased implicit diffusion results in shorter periods. The same is true for the comparison between the flux-form Eulerian compared to the semi-Lagrangian approach (see Smolarkiewicz and Margolin (1993) and Smolarkiewicz and Pudykiewicz (1992) for details of the implementation), where the semi-Lagrangian advection produces a marked shorter and irregular period. This can be seen in the comparison of the energy budgets of the simulations using a Eulerian (figure 4.9) or a semi-Lagrangian (figure 4.10) advection scheme. The corresponding time-height cross sections are shown in figure 4.7 and 4.8, respectively.

The results were not very sensitive to the chosen numerical accuracy of the pressure solver. However, when the accuracy is reduced to  $10^{-3}$  and only a single iteration is enforced to obtain convergence the period of the mean flow oscillation distorts and becomes much larger than in the accurate solution. Also an explicit vs. implicit solution procedure with respect to the internal gravity waves has been analysed. In the explicit case full  $\rho$  is advected whereas in the implicit case only the perturbation  $\rho'$ . This influences the numerical solution procedure in the implicit case due to the appearance of the convective derivative in the thermodynamic equation. Here, this equation has to be solved simultaneously with the momentum equation (see the appendix in Smolarkiewicz et al. (2001) for details). The same time-step was used for both integrations. The explicit solution gives only a weak and distorted oscillation period similar to the lower accuracy solution above. Notably, doubling the vertical resolution in the explicit case almost recovers the implicit solution. From the comparison of the waves generated in both solutions it is concluded that the dispersion of the waves is little effected by the implicit calculations but the explicit solution procedure is inferior in accuracy.

It is evident that sufficient resolution is required in particular in the vertical to resolve the initiating internal gravity waves, otherwise no oscillation is observed. This necessitates of course the knowledge of the waves, responsible for the generation of the stratospheric equatorial QBO. Resolution changes appear to impact mainly the speed of the apparent

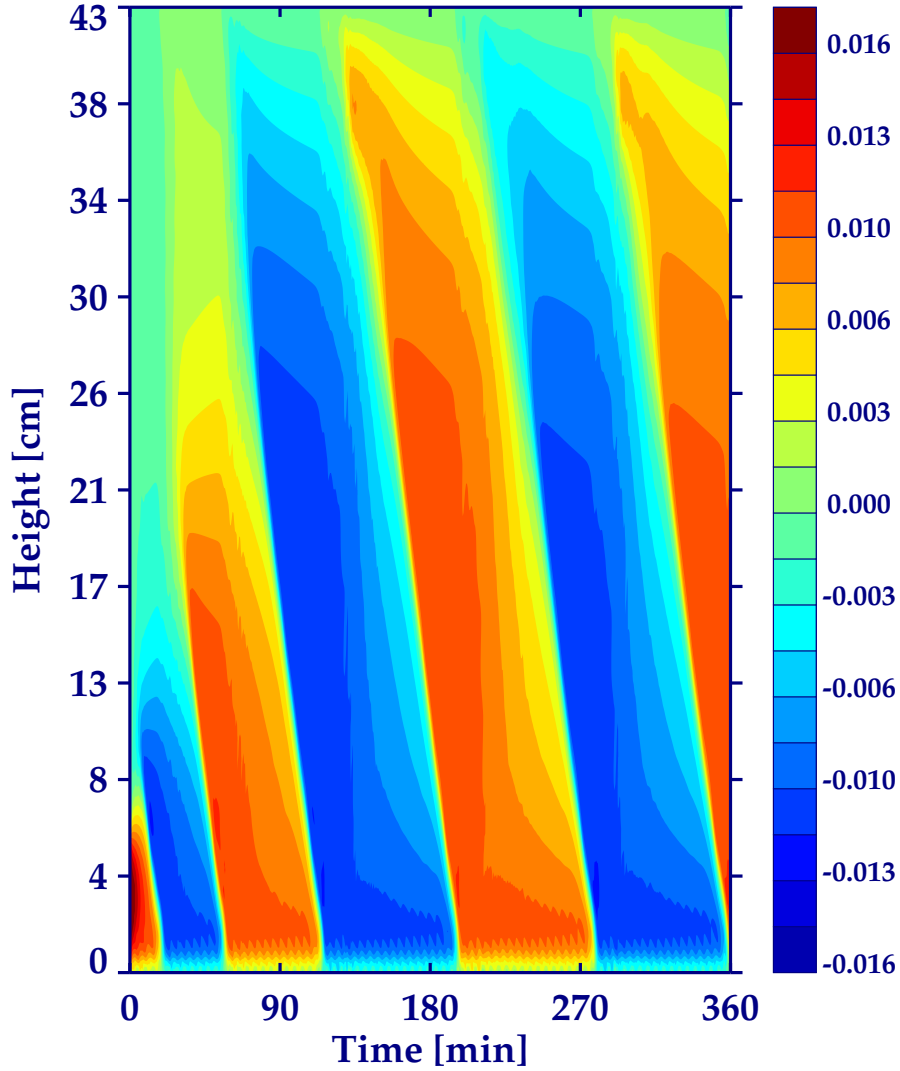


Figure 4.7: Time-height cross-section of the zonal-mean flow velocity in the 2D numerical simulation using a noslip rigid upper boundary with a flux-form Eulerian advection scheme (see table 4.2 for details). The onsets of the next mean flow reversal can also be identified in the evolution of transient kinetic energy in Figure 4.11 and in the evolution of available potential energy in Figure 4.9 indicating the dynamical activity of first decreased and then increased diapycnal mixing during those periods.

downward propagation which may relate to a better representation of the ratio of dynamic and viscous scales. Increasing horizontal and vertical resolutions increases the period up to 20-30% in the simulations up to a 'saturation threshold' after which the mean flow oscillation period is more or less invariant to resolution change (which is found to be the case at  $n = 384$  and  $l = 189$  discounting the effect of the near membrane boundary layer, see discussion below). All simulations in table 4.2 and 4.1 have been conducted with resolutions in excess of this 'saturation threshold'.

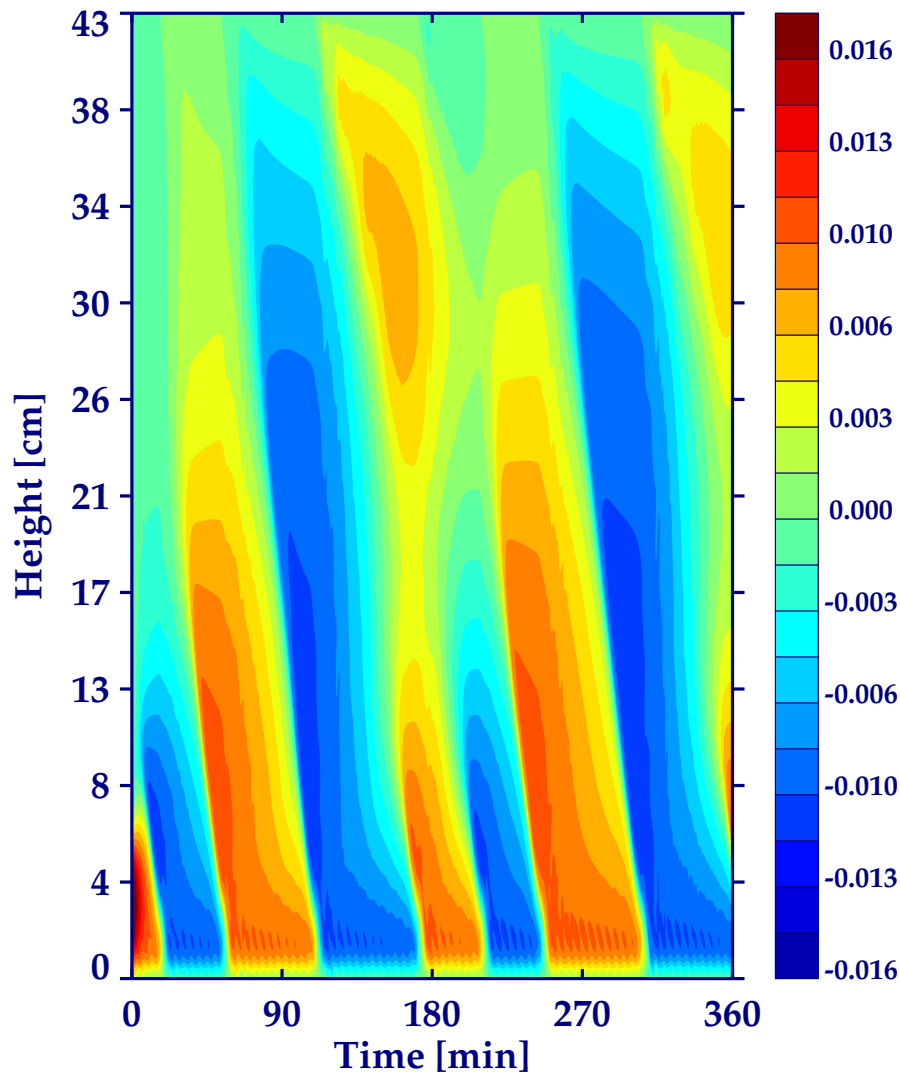


Figure 4.8: Time-height cross-section of the zonal-mean flow velocity in the 2D numerical simulation using a noslip rigid upper boundary with a semi-Lagrangian advection scheme (see table 4.2 for details). The onsets of the next mean flow reversal can also be identified in the evolution of transient kinetic energy in Figure 4.11 and in the evolution of available potential energy in Figure 4.9 indicating the dynamical activity of first decreased and then increased diapycnal mixing during those periods.

The influence of linearisation of the equations has also been investigated in the numerical model. It is interesting to note that the same setup with a linearised advection operator does not initiate an oscillation. If restarted from a fully developed oscillation with a linearised advection operator and constant mean flow, the oscillation does not continue. Further, if the mean flow from a previous fully developed oscillation run is used in a subsequent linearised setup, no oscillation develops either. Finally, to investigate in what way the developing vertical spectrum of waves plays a role a band-pass filter has been applied

on the same restart data for all higher vertical wave-numbers. If the non-linear integration is continued from this restarted state, the mean flow oscillation continues without delay. These results indicate some of the limitations of linear theory with time-independent background shear and stress the importance of non-linear interactions for this phenomenon.

In 2D the geometry of the vertical domain limits the period. One experiment has been conducted with a very deep tank (3m) in which the depth of the oscillation and, due to the extended apparent downward propagation of the mean flow, the period grew until the top of the tank was reached. The growing “steps” visible in this simulation as well as the beginning of any 2D simulation (see for example figure 4.4) are believed to result from the distortion of the waves by the mean-flow up to the height of the previous “step”. Above, internal wave interaction takes place as before and spatial interference of the waves dominates which lets the next “step” grow up to the next spatial position of a maximum in the mean flow where  $U_{crit}$  is reached.

In two dimensions, the boundary conditions influencing wave reflection can alter the period substantially depending on the geometry of the domain and the propagation speed of the contributing internal gravity waves. For simulating non-reflecting conditions It has been found beneficial to apply the absorber only on zonal wind but not on density perturbations providing least impact on the interior domain.

The comparability of the obtained numerical results to the periods in the Kyoto experiments ([www.gfd-dennou.org](http://www.gfd-dennou.org), 2004; Otobe et al., 1998) and the differences with respect to the original laboratory experiment of Plumb and McEwan have been further investigated. From table 4.1 one finds two main differences: the setup of the Kyoto experiment in [www.gfd-dennou.org](http://www.gfd-dennou.org) (2004) used an approximately twice larger domain ( $2L_x, 2L_y$ ), and the membrane is mounted at the top of the water tank. The equivalent numerical results have been obtained with either a no-slip [case (q) in table 4.1] or a free-slip [case (r) in table 4.1] boundary condition at the oscillating membrane and a no-slip condition at the rigid bottom of the water tank. The same flow and forcing parameters as in the laboratory have been used. The domain size influences the wave-length of the forcing and the effective curvature of the water tank. The curvature is ignored in the numerical experiments but the relatively stronger curvature in the original Plumb and McEwan setup may play a role. A numerical test with an approximated beta-plane effect did not change the period significantly. However a better comparability of simulated and laboratory results for larger annuli suggests that curvature effects may be worth investigating further in the future (see Read et al. (1997) for a discussion). From the investigated sensitivities it is concluded that only large and cumulative changes ( $> 10$  percent) in stratification, forcing frequency and amplitude may explain the difference, but this would imply a measurement error in the original experimental setup by Plumb and McEwan which is rather speculative. However, there is a strong sensitivity to the forcing wave-number of more than  $\propto k^3$ , indicated by the experiment, where a doubling of the domain increases the period by a factor of 10. This suggests that a small uncertainty in the realization of the forcing membrane ( $\approx 6$  percent equivalent to one or two of the oscillating sixteen chambers having less amplitude) could explain the obtained difference. Using the movies of both experiments and comparing the different laboratory realizations of the membrane in the Kyoto case and the

original Plumb and McEwan case, the latter appears to have a less exact shape, which supports this speculation. A simulation with an “imperfect” membrane shape [case (v) in table 4.1] results in good comparability to the original Plumb and McEwan setup and is shown figure 4.2. However, the influence of the forcing membrane shape is found to be less important with lower forcing frequency and larger amplitude [case (x) and (y) in table 4.1] and the observed zonal mean flow oscillation period (Fig. 11 in (Plumb and McEwan, 1978)) deviates from the numerical simulations.

Also the choice of the boundary conditions in the numerical simulations influences the period. For example in the Kyoto case, a free-slip condition at the oscillating membrane results in a relatively shorter period compared to a no-slip condition. The difference in the simulations is found to be 15 – 25 minutes. While not significant in comparison to the influence of changes in the forcing wave-length, it is not negligible. This is further investigated by examining the structure of the boundary layers in free-slip and no-slip simulations of only the boundary layer region. From those simulations the lateral (meridional) width of the boundary layer with no-slip is approximately 1 cm near the walls and has no effect on the solution in the middle of the tank. With zero stratification the boundary layer above the oscillating membrane grows to approximately 5 cm after a few minutes of simulation. This is not observed when examining the movies of the laboratory experiments, where there appears to be hardly any boundary layer. The simulation of the near membrane boundary layer with stratification included and no-slip boundary condition exhibits a varying boundary layer of approximately 0 – 1 cm depth. Repeating the same simulation with a five times higher resolution confirms the same result. Therefore two conclusions can be drawn. First, the stratification appears to reduce the depth of the boundary layer. Further, the resolution enhancement does not alter the boundary layer depth or structure, validating the chosen resolution for the direct numerical simulation (DNS). It is interesting to note, that after several hours a lack of stratification was observed in the near membrane layers (S. Yoden, personal communication), which may explain an increase in the observed zonal mean flow oscillation period, similar to the difference of no-slip (i.e., with a boundary layer) and free-slip (i.e. no boundary layer).

The influence of the upper free surface in the Plumb and McEwan experiment has been investigated by assuming a free-slip rigid lid or an absorbing region, but both have negligible influence on the period. Also the possibility of using a (free-slip) shallow water solution at the top of the domain, similar to the experiment described in section 3.3, has been investigated. However, the laboratory experiments show little if any movement of the upper boundary which is confirmed by the high resolution solution of the non-linear shallow water equations with zero forcing wind, which essentially remains flat. In Nature the effects of surface tension and the viscosity of the water further dampen any arising oscillations at the upper surface. Given the oscillating topography, the numerical integration of the non-linear shallow water equations develops indeed tiny, fairly constant amplitude (1-2 orders of magnitude lower than the original forcing) high-frequency surface oscillations after a long time. It is not clear if these are physical or numerical artifacts. If some numerical diffusion or a  $2\Delta x$ -filter is introduced these are suppressed and the surface remains flat. This implies that a flat rigid lid is a reasonable approximation in three-dimensions.

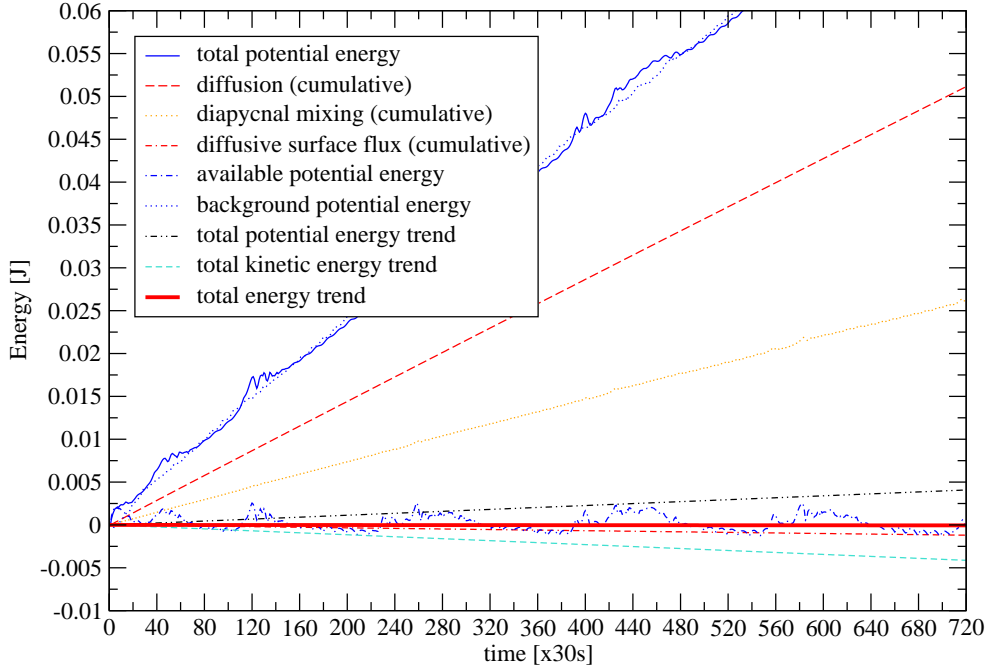


Figure 4.9: Potential energy budget for the Eulerian advection case. The total, available, and background potential energy are shown together with the irreversible cumulative effects of diffusion. Trends of total, kinetic and potential energy are also shown. See the text for more details.

### 4.3 Energy budget

In the following an energy budget analysis is performed to ensure the energetically accurate incorporation of the external forcing applied through the oscillating membrane. Furthermore, it is tried to clarify the role of numerical dissipation for the onset and the development of the mean flow oscillation.

The potential energy of the density stratified Boussinesq fluid is defined as

$$E_p = g \int_V \rho z dV. \quad (4.6)$$

It should be noted that in the following calculations and figures not  $\rho$  but  $\rho - \rho_e$  was used, since the absolute change of potential energy is small, but the perturbation is nevertheless found to be relevant to the flow evolution. The kinetic energy is given as

$$E_k = \frac{\rho_0}{2} \int_V (u^2 + v^2 + w^2) dV. \quad (4.7)$$

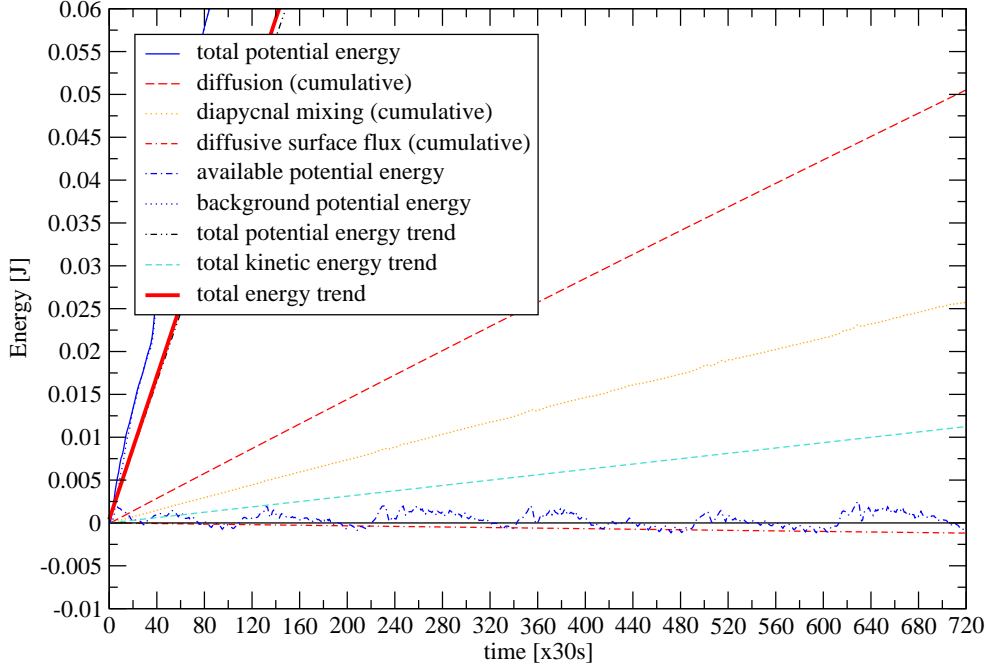


Figure 4.10: Potential energy budget for the semi-Lagrangian advection case. The total, available, and background potential energy are shown together with the irreversible cumulative effects of diffusion. Trends of total, kinetic and potential energy are also shown. See the text for more details.

An equation for the time rate of change of kinetic energy can be derived by taking the scalar product of the momentum equation in (1.2) with the wind vector  $\mathbf{v}$  and the definition (4.7) (see Gill (1982), Winters et al. (1995) and references therein):

$$\frac{d}{dt}E_k = - \oint_S [p\mathbf{v} + \frac{\rho_0}{2}\mathbf{v}(u^2 + v^2 + w^2) - \mathbf{v} \cdot \boldsymbol{\tau}] \cdot \hat{\mathbf{n}}dS - \int_V g\rho wdV - \mathcal{D}. \quad (4.8)$$

Here the first term on the right hand side gives the reversible rate of change of kinetic energy from pressure work and advection, and the irreversible viscous diffusion of energy across the bounding surface  $S$ . The second term denotes the reversible exchange with potential energy via buoyancy and the last term  $\mathcal{D}$  symbolises the irreversible exchange of kinetic to internal energy through viscous dissipation. In this thesis the total effect of viscosity is computed as a volume integral of the viscous term  $\int_V \mathbf{v} \cdot \nabla \cdot \boldsymbol{\tau}$ . Similarly, an evolution equation for potential energy (4.6) is derived from the continuity equation and

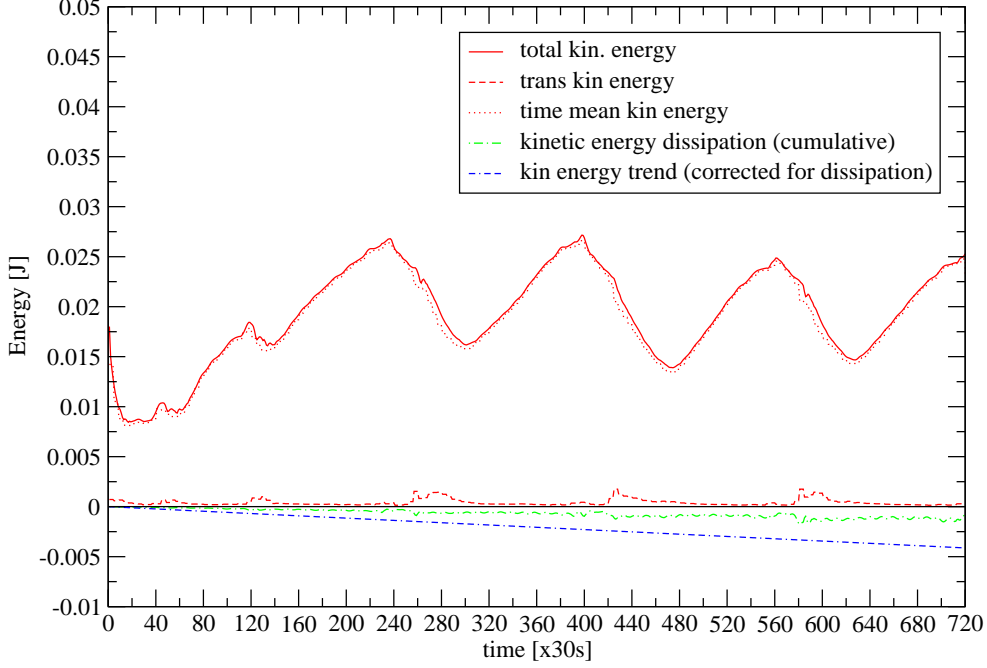


Figure 4.11: Kinetic energy budget. The total, time mean, and transient kinetic energy are shown together with the irreversible, cumulative, viscous dissipation effect. The decaying trend of total kinetic energy is also shown. See the text for more details.

$gz$  times the thermodynamic equation in (1.2):

$$\frac{d}{dt}E_p = - \oint_S gz \rho \mathbf{v} \cdot \hat{\mathbf{n}} dS + \int_V g \rho w dV + \kappa g \oint_S z \nabla \rho \cdot \hat{\mathbf{n}} dS - \kappa g A_{xy} (\langle \rho_{top} \rangle_{xy} - \langle \rho_{bottom} \rangle_{xy}). \quad (4.9)$$

Here, the first two terms on the right hand side denote the reversible change of potential energy via the advective flux through the bounding surface  $S$  and via buoyancy. The last two terms specify the irreversible rate change due to diffusive mass fluxes across the surface  $S$  and the conversion rate from internal to potential energy. In the following analysis the total effect of diffusion is computed from the volume integral  $\int_V gz \nabla^2 \rho$ . The diffusive surface flux is then determined from the difference of the total effect of diffusion and the last term on the right hand side in (4.9).

As pointed out by [Winters et al. \(1995\)](#) the evolution equation (4.9) does not readily allow to identify all reversible and irreversible dynamic processes, in particular the translation of buoyancy. Instead, [Winters et al. \(1995\)](#) make use of a reconstructed reference state of minimum gravitational potential energy to separate diabatic and adiabatic processes.



An analytic justification of this separation is given in [Winters et al. \(1995\)](#). Numerically, an approximation of this reference state at every time step is obtained by sorting all discrete fluid elements and stably restratifying with heaviest elements at the bottom and lighter elements above. Using the density distribution  $\rho_*$  obtained in this way, the background potential energy can be computed as

$$E_b = \int_V gz\rho_* dV \quad (4.10)$$

and the so called available potential energy  $E_a$  can be obtained using (4.6) and

$$E_p = E_b + E_a. \quad (4.11)$$

Figure 4.9 summarises the potential energy budget for the Eulerian advection case. Trends of total, kinetic and potential energy are also shown for a six hour integration period. Comparing Figure 4.9 with the time-height evolution of the mean flow in Figure 4.7 one can identify the points of flow reversal by increased values of available potential energy.

The splitting (4.11) into background and available potential energy enables the derivation of an evolution equation for the background potential energy of the form

$$\frac{d}{dt}E_b = S_{adv} + S_{diff} - \kappa g \int_V \left( \frac{d\rho_*}{dz} \right)^{-1} |\nabla\rho|^2 dV, \quad (4.12)$$

where  $S_{adv}$  and  $S_{diff}$  denote advective and diffusive fluxes across the bounding surface  $S$  and the last term on the right hand side gives the irreversible rate of change of potential energy due to material changes of density within the volume  $V$ , also called diapycnal mixing ([Winters et al., 1995](#)).

The energy diagram in Figure 4.12 summarises the different forms of energy in the Boussinesq system and their corresponding reversible and irreversible exchanges and external fluxes. Potential energy and kinetic energy are defined in (4.6) and (4.7), respectively. The external energy symbolises the storage reservoir of externally induced input to the flow. Internal energy denotes the storage of energy within the fluid, with irreversible fluxes due to viscous dissipation of kinetic energy ( $\mathcal{D}$  in equation (4.8)) and irreversible conversion from internal to potential energy due to the diffusivity of salt (last right hand side term in equation (4.9)).

In [Laprise and Peltier \(1989a,b\)](#) an alternative approach is discussed, where fluid mixing and potential to kinetic energy exchanges are expressed in terms of the buoyancy flux and averages over slow and fast time scales. It is commented in [Winters et al. \(1995\)](#) that this approach does not necessarily allow an analysis with separation into reversible and irreversible fluxes. In fact in the application of severe downslope windstorms ([Laprise and Peltier, 1989b](#)) the authors encounter themselves difficulties to calculate meaningful fluxes for all terms involved. Following their approach the time mean kinetic energy is calculated as

$$\overline{K} = \frac{1}{2} \langle \overline{u^t u^t} \rangle_{xy}, \quad (4.13)$$

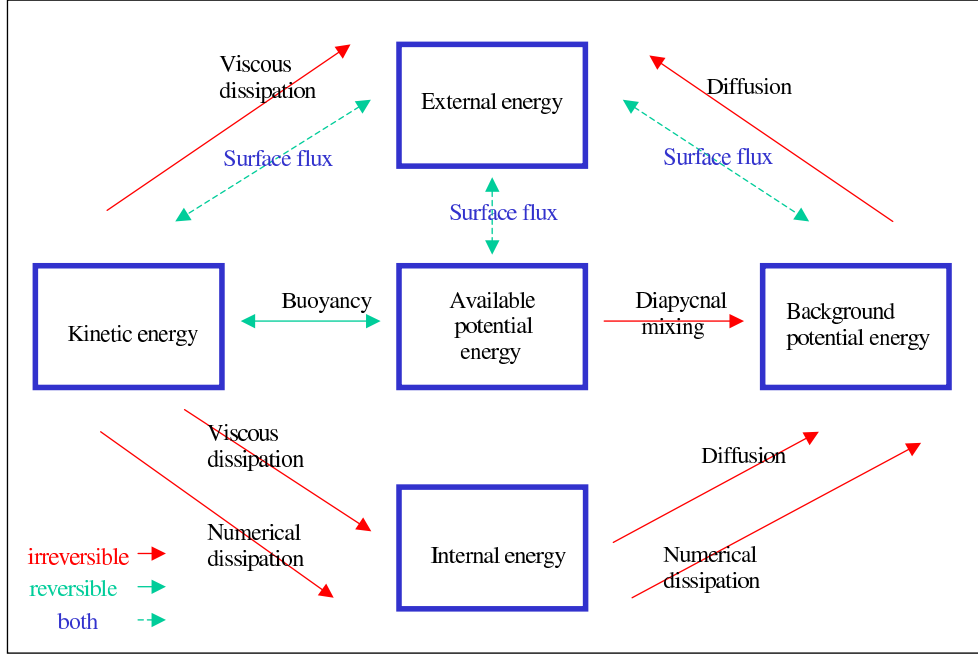


Figure 4.12: Energy diagram for density stratified Boussinesq flow adapted from [Winters et al. \(1995\)](#). The energy within a fixed volume is stored as kinetic, available potential, background potential, or internal energy. Energy is input to the flow through surface fluxes. Reversible and irreversible energy exchanges occur through buoyancy flux, diabatic mixing, viscous dissipation, or diffusion.

the transient kinetic energy

$$K' = \frac{1}{2} \langle \overline{u^t} \rangle_{xy}, \quad (4.14)$$

and the exchange fluxes of potential and kinetic energy

$$C_{KP} = C_{\overline{K}P} + C_{K'P} = \langle \overline{w^t \rho^t} g \rangle_{xy} + \langle \overline{w \rho^t} g \rangle_{xy}, \quad (4.15)$$

using running averages over 4 or 8 values for the calculation of the time mean (denoted  $\overline{\phi^t}$ ) and the corresponding fluctuation. The splitting of time mean and transient kinetic energy appears meaningful since it identifies the same points of reversal of the mean flow as the splitting into background and available potential energy. However, the calculation of the exchange rates via (4.15) fails to account for the irreversibility of the exchange via diapycnal mixing.

For the no-slip rigid 2D cases (p) and (r) in table 4.2, the potential and kinetic energies and the cumulative effects of the irreversible rates have been calculated in order to assess the effect of numerical dissipation while accounting for for all physical processes. Figure 4.11 gives an overview of the kinetic energy over a period of 3 hours of simulation, i.e. 432000 time steps. The trend of total energy (the sum of the potential and kinetic energy trends) is shown in figure 4.9 as the thick line. The potential energy trend has been calculated as a linear regression of the residual background potential energy after subtracting the

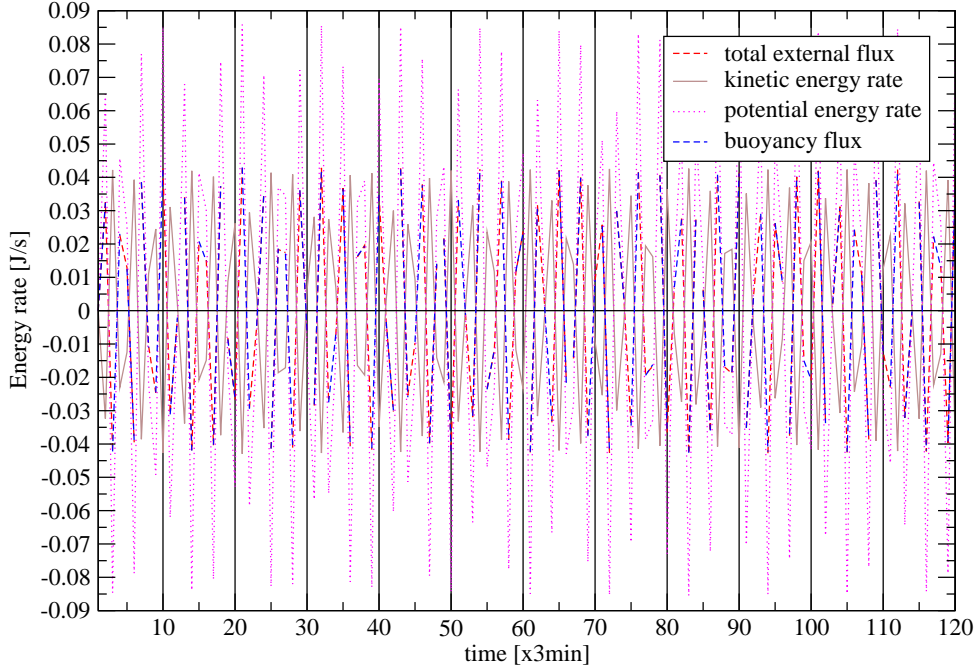


Figure 4.13: Exchange rates of energy. The exchange rates are dominated by high frequency ( $\approx 3$  buoyancy periods per 10 minutes) reversible oscillations. The kinetic energy is of the same size and opposite to the buoyancy flux. The potential energy rate is twice the size of kinetic energy accounting for buoyancy and the advective surface flux of the same size. The irreversible exchange rates are too small to be seen and are visualised through their respective cumulative effect in Figures 4.9 and 4.11.

cumulative effects of dissipation and diapycnal mixing. The kinetic energy trend has been calculated using a linear regression (discarding the first 160 points) of a 130 point running mean of kinetic energy, where the initial value has been subtracted.

After subtraction of all physical contributions the numerical loss of kinetic energy is found to be  $\approx -5. \times 10^{-5}\%$  of the initial kinetic energy per time step. This may be compared with a loss of kinetic energy in the operational forecast at ECMWF of  $\approx -2.7 \times 10^{-4}\%$  of the initial kinetic energy per time step. The loss is compensated by an almost equal amount of numerically generated potential energy growth as can be seen in Figure 4.9. The total energy residual is  $\approx 1. \times 10^{-10}$  per time step which is in the order of round-off errors.

The Eulerian formulation of the model therefore conserves the total energy invariant of the analytic Boussinesq equations (1.2) to the order of round-off errors. This verifies also the negligible amount of any artificial energy source or sink terms other than the external

surface fluxes (via the oscillating membrane) and as described in the diagram 4.12. A summary of the reversible fluxes depicted in the diagram are shown in figure 4.13. It can be seen that the surface flux, calculated via the advective right hand side terms in (4.8) and (4.9), which feeds the available potential energy is nearly equivalent to the buoyancy (the second right hand side term in (4.9)).

The overall accumulated numerical diffusion is approximately four times the natural cumulative viscous dissipation in the Eulerian simulation. However, the instantaneous dissipative rate is negligible compared to the buoyancy exchanges, and the cumulative rate of dissipation appears less relevant since several mean flow reversals happen over the investigated period. Also explicit viscous dissipation and numerical dissipation are likely to differ in the way they are applied locally. Furthermore, if numerical dissipation would be responsible for the oscillation or its onset, the equivalent inviscid simulation would show the same oscillation, which is not the case. However, while the energy analysis suggests that numerical diffusion is not important in this simulation it does not generally clarify the role of numerical dissipation in the development of a mean flow reversal in other simulations. Therefore, the same analysis has been performed for the corresponding simulation using a semi-Lagrangian advection scheme. As can be seen from figure 4.10, the physical irreversible rates are the same but there is a considerable irreversible growth of background potential energy and some (unexplained) growth of the kinetic energy. This additional energy accounted to the different numerical scheme may explain in part the altered flow evolution in figure 4.8 compared to figure 4.7.

## 4.4 Spectral analysis

In this section a detailed spectral analysis of the waves in the numerical simulations is performed to gain insight into the physical processes at the various stages of the mean flow oscillation.

The 2D data for this analysis (case (x) in table 4.2) consists of the horizontal velocity component  $u$  on 295 equidistant vertical levels. The analysis to determine the particular horizontal wavenumber present in each selected level (see figure 4.23) has been done for 9 equidistant heights with a spacing of approximately 4.76  $cm$  ( $\approx 20$  vertical model levels). The data exists in a time-series of 1  $s$  intervals (20 time-steps) for a period of 1800  $s$ . The horizontal resolution is 640 points over a distance of 1.52  $m$ . The simulation was started with a mean-flow at rest. The forcing amplitude is  $\epsilon = 0.008 m$ . Given a sequence of  $n$  complex data values  $z_j$  for  $j = 0, 1, \dots, n - 1$  the discrete Fourier transform is defined NAG (2004) as

$$\hat{z}_k = \frac{1}{\sqrt{n}} \sum_{j=0}^{n-1} z_j e^{(\pm i \frac{2\pi j k}{n})}, \quad k = 0, 1, \dots, n - 1. \quad (4.16)$$

The data is subdivided into 60 intervals of 30  $s$ . First a transformation is applied from physical space to the horizontal wave number space for each time interval and each vertical level. Subsequently, the obtained complex values are transformed to find the distribution

of spectral densities in the vertical for each time-interval. Then the analysis is completed by a transformation in time to find the dominant frequencies. The NAG-library routines *C06EAF* and *C06PCF* are repeatedly used for this purpose. These routines use a variant of the fast Fourier transform (FFT) algorithm described in [Temperton \(1983\)](#). The lower and upper limits of representativeness in spectral space for the horizontal and vertical wavenumbers, and the waves' frequencies, are defined through the given numerical discretisation as  $2\pi/(640 \times \Delta x) < k < 2\pi/2\Delta x$ ,  $2\pi/(295 \times \Delta z) < m < 2\pi/2\Delta z$ , and  $2\pi/(1800 \times \Delta t) < \omega < 2\pi/2\Delta t$ , respectively. Figure 4.14 shows the horizontal wave-number and frequency spectrum for individual time-intervals. A single frequency of  $\approx 0.42 \text{ s}^{-1}$  is dominating the spectrum, which is nearly equivalent to the forcing frequency of the oscillating lower boundary. In the beginning of the simulation both horizontal wave numbers 8 and  $-8$  can be observed in agreement with the shape of the forcing membrane and the resulting standing wave pattern. However, not all levels show the existence of both wave numbers for all time intervals and after the first mean flow reversal only one of them (8 or  $-8$ ) is observed at any one time (except perhaps for the lowest level). The distribution of a particular horizontal wavenumber present in a selected vertical level has been obtained by relating the power spectrum of the individual waves to the maximum power in a given time interval. Only contributing waves with at least 10 percent of this maximum power are shown. The vertical filtering of a particular horizontal wave number, depending on the phase of the mean flow oscillation is evident in figure 4.23.

## 4.5 Theoretical considerations to the QBO analogue

Before proceeding to the precise analysis of the direct numerical simulation in section 4.6 it is instructive to discuss a linear analysis of the internal wave propagation in the laboratory experiment and potential shortcomings of this approach.

The zonal component of the momentum equation in (1.2) in the  $x$ - $z$ -plane is given as

$$\partial_t u + u \partial_x u + w \partial_z u = -\partial_x \pi + \nu (\partial_x^2 + \partial_z^2) u. \quad (4.17)$$

Assuming a  $2\pi$ -periodic domain in  $x$ -direction with corresponding boundary conditions and using the horizontal average operator

$$U(z, t) = \langle u \rangle_x := \frac{1}{2\pi} \int_0^{2\pi} u dx \quad (4.18)$$

while utilising the continuity equation in the form

$$\partial_x u + \partial_z w = 0, \quad (4.19)$$

one obtains the averaged zonal component of the momentum equation as

$$\frac{\partial U}{\partial t} - \nu \frac{\partial^2 U}{\partial z^2} = -\frac{\partial}{\partial z} \langle u'w' \rangle_x. \quad (4.20)$$

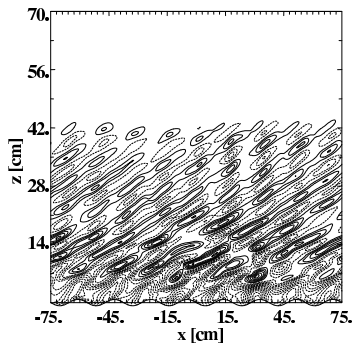
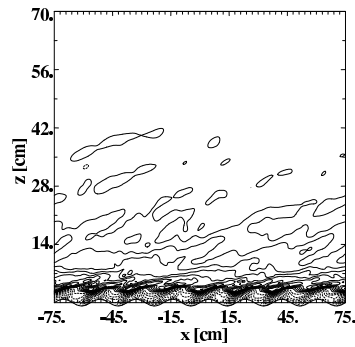
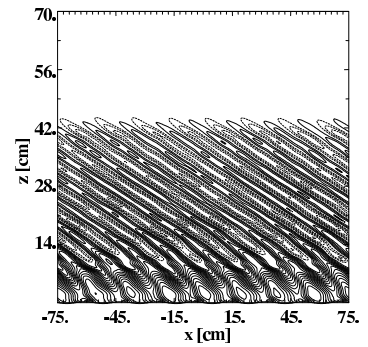
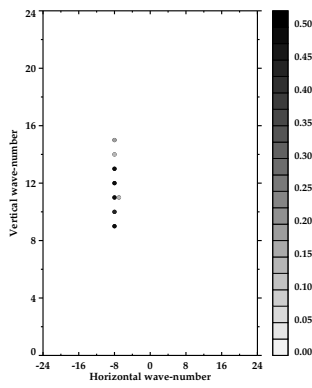
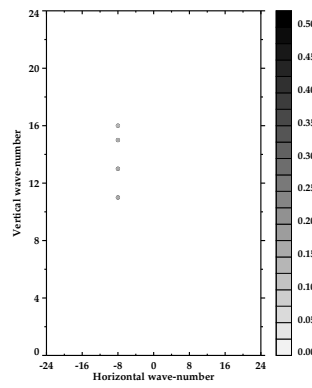
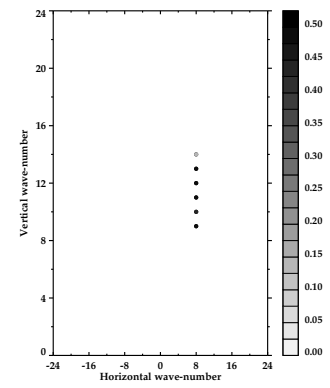
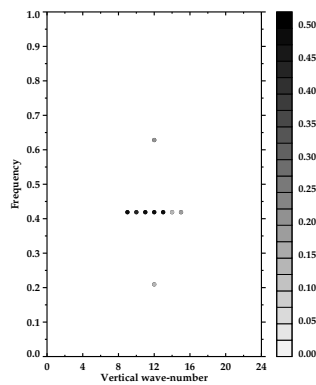
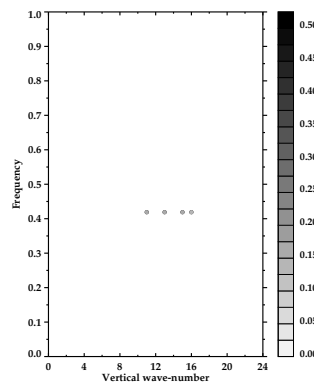
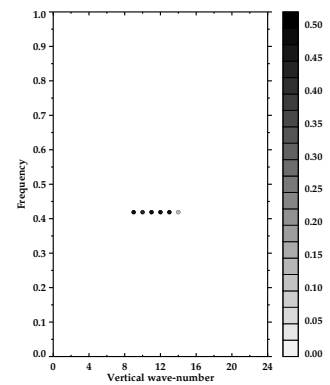
(a)  $t=16$ ,  $s=-8$ ,  $c_x > 0$ (b)  $t=21$ , (almost) none(c)  $t=24$ ,  $s=+8$ ,  $c_x < 0$ (d)  $t=16$ (e)  $t=21$ (f)  $t=24$ (g)  $t=16$ (h)  $t=21$ (i)  $t=24$ 

Figure 4.14: Comparison of zonal wind, horizontal and vertical wave numbers, and dominant frequencies diagnosed at selected time intervals by spectrally analysing the zonal velocity. The waves in plate a travel to the right and the waves in plate c travel to the left.

No approximations have been made in deriving equation (4.20). The right hand side represents the averaged vertical flux of wave momentum, which contributes to changes in the mean flow. It should be noted that viscous dissipation  $\propto \nu \partial^2 U / \partial z^2$  or an additionally imposed (artificial or real) friction  $\propto \alpha U$  may also contribute to a change of the mean flow and may overwhelm the effect of the wave momentum flux. At first, equation (4.20) may appear as a violation of the Eliassen Palm theorem (Eliassen and Palm, 1961), which states the height independence of the vertical flux of horizontal momentum  $\overline{u'w'^x}$ ,

$$\rho_0 \langle u'w' \rangle_x = \text{const.} \quad (4.21)$$

However, as noted by Bretherton (1966), the height independence of the vertical flux of horizontal momentum has been derived under the assumption of a steady state in the absence of wave damping and critical levels; in such cases the theorem is indeed invalid because the waves interact with the time dependent mean flow.

Considering two wave solutions  $A$  and  $B$  of the physical equations (1.4), while neglecting distortions of the wave field by viscosity or a mean flow, both real and imaginary parts are independent solutions of the linear system of equations (Drazin and Reid, 1981). It therefore suffices to consider only the real part  $\Re$  of the relations (1.6),

$$\begin{aligned} u'_A &= \Re \left\{ -\frac{\partial \hat{\psi}_A}{\partial z} e^{ik_A x} \right\} \\ w'_A &= \Re \left\{ ik_A \hat{\psi}_A e^{ik_A x} \right\} \\ u'_B &= \Re \left\{ -\frac{\partial \hat{\psi}_B}{\partial z} e^{ik_B x} \right\} \\ w'_B &= \Re \left\{ ik_B \hat{\psi}_B e^{ik_B x} \right\}. \end{aligned} \quad (4.22)$$

Now the averaged Reynolds flux  $\langle u'w' \rangle_x$  of the two internal waves is calculated, noting that  $\Re\{a\} = (a + a^*)/2$ ,  $\Im\{a\} = (a - a^*)/2i$  and  $(ab)^* = a^*b^*$ , where  $a^*$  denotes the complex conjugate of  $a$ . It should be noted that using the imaginary part instead of  $\Re$ , the same result for the Reynolds flux will be obtained. It would be incorrect to insert the full complex expressions for the wave solutions since one seeks the wave-momentum flux

resulting from either physical solution ( $\Re$  or  $\Im$ ) of the linearised equations. It follows

$$\begin{aligned}
\langle u'w' \rangle_x &= \langle (u'_A + u'_B)(w'_A + w'_B) \rangle_x & (4.23) \\
&= -\frac{ik_A}{4} \left\{ \hat{\psi}_A \frac{\partial \hat{\psi}_A^*}{\partial z} - \hat{\psi}_A^* \frac{\partial \hat{\psi}_A}{\partial z} \right\} - \frac{ik_B}{4} \left\{ \hat{\psi}_B \frac{\partial \hat{\psi}_B^*}{\partial z} - \hat{\psi}_B^* \frac{\partial \hat{\psi}_B}{\partial z} \right\} \\
&\quad - \frac{ik_B}{8\pi} \int_0^{2\pi} \left[ -\hat{\psi}_B^* \frac{\partial \hat{\psi}_A}{\partial z} e^{i(k_A - k_B)x} + \hat{\psi}_B \frac{\partial \hat{\psi}_A^*}{\partial z} e^{-i(k_A - k_B)x} \right] dx \\
&\quad - \frac{ik_B}{8\pi} \int_0^{2\pi} \left[ \hat{\psi}_B \frac{\partial \hat{\psi}_A}{\partial z} e^{i(k_A + k_B)x} - \hat{\psi}_B^* \frac{\partial \hat{\psi}_A^*}{\partial z} e^{-i(k_A + k_B)x} \right] dx \\
&\quad - \frac{ik_A}{8\pi} \int_0^{2\pi} \left[ -\hat{\psi}_A^* \frac{\partial \hat{\psi}_B}{\partial z} e^{-i(k_A - k_B)x} + \hat{\psi}_A \frac{\partial \hat{\psi}_B^*}{\partial z} e^{i(k_A - k_B)x} \right] dx \\
&\quad - \frac{ik_A}{8\pi} \int_0^{2\pi} \left[ \hat{\psi}_A \frac{\partial \hat{\psi}_B}{\partial z} e^{i(k_A + k_B)x} - \hat{\psi}_A^* \frac{\partial \hat{\psi}_B^*}{\partial z} e^{-i(k_A + k_B)x} \right] dx.
\end{aligned}$$

There are several important aspects to be noted. The first two terms on the right hand side of equation (4.23) describing the self-interaction of individual waves, have been already considered by [Plumb \(1977\)](#). He inserted an approximate solution  $\hat{\psi}$  of the Taylor-Goldstein equation (1.17) into the first term of equation (4.23) and used the resulting momentum flux to solve equation (4.20) numerically. However, performing the integration of the remaining cross-terms of  $A$  and  $B$  in equation (4.23), one finds that due to the periodicity condition in  $x$  direction all right hand side terms give a contribution to the wave momentum flux but only in the cases  $k_A = k_B$  or  $k_A = -k_B$ . In the case  $k_A = k_B = k$  one obtains

$$\begin{aligned}
\langle u'w' \rangle_x &= -\frac{ik}{4} \left\{ \hat{\psi}_A \frac{\partial \hat{\psi}_A^*}{\partial z} - \hat{\psi}_A^* \frac{\partial \hat{\psi}_A}{\partial z} \right\} - \frac{ik}{4} \left\{ \hat{\psi}_B \frac{\partial \hat{\psi}_B^*}{\partial z} - \hat{\psi}_B^* \frac{\partial \hat{\psi}_B}{\partial z} \right\} & (4.24) \\
&\quad - \frac{ik}{4} \left\{ \hat{\psi}_B \frac{\partial \hat{\psi}_A^*}{\partial z} - \hat{\psi}_B^* \frac{\partial \hat{\psi}_A}{\partial z} + \hat{\psi}_A \frac{\partial \hat{\psi}_B^*}{\partial z} - \hat{\psi}_A^* \frac{\partial \hat{\psi}_B}{\partial z} \right\}.
\end{aligned}$$

In the case  $k_A = -k_B = k$  one obtains

$$\begin{aligned}
\langle u'w' \rangle_x &= -\frac{ik}{4} \left\{ \hat{\psi}_A \frac{\partial \hat{\psi}_A^*}{\partial z} - \hat{\psi}_A^* \frac{\partial \hat{\psi}_A}{\partial z} \right\} - \frac{ik}{4} \left\{ \hat{\psi}_B \frac{\partial \hat{\psi}_B^*}{\partial z} - \hat{\psi}_B^* \frac{\partial \hat{\psi}_B}{\partial z} \right\} & (4.25) \\
&\quad - \frac{ik}{4} \left\{ \hat{\psi}_A \frac{\partial \hat{\psi}_B}{\partial z} - \hat{\psi}_A^* \frac{\partial \hat{\psi}_B^*}{\partial z} + \hat{\psi}_B \frac{\partial \hat{\psi}_A}{\partial z} - \hat{\psi}_B^* \frac{\partial \hat{\psi}_A^*}{\partial z} \right\}.
\end{aligned}$$

For example, in the simplest case of two internal waves of the form

$$\begin{aligned}
w'_A &= w'_{0A} \cos(k_A x + m_A z - \sigma_A t), & (4.26) \\
u'_A &= -(m_A/k_A) w'_{0A} \cos(k_A x + m_A z - \sigma_A t), \\
w'_B &= w'_{0B} \cos(k_B x + m_B z - \sigma_B t), \\
u'_B &= -(m_B/k_B) w'_{0B} \cos(k_B x + m_B z - \sigma_B t),
\end{aligned}$$



where  $\sigma_A, \sigma_B$  are given by the Boussinesq dispersion relations (cf. equation (1.13)) of wave A and wave B respectively, all self-interaction terms are identically zero. The only contribution to the mean flow results from the interference of the two waves if, and only if  $k_A = k_B$  or  $k_A = -k_B$ . This can be shown by inserting (4.26) into the averaged Reynolds flux divergence  $\langle (u'_A + u'_B)(w'_A + w'_B) \rangle_x$ . Using the addition rules of trigonometric functions  $\cos(k_A x + m_A z - \sigma_A t) = \cos(k_A x) \cos(m_A z - \sigma_A t) - \sin(k_A x) \sin(m_A z - \sigma_A t)$ ,  $\cos(k_A x) \cos(k_B x) = 1/2[\cos((k_A - k_B)x) + \cos((k_A + k_B)x)]$ , and noting that  $2\pi$ -periodic terms do not contribute, one finds for the case  $k_A = k_B \equiv k$

$$\frac{\partial}{\partial z} \langle u'w' \rangle_x = \frac{w'_{0A} w'_{0B}}{2} \left( \frac{m_A^2 - m_B^2}{k} \right) \sin[(m_A - m_B)z - (\sigma_A - \sigma_B)t]. \quad (4.27)$$

An equivalent result has been obtained before by Galmiche et al. (2000) for the inviscid case in which equation (4.20) reduces to

$$\frac{\partial U}{\partial t} = -\frac{\partial}{\partial z} \langle u'w' \rangle_x. \quad (4.28)$$

Solving equation (4.28) with the initial condition  $U(z, 0) = 0$  leads to

$$U(z, t) = \frac{w'_{0A} w'_{0B}}{2k} \left( \frac{m_A^2 - m_B^2}{\sigma_A - \sigma_B} \right) \cos[(m_A - m_B)z - (\sigma_A - \sigma_B)t] - \cos[(m_A - m_B)z]. \quad (4.29)$$

Galmiche further demonstrated that the resulting mean flow given by equation (4.29) can be sufficiently strong to locally develop a zonal mean flow, which can become critical to either wave A or B (Galmiche et al., 2000).

In the more general case equation (1.8) together with (4.20) and (4.24) would determine the solution of internal gravity waves in a Boussinesq fluid under the influence of a self-induced time-varying mean flow. However, the equations are implicit with respect to the mean-flow  $U$ . This problem has been avoided by Plumb considering only the self-interaction of waves and considering only solutions to equation (1.17), derived under the assumption of  $U \equiv U(z)$  (Plumb, 1977). Galmiche avoids the implicitness of the problem by investigating only the inviscid case and postulating that the wave fields to a first approximation are only weakly distorted by the mean flow, justifying the use of the simple Boussinesq dispersion relation  $\sigma$  in the relations (4.26) (Galmiche et al., 2000). While Plumb's approach appears to allow the estimation of the flow evolution in a limited regime, Galmiche's simplifications merely allow qualitative conclusions until the flow becomes critical.

The assumptions of Galmiche and Plumb may be regarded as special cases of a "slowly varying" mathematical approach<sup>4</sup> called WKB(J) approximation (after Wenzel, Kramers, Brouillon and Jeffreys) (Baines, 1995; Gill, 1982). Using this technique, Grimshaw (1975) already noted earlier that waves can cause changes in the mean wind in the absence of an initial shear. He also pointed out that large amplitude internal waves can create sufficient shear which can become critical and cause absorption and "self-destruction" of the originating waves.

---

<sup>4</sup> The WKB approximation is common in optics to mathematically describe the fast propagation of light through a medium with a slowly varying refraction index.

Following [Bretherton \(1966\)](#); [Grimshaw \(1972, 1974\)](#) and summarised in [Baines \(1995\)](#), an evolution equation for the mean flow as a function of wave action may be found. In analogy to the derivation of the energy equation in section 4.3 but using the linearised equations (1.4), multiplying the zonal component of the momentum equation with  $u'$ , the vertical component with  $w'$  and the thermodynamic equation with  $b'/N^2$  and building the sum of all equations gives

$$\frac{\partial \mathcal{E}}{\partial t} + U \frac{\partial \mathcal{E}}{\partial x} + \frac{\partial}{\partial x}(u'p') + \frac{\partial}{\partial z}(w'p') = -\rho_0 \frac{\partial U}{\partial z}(u'w') + \mathcal{D} \quad (4.30)$$

with  $\mathcal{E} = \rho_0/2(u'^2 + w'^2 + (b'/N)^2)$  denoting the local wave energy per unit volume (wave energy density, which is proportional to the square of the wave amplitude), and with  $\mathcal{D} = \rho_0(\nu(u'\nabla^2 u' + w'\nabla^2 w') + \nu u' \partial^2 U / \partial z^2 + \kappa(b'/N^2)\nabla^2 b')$ . Assuming sinusoidal motions of a wave train in a zonally periodic domain one finds from the zonal component of the momentum equation multiplied with  $w'$  the relation

$$\langle u'w' \rangle_x = \frac{k}{\rho_0(\omega_0 - Uk)} \langle w'p' \rangle_x. \quad (4.31)$$

In the inviscid case, zonally averaging equation (4.30) and using the definition of the wave action  $\mathcal{A}$  as

$$\mathcal{A} := \frac{\mathcal{E}}{\omega_0 - Uk}, \quad (4.32)$$

one obtains an expression relating the Reynolds stress divergence and the change of wave action in time

$$\frac{k}{\rho_0} \frac{\partial \mathcal{A}}{\partial t} = -\frac{\partial}{\partial z} \langle u'w' \rangle_x. \quad (4.33)$$

Including the effects of viscosity [Grimshaw \(1974\)](#) finds the following WKB approximated evolution equation for the mean flow in 2D as a function of wave action  $\mathcal{A}$  (ie. as a function of wave amplitude)

$$\frac{\partial U(z, t)}{\partial t} = \frac{k}{\rho_0} \frac{\partial}{\partial t} \mathcal{A}(z, t) + \frac{k}{\rho_0} (\nu + \kappa)(k^2 + m(z, t)^2) \mathcal{A}(z, t). \quad (4.34)$$

Subject to the simplifying assumptions of the WKB theory one may find from equation (4.30) the more general concept of the conservation of wave action ([Bretherton, 1966](#)) in the absence of dissipation. Relaxing some of the simplifying assumptions this has been shown more generally by [Andrews and McIntyre \(1978\)](#).

Equation (4.34), (1.19) with (1.13) and (4.32) relate the background flow  $U(z, t)$  to the intrinsic wave properties  $m(z, t)$  and  $\mathcal{A}(z, t)$ . Together with initial and boundary conditions these form a WKB approximated non-linear system of coupled partial differential equations ([Grimshaw, 1975](#); [Baines, 1995](#)). While some of the underlying WKB scaling assumptions are violated in the simulations of the laboratory experiment (see the Richardson number analysis in the next section), some aspects of the flow appear well described by equation (4.34). In particular, the cumulative effect of viscosity (second term in equation (4.34))

and the instantaneous effect of propagating waves on the mean flow (first term in equation (4.34) are qualitatively captured. However, one cannot simply use scaling arguments and apply only one of the above equations but rather has to solve the coupled non-linear problem simultaneously. Only in the linear regime with weak or steady mean flow a strict separability between the mean flow and the waves is applicable. The precise limits of applicability of the WKB approximation are not known but the numerical results suggest that it is inappropriate to apply the WKB theory for the whole development of the arising flow, since ultimately the oscillatory behaviour is a solution of the non-linear equations in (1.2) and the effect of the boundary conditions. This is demonstrated in section 4.6.

As suggested in previous sections, instead of pursuing a semi-analytic solution using WKB theory or solving numerically (1.8),(4.20) and (4.24)<sup>5</sup>, the direct numerical simulation of the equations in (1.2) is employed for the special case of the Plumb and McEwan laboratory experiment. The simplicity of the experiment enables the investigation of a range of numerical and parametric sensitivities, important for the successful simulation of a QBO. From the results of section 4.2 the importance of wave interference in accord with a self-induced time-varying mean flow is confirmed. The existence of a single horizontal wave-number at any one time is found with a small range of vertical wave-numbers confirming the principal validity of equation (4.29). In accordance with these results, as visualised in Figure 4.24, Galmiche et al. (2000) notices that the wave-wave-mean flow interaction is spatially resonant but not in general temporally since the induced zonal mean-flow oscillation does not itself automatically verify the dispersion relation. Furthermore, the previously discussed importance of an anisotropy in the wave field, needed initially to give rise to a horizontal mean flow, has also been noted by Galmiche et al. (2000). Furthermore, equation (4.34) qualitatively expresses the contribution of explicit viscosity and diffusivity in enhancing the wave momentum transfer to the mean flow. In summary, the experimental results agree with above theoretical considerations to the extent that the equations (4.20),(4.29), and (4.34) qualitatively correctly describe aspects of the observed behaviour for the investigated flow until the formation of a critical layer. A further evolution does not directly follow from the above without further assumptions and the results of the direct numerical simulation are required at this point to derive the schematic description in the next section.

## 4.6 A revised schematic description of the QBO analogue

The original explanation of the laboratory analogue of the QBO given in Plumb (1977) and Plumb and McEwan (1978) has been revised, based on the results presented in section 4.2 and section 4.4 and the theoretical considerations in section 4.5. The precise mechanism of the mean flow reversal is documented by the figures 4.14, 4.16 - 4.24 and sketched in

---

<sup>5</sup>One could perhaps solve numerically the equations (1.8) and (4.20) with (4.24) by iteration for the complex structure functions of both waves and the mean flow  $U$  to obtain a semi-analytic result.

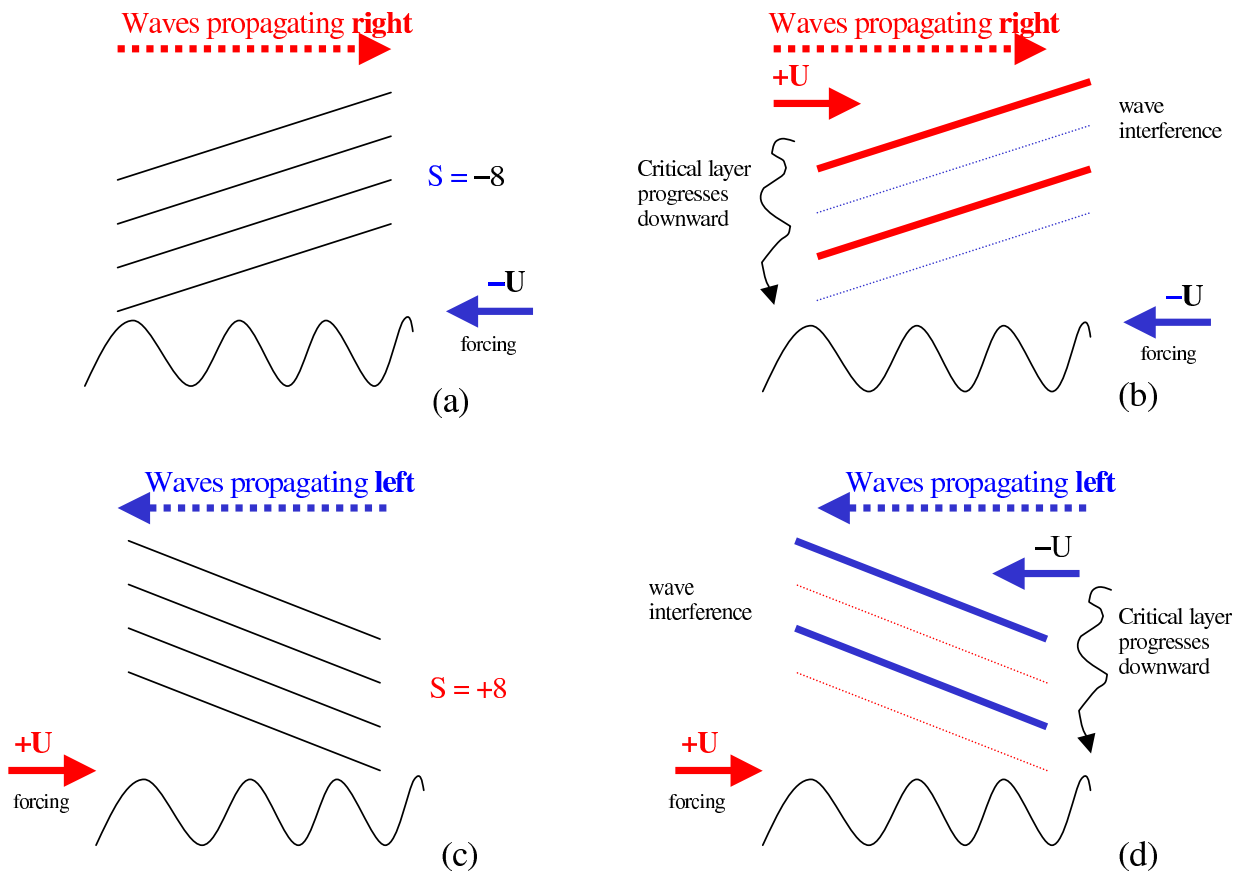


Figure 4.15: The principle mechanism of the oscillation in the laboratory experiment of Plumb and McEwan is shown in four representative phases of the mean flow. a) There is a zonal mean zonal flow  $-U$  creating gravity waves with a single dominant horizontal wave-number  $s = -8$ ; b) wave-wave-mean flow interaction generates a “critical layer” that propagates downward generating a zonal mean zonal flow  $+U$  near the oscillating membrane; c) The mean flow drives against the oscillating membrane from the opposite direction to create waves with horizontal wave-number  $s = +8$ ; d) wave-wave-mean flow interaction generates a “critical layer” for the opposite travelling waves generating a downward propagating zonal mean zonal flow  $-U$  near the membrane.

figure 4.15.

In the beginning there is no mean flow and two gravity waves with horizontal wave-number 8 and -8 (equivalent to 8 individual gravity wave sources) are excited symmetrically by the oscillating membrane (figure 4.17). The standing wave pattern eventually breaks down as a result of small disturbances (anisotropy) in the wave-field and subsequently a mean flow develops in some direction  $U$  (which direction, is reminiscent of the prediction of the apparent outflow direction of a bath tub wrongly attributed to the Coriolis force). If there was no anisotropy no mean flow would develop. In the numerical simulation (as pointed out before) a small excitation is required; in Nature the meta stable state is likely to breakdown through other unrelated disturbances. Once a mean flow has developed the

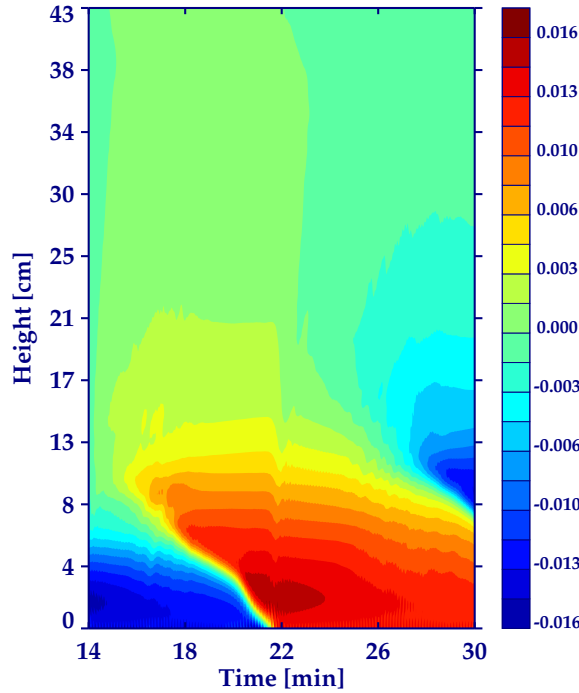


Figure 4.16: Time-height cross-section of the zonal-mean flow velocity for the in detail described phase of the mean flow reversal in section 4.6.

simulation proceeds as described below. It will be seen from that description, that the mechanism can be equivalently shown with an initial zonal background flow in the lowest layers. Therefore and because the very initial reversals are of small but growing amplitude the mechanism is shown in a more developed phase of the QBO analogue starting at  $t = 15$  minutes (plate a in the figures 4.18-4.23). The negative mean flow  $-U$  drives against the oscillating membrane like a mountain wave forcing creating gravity waves with a single dominant horizontal wave-number  $s = -8$ . The phase speed is positive and the waves propagate to the right (plate b in the figures 4.18-4.23). Due to the oscillation of the membrane and the constant (positive) wind forcing, time and spatially shifted vertically propagating waves with different vertical and the same horizontal wave number interfere predominantly in space. The spatial wave interference breaks up the coherent wave trains and, as explained in section 4.5, wave-transported momentum is transferred to the mean flow according to equation (4.20). A shear layer with positive mean wind  $+U$  is forming at the lowest level of wave interference. The Reynolds stress divergence is negative, consistent with equation (4.20). This is illustrated in plate c - e of the figures 4.18-4.23. The mean flow travelling in the same direction as the waves grows to a magnitude  $U_{crit} = \omega_0/k = 0.43/(2\pi 8/L_x) \approx 13 \text{ mm s}^{-1}$  which represents asymptotically a critical level to the (also vertically propagating) waves. At and below this level effectively all momentum carried by the  $s = -8$  wave is absorbed and the further vertical propagation of the wave is inhibited (plate e in figure 4.23). Note, that wave momentum fluxes are already enhanced before the layer actually becomes critical and as is evident in the 3D simulations the mean may never

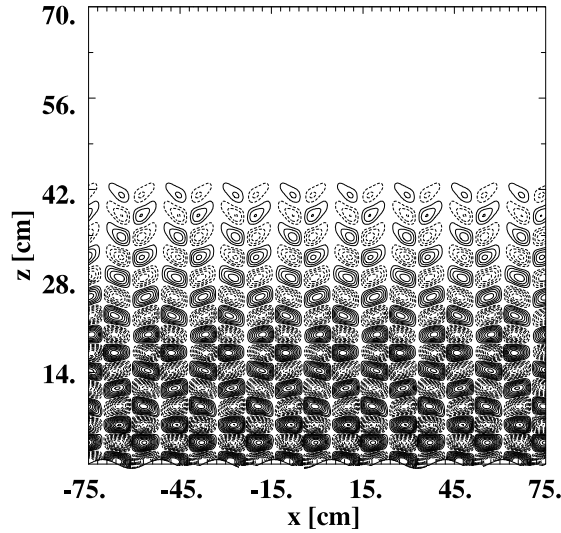


Figure 4.17: Symmetric gravity waves are excited by the oscillating membrane in the beginning of the simulation with no background flow.

reach a critical magnitude. However, locally the waves nevertheless experience “critical behaviour” in the same way, thus defining a “critical layer” below a virtual critical level. This is further discussed in section 4.7. With the subsequent enhanced convergence of the wave-induced stress below the critical layer through wave breaking (i.e., examine the local Richardson number  $Ri \equiv N^2/(\partial u/\partial z)^2 < 0$  in the critical layer in figure 4.19, also some regions exhibit  $Ri \sim \mathcal{O}(1)$  and everywhere else  $Ri \gg 1$ .) the shear layer grows downward. Interestingly, at least in the 2D simulations, the apparent downward growth only starts once the magnitude of the zonal flow at the shear layer equals or exceeds  $U_{crit}$ . Explicit viscosity (and to some extent the chosen vertical and horizontal resolution of the numerical model if poorly resolved) appears to act in support of the growth, further restricting the vertical wave propagation (plate e - h in figure 4.18-4.23). When the shear layer with  $+U$  arrives at the forcing level (the membrane), it drives against the oscillating membrane but from the opposite direction to create waves with horizontal wave-number  $s = +8$ , propagating to the left. The wave interference, critical layer formation and apparent downward propagation of the zonal mean flow proceed as before but with opposite sign. It is therefore, that the oscillation in the laboratory analogue appears to propel itself through the subsequent arrival of a reversed mean wind at the forcing level and not through “viscous” destruction of a mean shear layer as proposed by Plumb (1977). Qualitatively it may be argued that the mechanism described above is equivalent to the interpretation, where always both horizontal waves  $s = +8$  and  $s = -8$  are present, but where one wave is filtered out immediately through absorption at or just above the forcing level.

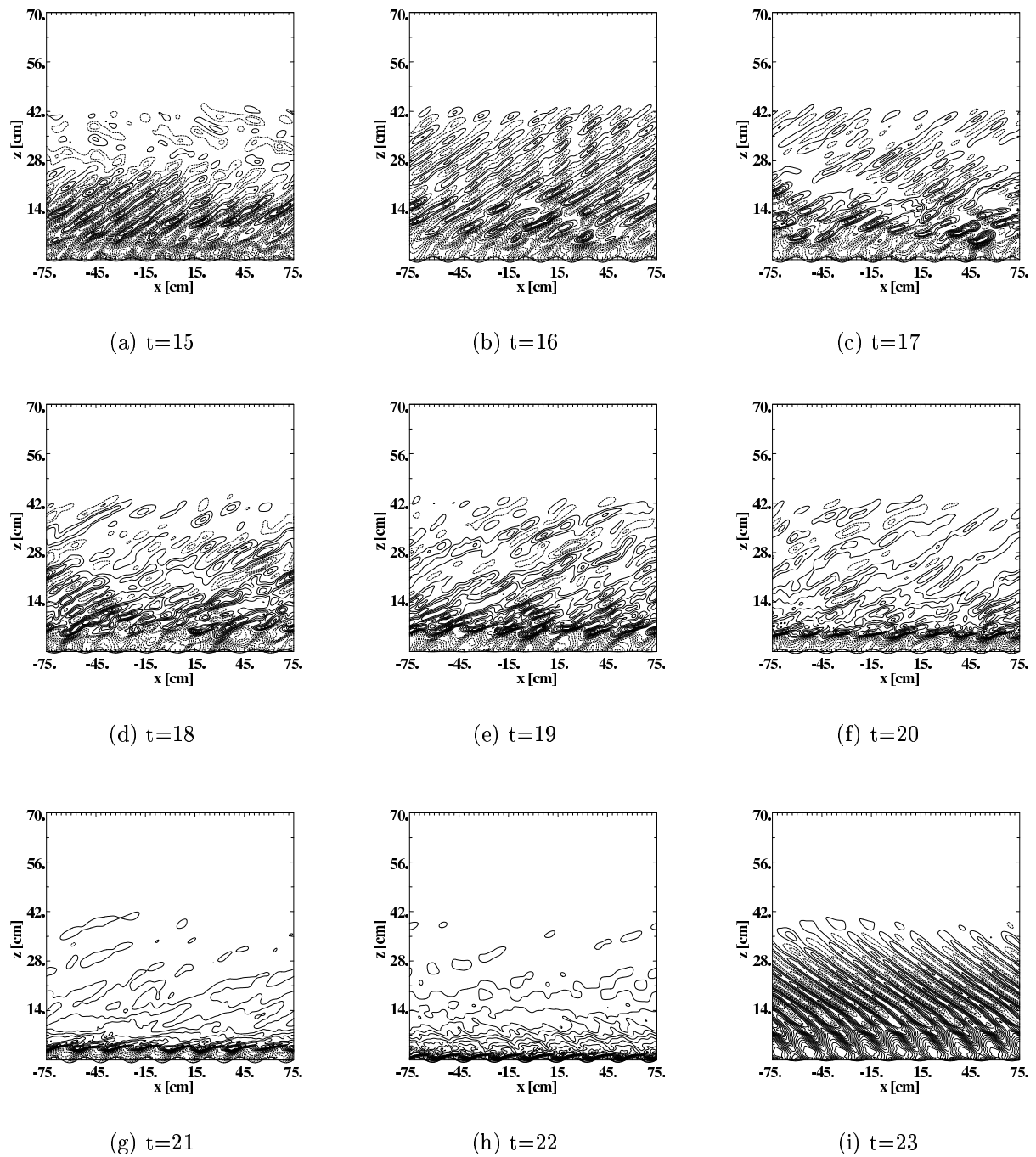


Figure 4.18: Time evolution between  $t=15\text{min}$  to  $t=23\text{min}$ . The figure shows the evolution of the zonal wind during one half period of the reversing mean flow.

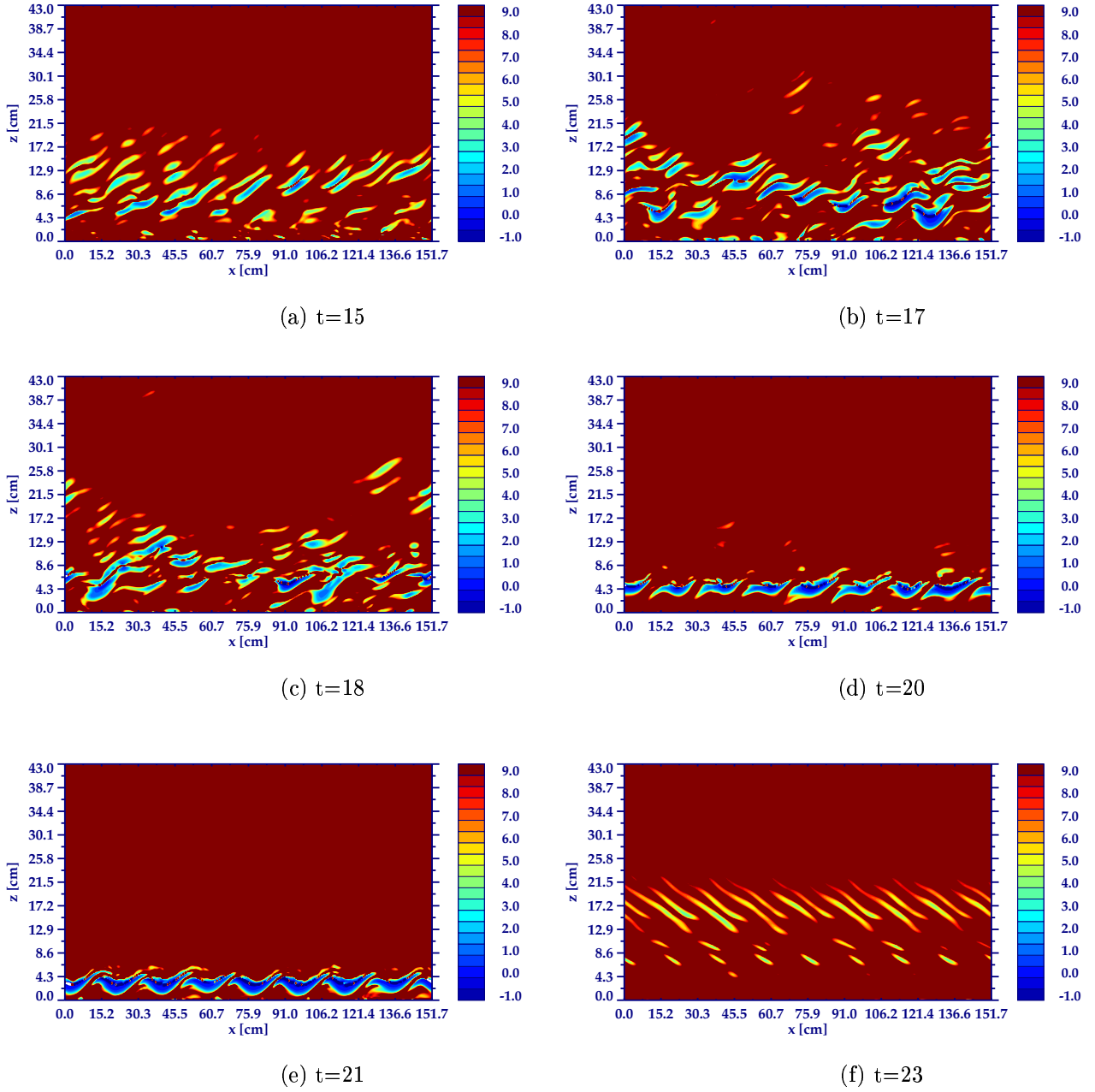


Figure 4.19: Time evolution between  $t=15$ min to  $t=23$ min. The figure shows the dimensionless local Richardson number  $Ri = -(g/\rho)(\partial\rho/\partial z)/(\partial u/\partial z)^2$  and occurrences, where  $Ri < 0$  (convective instability and wave breaking regions), during one half period of the reversing mean flow. Richardson numbers greater than 9 (where one may assume the validity of  $Ri \gg 1$ ) and lower than  $-1$  are plotted in the maximum or minimum colour, respectively.



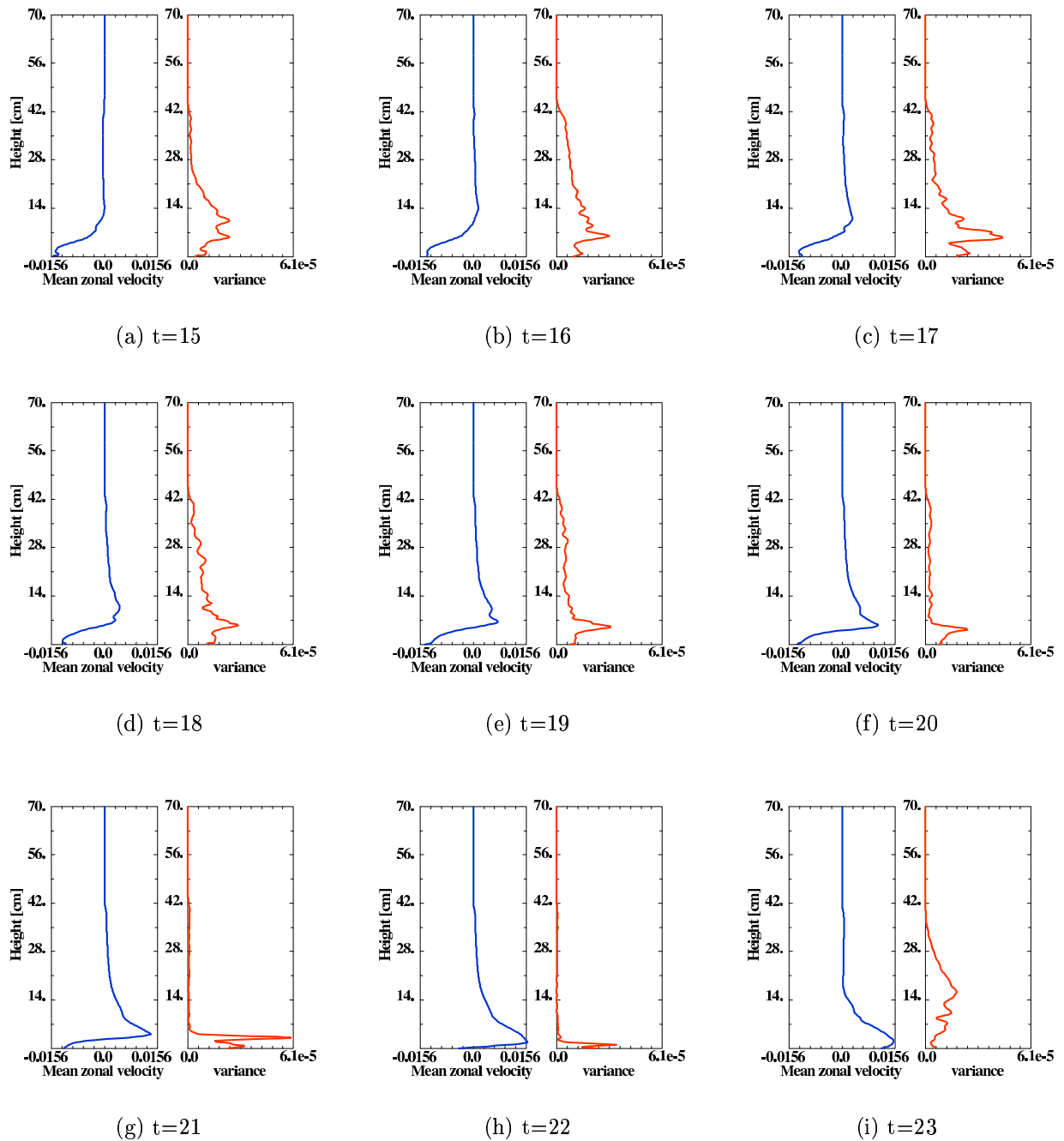


Figure 4.20: Time evolution between  $t=15\text{min}$  to  $t=23\text{min}$ . The composite figure shows the evolution of the zonal mean zonal velocity profile during one half period of the reversing mean flow. The left plate in each figure shows the zonal mean and the right plate the variance. Units are in  $m s^{-1}$  and  $m^2 s^{-2}$ , respectively.

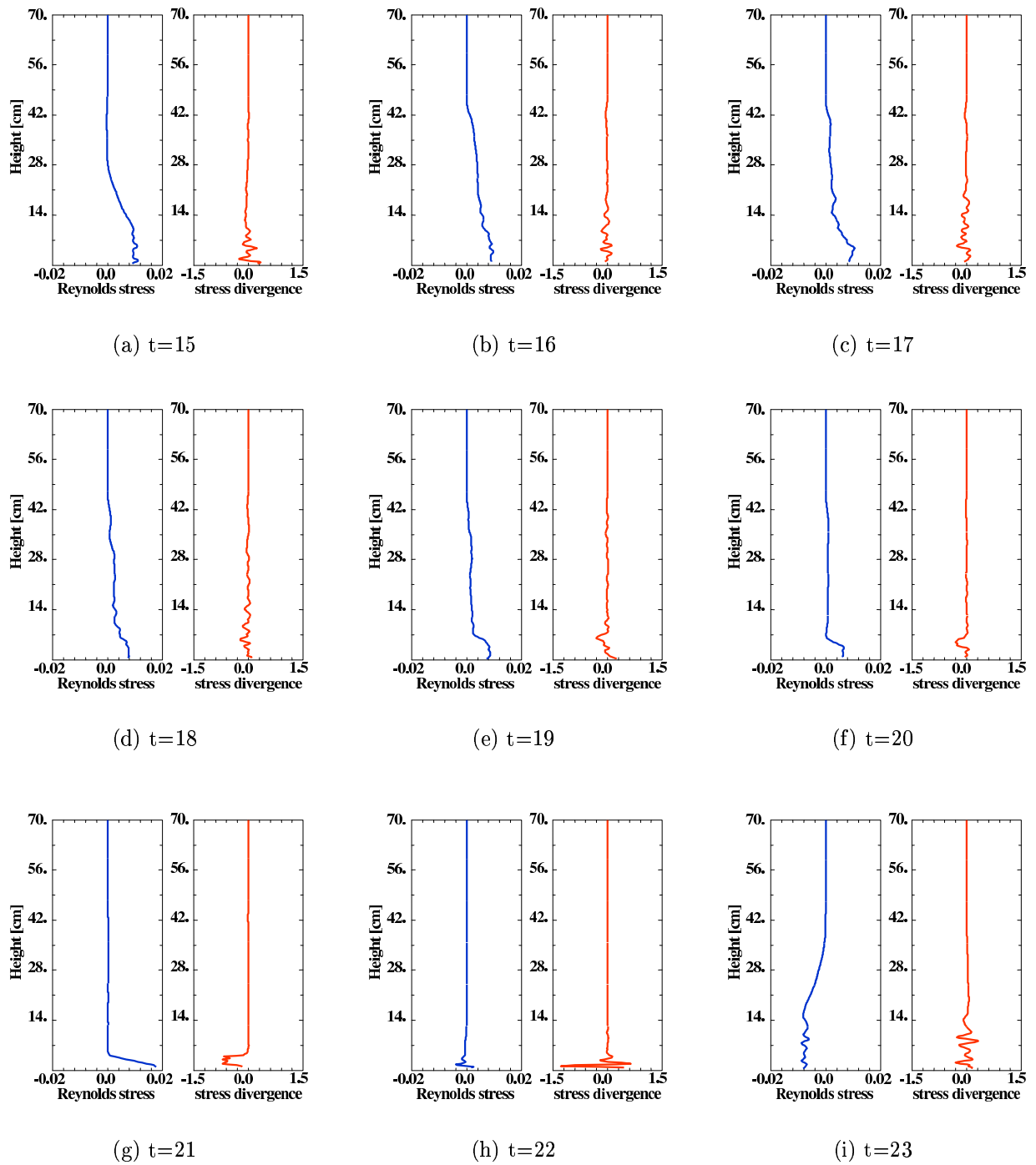


Figure 4.21: Time evolution between  $t=15\text{min}$  to  $t=23\text{min}$ . The composite figure shows the evolution of the Reynolds stress (left plates) and the Reynolds stress divergence (right plates) during one half period of the reversing mean flow. Units are in  $Nm^{-2}$  and  $Nm^{-3}$ , respectively.

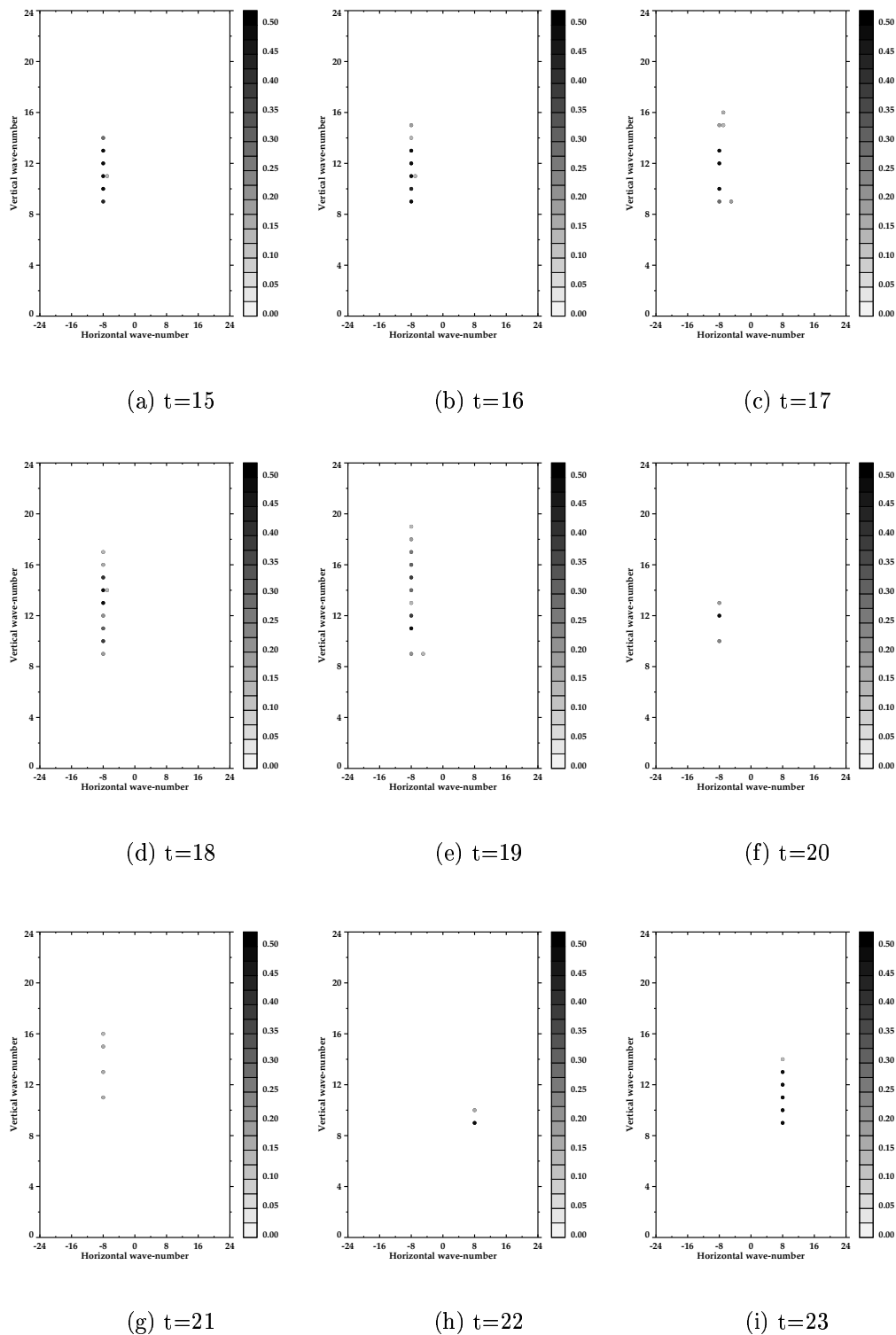


Figure 4.22: Time evolution between  $t=15$ min to  $t=23$ min. The figure shows the evolution of the horizontal and vertical wave number analysis of the zonal wind data during one half period of the reversing mean flow.

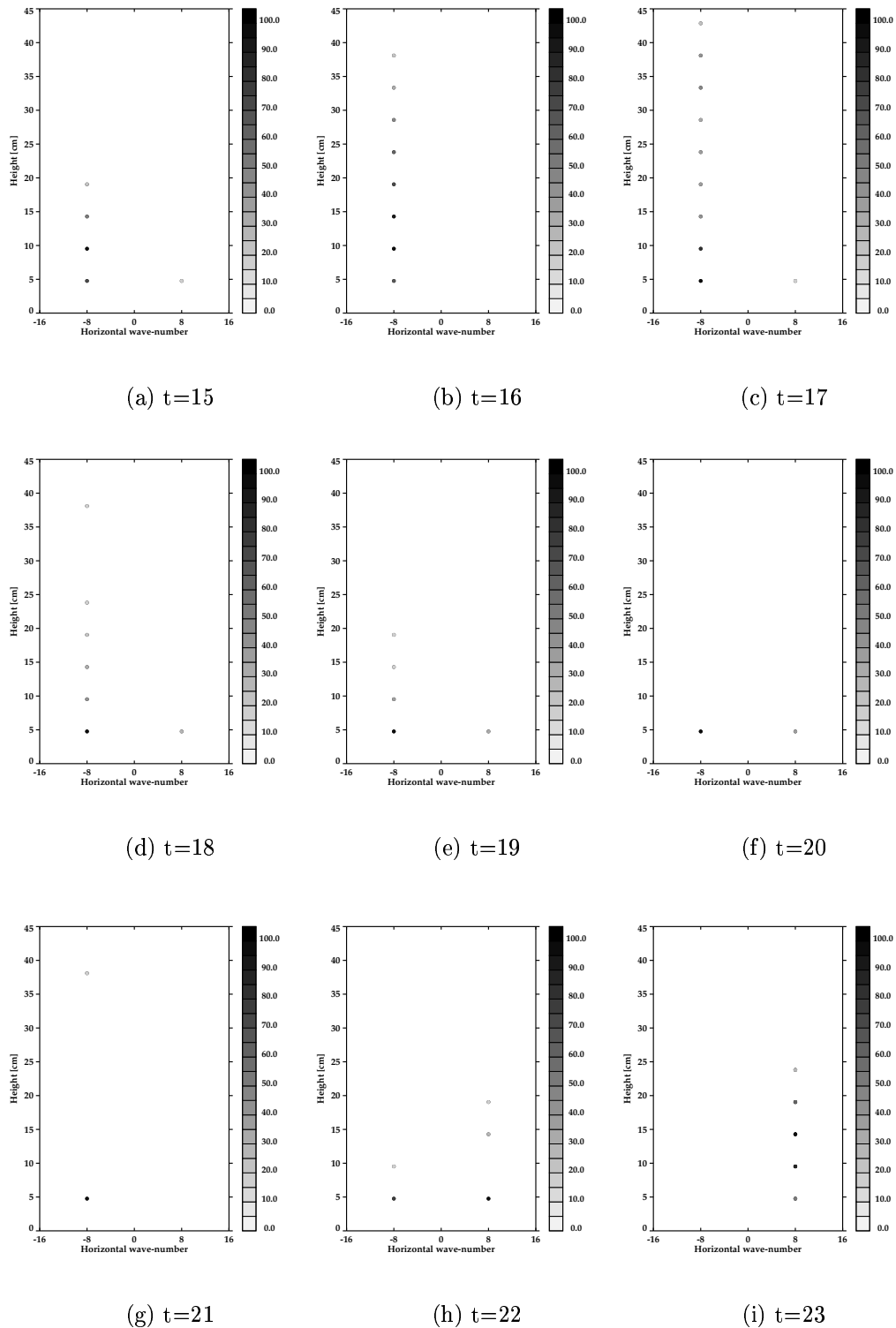


Figure 4.23: Time evolution between  $t=15$ min to  $t=23$ min. The figure shows the existence of horizontal wave numbers in 9 equidistant vertical levels during one half period of the reversing mean flow. The strength of the colour indicates the power. Only vertical levels with a power larger than 10 percent of the dominant power in an interval are plotted.

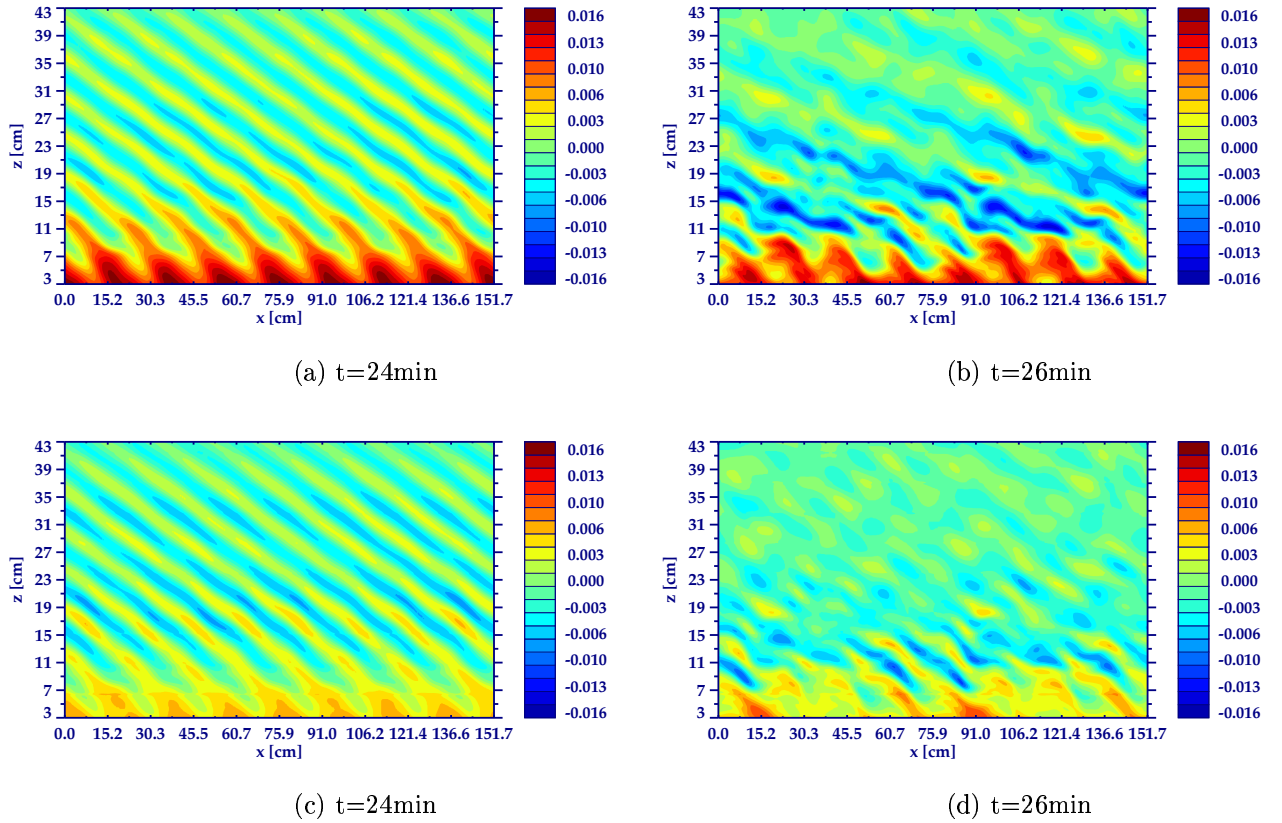


Figure 4.24: The observed horizontal velocity data in plate a and b is shown at time  $t=24\text{min}$  and  $t=26\text{min}$  in comparison to the signal reconstructed from the dominant wave spectrum in the corresponding time-interval (plate c and d) and as identified spectrally from figure 4.22. In this case all vertical wave-numbers except for the range  $m = 8 - 16$  have been filtered out to create plate c and d. A crude highpass filter has been applied by setting all coefficients to zero below  $m = 8$ , and has been combined with a lowpass filter of the form  $1/(1 + (m/M_{cut})^l)$  with  $l = 36$ ,  $M_{cut} = 16$ .

## 4.7 Summary

In this section the main results of the direct numerical simulation (DNS) of the QBO analogue are summarised.

The different experimental setups and the range of resulting zonal mean zonal flow oscillations, as described in [Plumb and McEwan \(1978\)](#) and [Otobe et al. \(1998\)](#), have been successfully reproduced. However, the experimentally observed zonal mean flow oscillation period, obtained with lower forcing frequency and larger amplitude (Fig. 11 in [Plumb and McEwan \(1978\)](#)), has not been exactly reproduced by the numerical simulations, which tend to predict shorter periods. Differences between the relatively wide

range of oscillation periods in the laboratory (Otoabe et al., 1998) compared to the DNS are explained primarily due to the strong sensitivity of the oscillation period to the forcing wave-number of more than  $\propto k^3$  and its realization in the laboratory experiments. Other individually investigated parametric sensitivities play a role but are less significant in comparison.

In the parameter range investigated by Plumb and McEwan (1978) the relationship to the zonal mean oscillation period can be confirmed, namely  $\propto 1/N$ ,  $\propto 1/\epsilon$ ,  $\propto 1/(\nu + \kappa)$ ,  $\propto \omega_0$  and approximately  $\propto k^3$ . However, a number of examples are given where these simple proportionality laws don't hold. The reason is given through the inherent nonlinearity of the involved processes. Inviscid scenarios do not maintain a mean flow oscillation but develop vertically staggered zonal mean flow layers of opposite sign. It is found that viscosity acts primarily as an "agent", contributing to the wave momentum flux convergence in regions of strong nonlinearity. Replacing the effect of viscosity and salt diffusivity by a (physically unmotivated) friction term in the thermodynamic equation results in a zonal mean flow oscillation in the inviscid case. Too strong viscosity suppresses an oscillation. The other sensitivity to the medium in which the waves propagate is given by the stratification. It is found that continuously changing stratification alters the period of the zonal mean flow oscillation and sharp changes in stratification give rise to wave reflection, altering the vertical extent and the period of the oscillation. Finally, the shape and amplitude of the forcing has been investigated in detail. As has been found by Plumb and McEwan (1978), sufficient amplitude is necessary to obtain a zonal mean flow oscillation. Combinations of various wave-numbers and frequencies show a dominant role of the combination with the largest critical velocity that can be reached. Multiple combinations with the same critical velocity accelerate the downward propagation. A "semi-random" forcing with varying shapes and amplitudes of individual cosine mountains also results in a zonal mean zonal flow oscillation. If waves exist but a critical velocity is not reached (not even locally), zonal mean zonal flow variations are observed but no mean oscillation.

Simulations with a linearised version of the equations do not show a zonal mean oscillation. However, the non-linear set of the Boussinesq approximated equations (1.2) has been found adequate for the DNS of the laboratory experiment. Aspects of numerical realisability have been investigated where the onset of the zonal mean flow oscillation and the length of its period are used as a measure of numerical error. Sensitivities are found to the resolution, to the advection scheme, to the use of first-order and second-order accuracy or an alternating use, to the accuracy of the pressure solver, to explicit versus implicit formulations and to the sensitivity of upper and lower boundary conditions. All of these can be summarised as influencing the numerical solution of wave dispersion, their dissipation and subsequent alterations of the mean flow. In the flux-form Eulerian formulation, numerical dissipation has been found to be unimportant for the onset or the evolution of the oscillation. However, in the semi-Lagrangian framework it may account for the distorted evolution and the unrepresentative growth of potential and kinetic energy. In three dimensions boundary conditions (other than the oscillating membrane) had negligible influence due the viscosity of the water and due to the amplitude decay of three-dimensional gravity waves, unlike two-dimensional hydrostatic flow (Smith, 1980). However, 2D simulations

required careful consideration of the boundary opposite the oscillating membrane due to wave reflection substantially influencing the zonal mean zonal flow oscillation period. In non-Boussinesq simulations the amplitude growth of vertically propagating waves, due to the decrease of density with height, offsets the decay and may raise again the importance of upper boundary influences in atmospheric simulations.

It is found that some anisotropy has to exist to excite a zonal mean flow oscillation. Then the laboratory experiment exhibits critical layers which determine the behaviour of the mean flow. The arising zonal mean flow speed matches in all 2D cases and approximately in some 3D cases the critical velocity given by relation (4.3) and as predicted from linear theory. However, while locally a critical magnitude of the flow is reached in most 3D experiments, the zonal mean zonal flow is found to be  $2 - 3 \text{ mms}^{-1}$  below the theoretical critical threshold. In experiments with low frequency and large amplitude and especially with an imperfect membrane the observed mean deviates substantially, up to  $5 - 6 \text{ mms}^{-1}$  from critical magnitude. However, the reversing mechanism is still the same in all simulations. One observes regions of wave overturning and breaking (with  $Ri < 0.25$  or  $Ri < 0$ ), where the background flow locally accelerates (critically) and these regions of acceleration merge (horizontally) to a more confined layer, even when the mean is not observed to be critical. The height at which this layer is first identified depends on the stratification, forcing shape, amplitude and frequency. It appears therefore that horizontal averaging leads in 3D to a non-critical mean flow. This is in particular obvious with imperfect membranes, where in some part of the tank the flow is even reversed to the mean but by simply evaluating the mean an overall unidirectional picture emerges. A critical background flow may therefore be seen as an idealisation of reality, in particular when a number of (imperfect) wave sources exist.

The detailed analysis of the obtained data (spectral analysis, energy budgets, vertical profiles of Reynolds stress divergence and zonal mean zonal velocity, and x-z-plots of Richardson number and the zonal velocity component) suggest a different picture of the arising oscillation compared to the original explanation by [Plumb and McEwan \(1978\)](#). In the DNS the zonal mean zonal flow oscillations are wave-driven by wave-induced vertical transport of momentum originating from the oscillating boundaries and dissipated at self-induced mean flow variations that grow to “self-destructing” critical magnitude, given sufficient forcing amplitude. When this critical magnitude is reached, one observes the downward propagation propelled by wave breaking (indicated by visual inspection and Richardson numbers lower than zero). The simulations exhibit a number of fundamental internal wave phenomena: wave interference, wave reflection, wave-mean flow interaction, critical layer gravity wave attenuation and subsequent wave breaking. While the same mechanistic behaviour is observed in 2D and 3D simulations, the amplitudes and oscillation periods differ due to the amplitude decay of three-dimensional gravity waves in a dissipative Boussinesq medium.

The theoretical considerations in section 4.5 link the explanations given by [Plumb \(1977\)](#) and [Galmiche et al. \(2000\)](#) to each other and to the results obtained from the DNS in explaining aspects of the laboratory experiment. However, it is concluded that ultimately only the DNS results give the correct and complete picture, which is detailed

in section 4.6 and sketched in figure 4.15.



# Chapter 5

## Discussion

### 5.1 The generalised time-dependent coordinate transformation

The generalisation of the Gal-Chen & Somerville development allows to include intricate time-dependent boundaries into numerical models via a coordinate transformation of the bounding surface. In principle, an auxiliary boundary model could have provided the velocity components and potential temperature along a flat boundary, accounting for the changing momentum fluxes across the boundary as the simulation progresses. However, since the shape of the upper boundary is fixed independently of the fluid flow, this approach requires the numerically accurate estimation of all dependent variables at the bounding surface. In particular, the specification of advective velocities is more difficult in this case.

In the context of ocean data assimilation and subsequent adjoint operations in the presence of a free surface the application of the coordinate transformation may provide a natural utility to overcome the difficulty that the control variable (free surface height) is also a prognostic unknown of the forward model (Gejadze and Copeland, 2004).

In the context of atmospheric applications, where hybrid vertical coordinates are commonly used, the approach may provide an alternative to the vertical nesting of different curvilinear frameworks within the same model. If several vertically bounding surfaces exist, the coordinate transformation may be further generalised to

$$\xi = \sum_{i=1}^N \xi_{0i} \frac{z - h_{i-1}}{h_i - h_{i-1}}, \quad (5.1)$$

with  $h_0 = z_s$  and  $\xi_{0i} = H_{0i}$  for  $h_{i-1} \leq z \leq h_i$  and 0 otherwise. While this formulation has not been further explored in this thesis, it may complement attempts to exploit the strength of different curvilinear frameworks for various regions of a simulated medium, each coupled through a common interface layer. In particular in geophysical flows, it may facilitate the coupling of boundary layers with stratified fluids, such as the incorporation of mixed layers in deep oceans and the coupling of planetary boundary layers (PBL) to the large-scale dynamic flow.

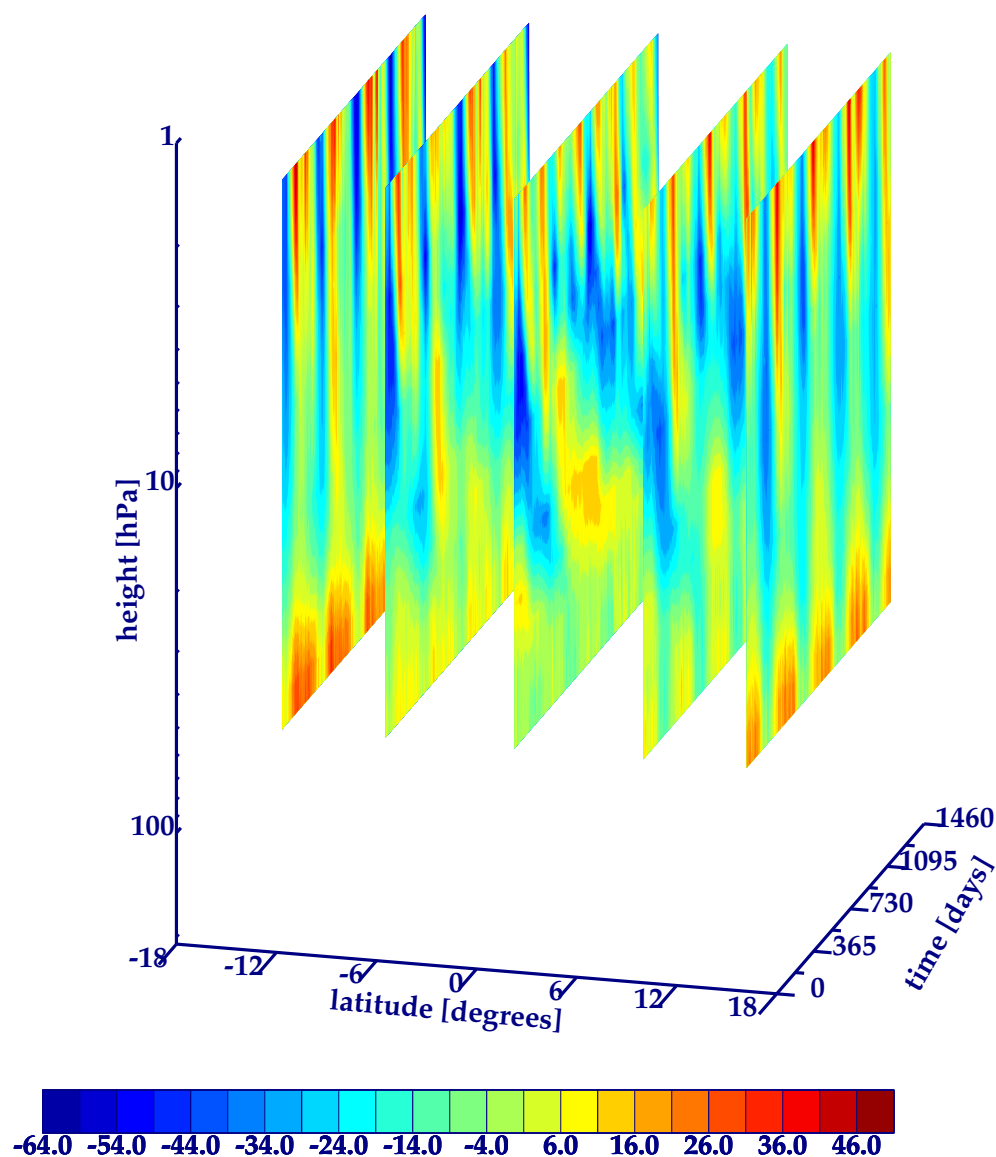


Figure 5.1: The quasi-biennial oscillation as analysed in ERA40 in a three dimensional time-height representation. The figure shows time-height slices of zonal mean zonal wind between 200hPa and 1hPa averaged between  $\pm(18 - 16)$  degrees latitude, between  $\pm(10 - 8)$  degrees, and at the equator,  $(0 - 2)$  degrees, for the period 1965-1968.

## 5.2 Implications for atmospheric equatorial zonal mean flow oscillations

In this chapter, the results of the direct numerical simulation of the QBO analogue, as summarised in section 4.7, are discussed in the context of the atmospheric QBO, the basic mechanism of which it was designed to emulate.

Figure 1.1 illustrates the evolution of the QBO in the equatorial stratosphere for the pe-

riod 1965-1990, as analysed by the European Re-Analysis project (ERA40) (Uppala et al., 2004), which incorporated all available observations over a period of 40 years, utilising the latest available three dimensional variational data assimilation system. A typical latitudinal perspective for the period 1965-1968 is shown in figure 5.1. Apparent downward propagating mean flow patterns with maximum amplitudes nearer the equator can be seen. Towards the top of the time-height slices another zonal mean flow oscillation with shorter period, the semi-annual oscillation (SAO) can be observed, which makes it difficult to measure the actual vertical extend of the QBO.

The following questions have been posed in the introduction and are now addressed using the results of the direct numerical simulation of the laboratory analogue of the QBO.

- Where is and what determines the upper and lower boundaries of the QBO in the real atmosphere?
- What is the precise mechanism that dissipates one phase of the QBO near the tropopause and when does the next phase start aloft?
- Which waves drive the QBO in the real atmosphere and how are they generated?
- What is required in global circulation models to reproduce a wave-driven zonal mean zonal flow oscillation?

The design of the laboratory experiment of Plumb and McEwan (1978) was such as to verify the theory outlined by Holton and Lindzen (1972), in which the upward propagating waves are attenuated primarily by infrared cooling. It is an interesting twist to the story about the QBO that the results of the direct numerical simulation for the same laboratory setup favour instead the theory put forward by Lindzen and Holton (1968) and advocated by Dunkerton (1981); Horinouchi and Yoden (1998) and others: the critical layer attenuation of gravity waves. Since the laboratory experiment is often employed to explain the basic mechanism of the atmospheric QBO (Baldwin et al., 2001), this thesis provides a revised detailed description of the precise mechanism, including a careful analysis of the data in various phases of the mean flow reversal.

In comparison to the laboratory mean flow oscillation, several details can be noted for the atmospheric QBO. First, numerical evidence is provided that the periodically reversing mean flow pattern in the laboratory analogue is a wave-wave mean flow interaction driven phenomenon with a non-zero momentum flux divergence primarily resulting from vertical wave interference, then subsequent critical layer formation and internal wave dissipation within, enhanced by wave breaking. A spectral analysis of the numerical data and energy considerations underline the conclusions and reveal a different oscillation mechanism from that described in Plumb (1977). In the laboratory experiment the mean flow arriving at the forcing level actively induces the next phase of the oscillation. In the atmosphere it appears from the ERA40 data (though not conclusively) that like in the laboratory analogue the next phase of the QBO only starts once the previous phase has arrived near the tropopause. Incidentally, Gabis and Troshichev (2005) find the existence of westerly

wind regimes, throughout the entire height range of a 50 year data set only in 3 % of the months, which coincides approximately with 21 observed reversals from westerly to easterly. This is similar to the behaviour in the laboratory experiment.

In the numerical simulations, almost complete wave absorption is observed before the mean wind magnitude is critical but downward propagation only starts and is maintained when “criticality” is reached. A positive mean wind supports the vertical propagation of waves necessary for the formation of a negative mean wind aloft. A negative mean wind of critical magnitude would not allow their vertical propagation and would filter these waves by absorbing them. The following two dynamical mechanisms are possible in the atmosphere. In the first scenario the mean wind arriving near or just above the tropopause (the assumed forcing level) would actively induce gravity waves with a reversed horizontal propagation direction such that by itself it provides the necessary forcing for the next phase of the QBO. One possible wave generating mechanism at the tropopause height is described in laboratory experiments of [Flynn and Sutherland \(2004\)](#), who investigated the excitation of internal gravity waves by fluid intrusions propagating along the interface between two differently stratified layers. They concluded that as a result gravity waves could be generated whose momentum flux is comparable to the momentum flux generated by topographically excited waves. The zonal mean wind of a QBO phase arriving at its forcing level may trigger the excitation of waves in such manner. In the second scenario the atmosphere always supports both horizontal propagation directions of waves and the mean wind filters the waves accordingly but plays no role in the wave generation. The second scenario is more difficult to realize in the numerical setup described in this thesis. One would have to prevent the mean flow from descending down to the membrane. So far both possibilities appear equally likely and may both contribute.

Stratification changes appear to confine the vertical propagation of gravity waves, as has been found in this thesis and by other authors ([Koop, 1981](#); [Baines, 1995](#)). It is speculated that the propagation of gravity waves contributing to the QBO may therefore be naturally confined between the tropopause and the stratopause and therefore effectively defining the vertical extent of the QBO and somewhat predetermining the length of its period. Unfortunately, the semi-annual oscillation (SAO) overlaps with the QBO and the lack of sufficient observations does not allow at present to verify this conjecture. Current numerical models as well as reanalysis data sets have the top of their model domain near the stratopause with increasingly poor resolution towards the model top, which also does not allow further insight into the vertical structure of the equatorial oscillations at stratopause height.

The influence of stratification on the zonal mean zonal flow oscillation period (decreased Brunt-Väisälä frequency increases the period) may explain the observed apparent change of the downward propagation speed of the stratospheric mean flow near 10hPa when considering the stratification change of the U.S. standard atmosphere at that height ([Holton, 1992](#)), pp. 403).

The simplicity of the laboratory experiment facilitates a revealing spectral analysis of the zonal mean flow oscillation and the waves involved in each phase. The atmosphere is likely to support a number of waves with similar wave-number/frequency pairs whose phase

speeds are critical to the observed mean flow. In the sensitivity experiments described in subsection 4.2.1 it is shown that similar wave-number/frequency pairs all contribute and accelerate the mean flow oscillation through increased wave momentum fluxes. The authors in Horinouchi (2003) tried to identify wave-number/frequency pairs in a spectral analysis of several global models but concluded that the participating models do not sufficiently resolve the necessary waves. It is not known if ERA40 exhibits those waves, but it should be noted that due to the nature of the process (short period waves exciting a large scale oscillation) the correct analysis of the QBO mean wind does not imply a correct representation of the necessary (forcing) waves. Further research and better observations will be necessary to answer this question but the detailed analysis in chapter 4 may help to discard part of the observed spectrum of waves based on the relevance of the criticality of the mean flow (rather than radiative cooling), the dominance of westward (eastward) travelling waves in an eastward (westward) mean flow, and the relative insignificance of waves with critical levels below the observed zonal mean flow of the QBO.

However, while the waves in the laboratory experiment are described as two opposite travelling waves, in the atmosphere, a quasi-random superposition of a spectrum of waves is likely to exist. What is perceived as a coherent large scale planetary wave may be generated by a sequence of causally disjoint processes which are aligned spatially and temporarily in a specific manner, where the combined behaviour exhibits a wave like pattern. The simulation with randomly distributed, and somewhat arbitrarily shaped, oscillating mountains with a coherent phase shift between them, in resemblance of radiatively driven (day-time sun) convection that forces gravity waves aloft, also created a regular zonal mean flow oscillation. This numerical result indicates that the forcing of the atmospheric QBO may just be the result of a “semi-random” forcing of a spectrum of waves even in the absence of horizontally propagating planetary waves. The “aqua-planet” experiment by Horinouchi and Yoden (1998) supports this conclusion.

In the introduction it was mentioned that the ECMWF model successfully modelled a QBO like oscillation (Untch, 1998) in an earlier version of the model but that the result in recent years could not be reproduced despite resolution enhancements and considerable progress in forecast ability (Simmons and Hollingsworth, 2002). The results in this thesis together with earlier studies (Giorgetta et al., 2002) suggest the need for sufficient resolution but above all the importance of vertically propagating gravity waves in the stratosphere with sufficient amplitude (energy) to produce a mean flow of critical magnitude. The most effective way to create many internal waves in the ECMWF model is by switching off the convective parametrization (P.Bechtold, personal communication). Lacking diabatic convective forcing to compensate the adiabatic tendencies, the model produces strong (randomly-distributed) localised convergence (figure 5.3) at the grid-scale, which in return produce large amplitude, vertically propagating gravity waves. These waves suffice to produce a QBO like oscillation in a climate integration using the latest forecast model at ECMWF (figure 5.2 and 5.3). An apparently paradoxical explanation for the “loss” of a QBO-like oscillation in the ECMWF model in the past years may therefore be given as the result of recent improvements in the convection scheme aimed at avoiding numerically generated gridscale divergence. These changes eliminated a major source of

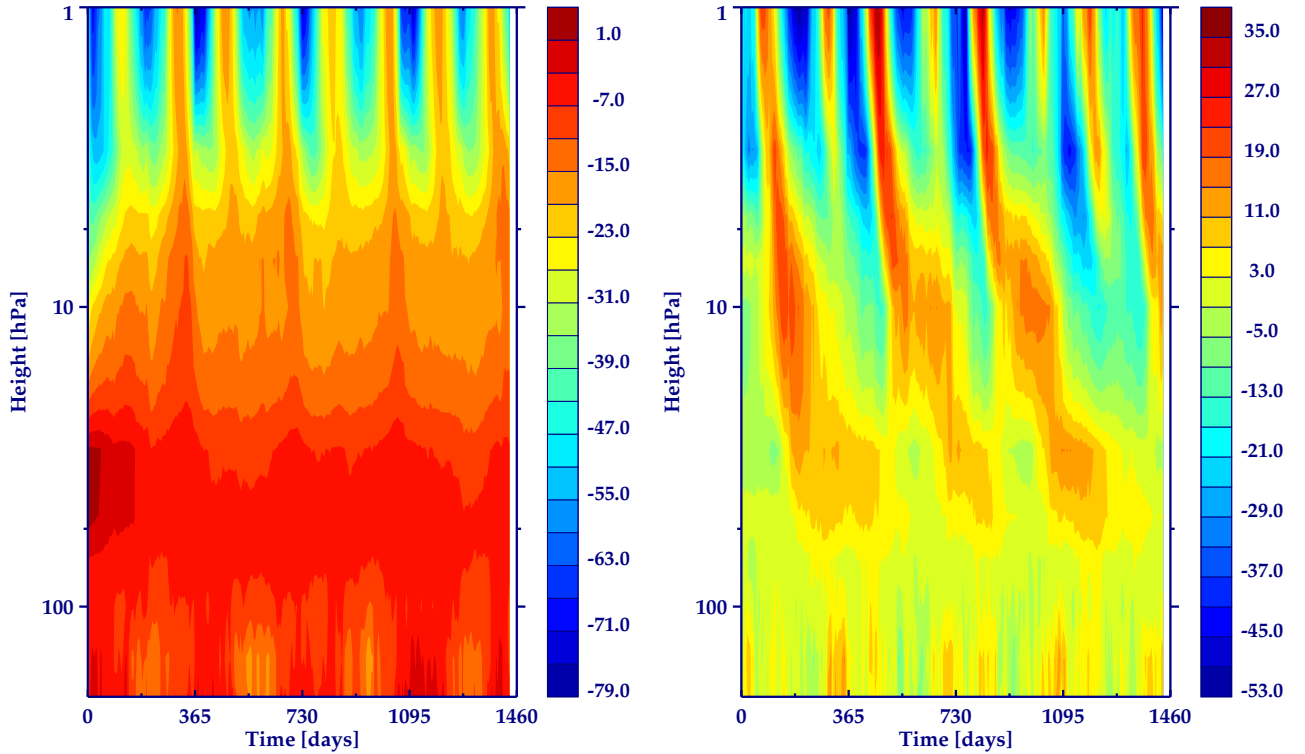


Figure 5.2: A QBO-like oscillation in a T63 IFS model simulation with 91 levels and no parametrized convection in the simulation. The left plate shows the time height cross-section at the equator for the experiment using the Tiedke convection scheme and the right plate shows the case with the convection scheme switched off.

gravity waves in the model. A comparison with the magnitude of gravity waves resulting from the operational convection scheme (Tiedke, 1989) shows indeed a large difference in the amount and the amplitudes of the generated waves. It furthermore suggests that the random distribution of such gravity wave sources suffices for the successful simulation as in (Horinouchi and Yoden, 1998) and as in the laboratory simulations described above. Also, since horizontal diffusion primarily acts on the tail of the spectrum of the resolved gravity waves in global atmospheric models (see section 1.5.4 for the effect of enhanced horizontal diffusion in the IFS model), the “tuning” of horizontal diffusion, which helped to obtain a QBO-like oscillation in Takahashi (1999), may be readily understood as varying the degree of suppression of gravity wave forcing.

The influence of the Coriolis force on mean flow oscillations has not been investigated in this study. A beta-plane approximation has been tested in the three-dimensional laboratory simulations but it had very little effect on the period. However, it is believed that the Coriolis force plays a major role in confining the oscillation to the equatorial latitudes (Haynes, 1998). This may also stem from the fact that the Reynolds stress divergence is

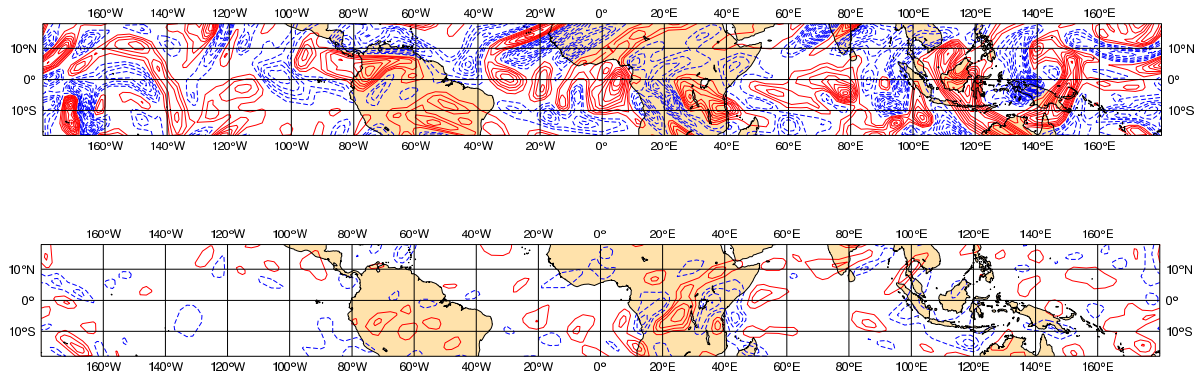


Figure 5.3: Instantaneous horizontal distribution of the driving forces for the QBO-like oscillation in the T63 IFS model with 91 levels. The simulation develops some strong local events throughout the troposphere reaching as high as model level 39 ( $\approx 100$  hPa), which is shown here. The figures show horizontal velocity divergence. Strong localised divergence patterns on the grid-scale can be identified that develop in the simulation without parametrized convection; the bottom plate exhibits the relative lack of such events when using the Tiedke massflux convection scheme. The contour interval is  $0.5 \text{ s}^{-1}$  in both plates.

balanced in part by the Coriolis term sufficiently away from the equator. It is speculated that this behaviour may be analog to the overwhelming effect of viscosity that has been shown in subsection 4.2.1 for increased values of  $\nu$  resulting in the disappearance of the oscillation. The influence of the Coriolis force on critical level behaviour has been investigated by Shutts (2001) concluding a vertical blurring effect as to where in space wave momentum flux convergences occur. Therefore, the absence of a particular critical layer, would possibly also prevent the development of a long-term oscillation such as the QBO. Variations in the meridional flow magnitude may further contribute to such dilution. However, it is well known that the mechanism of self-induced mean flow variations by orographic gravity waves with or without subsequent critical layer formation is relevant far away from the equator. For example, the effect of sub-grid scale mountain wave drag is typically parametrized in atmospheric models to simulate the drag effect on the larger scale simulations. The fundamental mechanism discussed in section 4.5 may also contribute to the discussions on severe downslope windstorms (Smith, 1985; Laprise and Peltier, 1989a,b). Furthermore, in investigations of transition to turbulence it may be relevant to consider wave mean flow interactions since it provides a contrasting mechanism to the energy extraction from the mean flow through baroclinic instabilities (see Holton (1992) for details). Direct numerical simulations (DNS) and large eddy simulations (LES) of turbulence in stratified homogeneous shear flows are summarised in Schumann (1996). There it is pointed out that large scale anisotropies due to the formation of locally turbulent spots need to be considered in turbulent studies of the free atmosphere. These spots may result from the onset of wave breaking at pre-existing critical levels. However, in this thesis it is shown that the prop-

agating gravity waves may themselves form such subsequently “self-destructing” layers. In this context [Poulin et al. \(2003\)](#) stressed the importance of time-varying background flows on the stability of otherwise stable shear flows. In this respect this thesis may be seen as a step towards more realistic investigations of atmospheric phenomena in stratified non-uniformly time-varying background flows.

### 5.3 Future work

The theoretical and numerical framework developed in this thesis allows further investigations into various aspects of designing upper boundaries for numerical simulations of oceanic and atmospheric flows as discussed earlier in particular in the context of three dimensional studies of flows bounded by “shallow water” or isentropic surfaces. Oceanic flows driven by observed tidal signals (P. Smolarkiewicz, personal communication) and data assimilation of free surface height data ([Gejadze and Copeland, 2004](#)) are two other examples of data-driven, direct applications.

The precise specification of a variety of gravity wave forcings in the numerical apparatus demonstrated in this thesis together with the accurate simulation of internal gravity wave behaviour would represent an appropriate testbed for internal gravity wave parametrizations. Their respective wave momentum fluxes could be diagnosed and compared with the corresponding DNS results to provide a validation of the, to some extent, uncertain underlying assumptions of existing internal wave parametrizations ([Kim et al., 2003](#)).

The zonal mean zonal flow oscillation that has been investigated in this thesis is generated by wave-induced vertical transport of momentum originating from the forcing boundaries. However, in the troposphere there are a number of waves which may similarly interact to create zonal mean flow oscillations resulting from meridional variations in which case the governing zonally averaged momentum equation results as

$$\frac{\partial U}{\partial t} = -\frac{\partial}{\partial y} \langle u'v' \rangle_x . \quad (5.2)$$

Such mean flow oscillations due to wave interference are only possible for the same or opposite zonal wavenumber in agreement with ([Lindzen et al., 1982](#)) who already noted the possibility of such horizontal vacillations in the atmosphere. The term on the right hand side of equation (5.2) is reminiscent of the term in ([Moncrieff, 2004](#)) formulating a forcing relation for the Madden-Julian oscillation (MJO) ([Madden and Julian, 1972, 1994](#)) which represents the major observed mode in the tropical troposphere and which is neither well understood nor accurately modelled in three-dimensional forecast or climate models. Therefore, the theory and the numerical apparatus used in this thesis may well be extended to provide a “laboratory” analogue for the MJO.



# Chapter 6

## Conclusions

In this thesis a new time-dependent, generalised vertical coordinate transformation has been introduced. Examples of applications relevant to a few distinct areas of computational fluid dynamics have been provided, validating both the conceptual and numerical aspects of the new time-dependent, generalised vertical coordinate transformation. A key feature of this development is the ability to collapse the spatial and temporal variations of the upper and lower boundaries to a single similarity variable defined in equation (2.7). This effectively encodes the relationship between an auxiliary boundary model and the interior fluid. In the atmospheric example presented in section 3.2, the simulation using the height of a selected isentrope in the definition of the vertical coordinate accurately represents the gravity waves generated above the obstacle.

In section 3.3 the practicality of the generalised coordinate transformation is successfully demonstrated for oceanic applications. In this example the free-surface boundary shape is predicted independently, providing the interior fluid model with a Neumann-type boundary condition for pressure, but maintaining the physicality of free-surface flows. While in theory — for incompressible or anelastic models — equivalent Dirichlet and Neumann boundary conditions may be found (cf. Gresho and Sani (1987) for a discussion), the use of a Dirichlet boundary condition can be impractical. In particular in the context of free surface flows, the application of a Dirichlet boundary condition for pressure in the numerical solution procedure for the interior domain allows fast propagating surface gravity waves in the solution, which severely limit the time-step. Furthermore, the shape of the upper boundary would remain unknown. Here, the novelty of the approach lies in the coupling of the independent auxiliary boundary model to the interior domain via the proposed vertical coordinate transformation, allowing the use of a larger time-step for the elaborate part of the interior domain computations.

Finally, the usefulness of the numerical framework has been demonstrated in the application to the laboratory experiment of Plumb and McEwan (1978). The comprehensive analysis of the direct numerical simulation of the QBO laboratory analogue exhibits a number of fundamental internal wave phenomena, which are also observed in the atmosphere: wave interference, wave reflection, wave-mean flow interaction, critical layer gravity wave attenuation and subsequent wave breaking. A number of numerical and parametric sensi-

tivities have been described. On the basis of the numerical results it confirms some of the findings obtained with simplified global circulation models (Horinouchi and Yoden, 1998) and NWP models (Untch, 1998; Giorgetta et al., 2002), while the accuracy of the direct numerical simulation removes the uncertainty with respect to the approximate nature of the global models. Furthermore, it enables to interpret those results and speculate on the remaining uncertainties with respect to atmospheric zonal mean zonal flow oscillations and their numerical realisability. In particular, the dominant role of randomly or semi-randomly distributed wave sources as originating from convection have been discussed. An alternative mechanism has been described in the laboratory simulations that does not necessitate the “obscure” dissipation of the descending shear layer and the role of viscosity in the laboratory experiment has been clarified which may allow to review the assumed dominant role of radiative cooling in the atmosphere (Holton and Lindzen, 1972; Dunkerton, 1997). The effects of stratification change on the vertical propagation of gravity waves have been discussed in determining the upper and lower bounds as well as the period change of a zonal mean zonal flow oscillation. Finally, suggestions have been offered on the numerical sensitivities and mechanisms reproducing a wave-driven zonal mean zonal flow oscillation in global circulation models.

# Appendix A

## Tensor algebra

### A.1 Curvilinear framework - the transformation of coordinates

The numerical investigations of specific meteorological problems require the selection of a suitable coordinate system. As shown by Gal-Chen and Somerville (1975); Dutton (1986); Zdunkowski and Bott (2003) and many others, the set of equations of motion, the thermodynamic equation and the continuity equation can be readily derived for a transformed system of coordinates. Prusa and Smolarkiewicz (2003) and in this thesis a general time dependent coordinate transformation is applied in the numerical model to ease the incorporation of intricate boundary conditions. The equations can be formulated in covariant or in contravariant form. In general, the temporal and spatial derivatives of the basis vectors do not vanish. As a result Christoffel symbols appear in the equations which represent inertial accelerations, affecting flow direction but not the flow magnitude. Numerical algorithms should preserve this “inertness” to avoid the introduction of artificial momentum sources. Truncation-error departures can be avoided if the momentum equations are solved for the untransformed Cartesian velocities in the transformed framework (Clark, 1977). This strong conservation formulation avoids Christoffel symbols resulting from the curvilinearity by using basis vectors  $\mathbf{i}_n$ , which are independent of time and independent of the coordinates (Clark, 1977; Smolarkiewicz et al., 1997). However, the advective velocities are the contravariant velocities of the transformed system. Therefore in a numerical model, two different forms of velocity have to be computed and stored, as described in chapter 2.

The concept of coordinate transformation is well known. Nevertheless, the main derivations of tensor analysis are compactly reviewed here for completeness. Furthermore, the less well known transformations of the Navier-Stokes equations in both, the general contravariant and the strong conservation formulation are reviewed. A new expression for the viscous terms in the strong conservation formulation is given for the general case of a not-necessarily Cartesian physical system.

The formulas of this appendix are readily applied to two specific examples. The first

example is the application of the standard transformation from Cartesian to spherical coordinates. The second example is the new generalised coordinate transformation described in detail in chapter 2. The transformation to spherical coordinates bears some relevance to the numerical modelling with the generalised coordinate on a sphere since the relevant metric conversion terms for each transformation are multiplicative.

### A.1.1 General definitions of tensor analysis

Two systems of linear independent basis vectors are called *reciprocal* if

$$\mathbf{q}^k \cdot \mathbf{q}_i = \delta_i^k, \quad (\text{A.1})$$

with the Kronecker-symbol  $\delta_i^k = 1$  for  $i = k$  and zero otherwise. It is customary to refer to upper indices  $i$  as *contravariant* and to lower indices  $i$  as *covariant*. In the following derivations both upper and lower indices will appear in the equations. A *contravariant system* is defined as a system where the basis vectors are covariant (the equations written in the vector component form only contain upper indices), and it is referred to a *covariant system* where the basis vectors are contravariant.<sup>1</sup>

In a Cartesian framework a vector  $\mathbf{A}$  and a tensor  $\mathbb{J}$  can be written as

$$\mathbf{A} = A^n|_{(x,y,z)} \mathbf{i}_n \quad (\text{A.2})$$

$$\mathbb{J} = J^{nm}|_{(x,y,z)} \mathbf{i}_n \mathbf{i}_m \quad (\text{A.3})$$

where the normal summation rules apply, i.e. repeated indices express sums unless otherwise stated.  $A^n$  denotes the measure number of the vector  $\mathbf{A}$ . In general coordinates with contravariant measure numbers  $A^n|_q$  and covariant basis vectors  $\mathbf{q}_n$ , a vector  $\mathbf{A}$  and a tensor  $\mathbb{J}$  can be expressed as

$$\mathbf{A} = A^n|_{(q^1,q^2,q^3)} \mathbf{q}_n \quad (\text{A.4})$$

$$\mathbb{J} = J^{nm}|_{(q^1,q^2,q^3)} \mathbf{q}_n \mathbf{q}_m, \quad (\text{A.5})$$

where the basis vectors  $\mathbf{q}_n$  and their measure numbers  $q^n$  may be functions of the original Cartesian coordinates. The basis vectors of the general coordinate system may not be orthogonal to each other and may not be unit vectors. The notation of the same physical vector  $\mathbf{A}$  in the two different coordinate systems (A.2) and (A.4) expresses the invariance of a vector with respect to the transformation.

With the definition of the scalar triple product, which represents the volume of the parallelepiped bounded by the three vectors  $\mathbf{A}, \mathbf{B}$  and  $\mathbf{C}$  (Chisholm, 1978; Zdunkowski and Bott, 2003)

$$[\mathbf{A}, \mathbf{B}, \mathbf{C}] \equiv \mathbf{A} \cdot \mathbf{B} \times \mathbf{C} \quad (\text{A.6})$$

---

<sup>1</sup>The choice of system is arbitrary but considerations with respect to properties of the covariant and contravariant partial derivatives favour the contravariant system (Zdunkowski and Bott, 2003).

and using (A.2) and (A.4) the scalar triple product is given by the determinant

$$\mathbf{A} \cdot \mathbf{B} \times \mathbf{C} = \begin{vmatrix} A_x & A_y & A_z \\ B_x & B_y & B_z \\ C_x & C_y & C_z \end{vmatrix} = \overline{G}|_{(q^1, q^2, q^3)} \begin{vmatrix} A^1 & A^2 & A^3 \\ B^1 & B^2 & B^3 \\ C^1 & C^2 & C^3 \end{vmatrix} \quad (\text{A.7})$$

with  $\overline{G}|_{(x, y, z)} = 1$  in a Cartesian coordinate system.  $\overline{G}|_{(q^1, q^2, q^3)} \equiv [\mathbf{q}_1, \mathbf{q}_2, \mathbf{q}_3]$  in an arbitrary coordinate system is the square root of the matrix determinant (“GRAMSche Determinante”) of the basis vectors  $\mathbf{q}_i$  which is defined as

$$\overline{G}^2 \equiv |\overline{g}_{ij}| = [\mathbf{q}_1, \mathbf{q}_2, \mathbf{q}_3]^2 = \begin{vmatrix} \mathbf{q}_1 \cdot \mathbf{q}_1 & \mathbf{q}_1 \cdot \mathbf{q}_2 & \mathbf{q}_1 \cdot \mathbf{q}_3 \\ \mathbf{q}_2 \cdot \mathbf{q}_1 & \mathbf{q}_2 \cdot \mathbf{q}_2 & \mathbf{q}_2 \cdot \mathbf{q}_3 \\ \mathbf{q}_3 \cdot \mathbf{q}_1 & \mathbf{q}_3 \cdot \mathbf{q}_2 & \mathbf{q}_3 \cdot \mathbf{q}_3 \end{vmatrix}. \quad (\text{A.8})$$

Given a line element in the  $q^i$ -system

$$d\mathbf{r}(q^1, q^2, q^3) = \frac{\partial \mathbf{r}}{\partial q^n} dq^n = \mathbf{q}_n dq^n \quad (\text{A.9})$$

with  $\mathbf{r} \equiv x\mathbf{i}_1 + y\mathbf{i}_2 + z\mathbf{i}_3$  defined in the Cartesian system,  $\overline{G}|_{(q^1, q^2, q^3)}$  can be expressed using  $\mathbf{q}_i = \partial \mathbf{r} / \partial q^i$ . The result is understood more generally as the Jacobian of the transformation from an initial coordinate system  $(x, y, z, t)$  into the system  $(q^1, q^2, q^3, t)$  with

$$\overline{G}|_{(q^1, q^2, q^3)} \equiv |\overline{g}_{ij}|^{1/2} = \left| \frac{\partial(q^1, q^2, q^3)}{\partial(x, y, z)} \right|^{-1} = |\overline{g}^{ij}|^{-1/2}. \quad (\text{A.10})$$

The covariant basis vectors can be expressed in terms of the contravariant basis vectors and vice versa using (A.10) and (A.1) according to

$$\mathbf{q}_i = \frac{1}{\overline{G}} (\mathbf{q}^j \times \mathbf{q}^k) \quad (\text{A.11})$$

$$\mathbf{q}^i = \frac{1}{\overline{G}} (\mathbf{q}_j \times \mathbf{q}_k). \quad (\text{A.12})$$

The gradient of a vector  $\nabla \mathbf{A}$  in the contravariant system can be written as

$$\begin{aligned} \nabla \mathbf{A} &= \mathbf{q}^n \frac{\partial}{\partial q^n} \mathbf{A} \\ &= \frac{1}{\overline{G}} \left\{ \frac{\partial}{\partial q^1} (\mathbf{q}_2 \times \mathbf{q}_3 \mathbf{A}) + \frac{\partial}{\partial q^2} (\mathbf{q}_3 \times \mathbf{q}_1 \mathbf{A}) + \frac{\partial}{\partial q^3} (\mathbf{q}_1 \times \mathbf{q}_2 \mathbf{A}) \right\}. \end{aligned} \quad (\text{A.13})$$

As before, a basis vector  $\mathbf{q}_i$  is expressed in terms of the Cartesian coordinates as

$$\mathbf{q}_i = \frac{\partial x^n}{\partial q^i} \mathbf{i}_n. \quad (\text{A.14})$$

With (A.14) the transformation for the measure numbers of a vector  $\mathbf{A}$  is then given by

$$A^i|_{(q^1, q^2, q^3)} = \frac{\partial x^n}{\partial q^i} A^n|_{(x, y, z)}. \quad (\text{A.15})$$

It follows that the contravariant measure numbers of  $g^{ij}$  or in fact any tensor component  $J^{ij}$  in general coordinates is expressed in terms of their corresponding Cartesian components to give

$$J^{ij}|_{(q^1, q^2, q^3)} = \frac{\partial q^i}{\partial x^n} \frac{\partial q^j}{\partial x^m} J^{nm}|_{(x, y, z)} \quad (\text{A.16})$$

$$g^{ij} = \frac{\partial q^i}{\partial x^n} \frac{\partial q^j}{\partial x^n}. \quad (\text{A.17})$$

In a Cartesian framework the metric terms  $g^{ij} = \delta^{ij}$ . With the metric tensor terms expressed as  $g_{ij} = \mathbf{q}_i \cdot \mathbf{q}_j$  a unit vector in the  $(q^1, q^2, q^3, t)$  coordinate system is given as

$$\mathbf{e}_i = \frac{\mathbf{q}_i}{|\mathbf{q}_i|} = \frac{\mathbf{q}_i}{\sqrt{\mathbf{q}_i \cdot \mathbf{q}_i}} = \frac{\mathbf{q}_i}{\sqrt{g_{ii}}}. \quad (\text{A.18})$$

Using the expression (A.4) for the vector  $\mathbf{A}$  in (A.13) and computing the first scalar of the expression  $\nabla \mathbf{A}$  leads to the divergence of a vector in general coordinates

$$\nabla \cdot \mathbf{A} = \frac{1}{G} \frac{\partial (\overline{G} A^n)}{\partial q^n}. \quad (\text{A.19})$$

In order to express the equations of motion in a general coordinate system, an expression for the material derivative  $D/Dt$  (in general not equal the total derivative  $d/dt$ ) of the velocity vector  $\mathbf{v} = v^n \mathbf{q}_n$  has to be derived. It follows

$$\frac{D\mathbf{v}}{Dt} = \frac{d}{dt}(v^n \mathbf{q}_n) = \frac{dv^n}{dt} \mathbf{q}_n + v^n \frac{d\mathbf{q}_n}{dt}, \quad (\text{A.20})$$

noting that the derivatives of the basis vectors in the general  $q^i$  coordinate system do not vanish. By multiplying (A.20) with  $\mathbf{q}^k$  and introducing Christoffel symbols of the 2nd kind  $\Gamma_{ij}^k$ , the  $k$ th component of the momentum equation in contravariant measure numbers reads

$$\mathbf{q}^k \cdot \frac{D\mathbf{v}}{Dt} = \frac{dv^k}{dt} + v^m v^n \Gamma_{nm}^k - v^n \mathbf{q}_n \cdot \frac{\partial \mathbf{q}^k}{\partial t} \quad (\text{A.21})$$

with

$$\frac{\partial \mathbf{q}_i}{\partial q^j} = \Gamma_{ij}^m \mathbf{q}_m, \quad (\text{A.22})$$

and

$$\Gamma_{ij}^k = \frac{\partial^2 x^n}{\partial q^i \partial q^j} \frac{\partial q^k}{\partial x^n} = \frac{g^{kn}}{2} \left( \frac{\partial g_{in}}{\partial q^j} + \frac{\partial g_{jn}}{\partial q^i} - \frac{\partial g_{ij}}{\partial q^n} \right). \quad (\text{A.23})$$

The importance of the last term on the right hand side of equation (A.21) for time dependent geometries in this contravariant formulation has been recently discussed by Luo and Bewley (2004). They find that the time-dependent terms cannot be neglected, in particular for rapidly varying geometries.

### A.1.2 The momentum equation

In a stationary inertial system the equations of motion are given in the form

$$\frac{D\mathbf{v}}{Dt} = -\frac{1}{\rho}\nabla p + \mathbf{g} + \frac{1}{\rho}\nabla \cdot \boldsymbol{\tau}, \quad (\text{A.24})$$

with the physical pressure  $p$ , gravity vector  $\mathbf{g}$ , density  $\rho$  and the deviatoric stress tensor  $\boldsymbol{\tau}$ . The  $k$ th component of the contravariant form of (A.24) can be found by multiplying the equation with the contravariant vector  $\mathbf{q}^k$  and expressing the gradient operator  $\nabla$  as

$$\nabla = \mathbf{q}_m \nabla^m = \mathbf{q}_m \frac{\partial}{\partial q_m} = g^{mn} \mathbf{q}_m \frac{\partial}{\partial q^n}. \quad (\text{A.25})$$

Using (A.21), (A.25) and (A.14) gives then

$$\frac{dv^k}{dt} + v^m v^n \Gamma_{nm}^k - v^n \mathbf{q}_n \cdot \frac{\partial \mathbf{q}^k}{\partial t} = -\frac{g^{kn}}{\rho} \frac{\partial p}{\partial q^n} - g \frac{\partial q^k}{\partial x^3} + \frac{1}{\rho} \mathbf{q}^k \cdot \nabla \cdot \boldsymbol{\tau}. \quad (\text{A.26})$$

The  $k$ th-component of the divergence of the viscous stress tensor (using (A.19) and (A.23)) can be written as

$$\mathbf{q}^k \cdot \nabla \cdot \boldsymbol{\tau} = \frac{1}{\bar{G}} \frac{\partial (\bar{G} \tau^{kn})}{\partial q^n} + \tau^{mn} \Gamma_{mn}^k, \quad (\text{A.27})$$

where the components  $\tau^{jk}|_{q^i}$  are given by (A.16). The coefficients in Cartesian space  $\tau^{jk}|_{x^i}$  are defined proportional to the mean gradients of the velocity following Lilly (1962) (see also Gal-Chen and Somerville (1975) for details).

### A.1.3 The momentum equation in strong conservation formulation

The difficulty in expressing the Christoffel symbols numerically in a conserving form is eliminated by the use of a strong conservation formulation (Clark, 1977). This entails the inconvenience to compute and store at least two different representations of the velocity components in the model.

In the strong conservation formulation, the physical velocity is expressed as

$$\mathbf{v} = u^n \mathbf{i}_n \quad (\text{A.28})$$

where the  $\mathbf{i}_n$  are assumed orthogonal and stationary but not necessarily Cartesian. Using the total derivative  $d/dt$  in the transformed  $q^i$  system one can write

$$\frac{d\mathbf{v}}{dt} = \frac{\partial u^n}{\partial t} \mathbf{i}_n + \dot{q}^m \frac{\partial u^n}{\partial q^m} \mathbf{i}_n. \quad (\text{A.29})$$

Equation (A.29) contains the advective velocity components of the transformed system  $\dot{q}^i$  given by

$$\dot{q}^i \equiv \frac{dq^i}{dt} = \frac{\partial q^i}{\partial t} + u^n \frac{\partial q^i}{\partial x^n}. \quad (\text{A.30})$$

Using partial derivatives, the vector operator  $\nabla$  can be expressed in this system as

$$\mathbf{i}_n \frac{\partial}{\partial x^n} = \mathbf{i}_n \nabla_n|_{(x,y,z)} = \mathbf{i}_n \frac{\partial q^m}{\partial x^n} \nabla_m|_{(q^1,q^2,q^3)} = \mathbf{i}_n \frac{\partial q^m}{\partial x^n} \frac{\partial}{\partial q^m}. \quad (\text{A.31})$$

For a reference space spanned by the basis vectors  $\mathbf{i}_n$  the equations of motion for the untransformed physical velocities along the coordinate lines  $q^i$  of the transformed system are now written as

$$\frac{\partial u^n}{\partial t} \mathbf{i}_n + \dot{q}^m \frac{\partial u^n}{\partial q^m} \mathbf{i}_n = -\frac{1}{\rho} \frac{\partial q^m}{\partial x^n} \frac{\partial p}{\partial q^m} \mathbf{i}_n - g \delta^{n3} + F^n \mathbf{i}_n + \mathcal{V}^n \mathbf{i}_n. \quad (\text{A.32})$$

In the general case if the reference space  $\mathbf{i}$  is not Cartesian, the derivation of the viscous terms is tedious. A summary of the derivation and the full expression of the  $\mathcal{V}^j$  in equation (A.32) has been argued in [Smolarkiewicz and Prusa \(2004\)](#) from first principles and is given as

$$\mathcal{V}^j = \frac{1}{\rho^*} \frac{\partial}{\partial q^p} \left( \rho^* \tilde{G}_k^p \sqrt{g_{jj} g_{kk}} \tau^{jk} \right) - \tau^{jk} \frac{\partial \sqrt{g_{jj}}}{\partial x^k} + \sqrt{g_{jj}} \tau^{mn} \Gamma_{mn}^j \quad (\text{A.33})$$

with the components of the deviatoric stress tensor given as

$$\tau^{jk}|_{(q^1,q^2,q^3)} = 2\nu g^{jj} g^{kk} \epsilon_{jk} + \iota g^{jk} \overline{v^s}^m \frac{\partial \ln \rho^*}{\partial q^m}, \quad (\text{A.34})$$

where  $\nu := \mu/\rho$  is the kinematic viscosity and  $\mu$  is the molecular viscosity;  $\iota := \lambda/\rho$  denotes the density normalised bulk viscosity;  $\overline{v^s}$  is the solenoidal velocity defined in (2.5). The symmetric strain rate tensor is given as

$$\epsilon_{jk}|_{(q^1,q^2,q^3)} = \frac{1}{2} \left( \sqrt{g_{kk}} \tilde{G}_k^l \frac{\partial \sqrt{g_{jj}} v^j}{\partial q^l} + \sqrt{g_{jj}} \tilde{G}_j^r \frac{\partial \sqrt{g_{kk}} v^k}{\partial q^r} - \sqrt{g_{mm}} v^m \Gamma_{jk}^m \right). \quad (\text{A.35})$$

In Cartesian coordinates, it is easily verified that the strain rate tensor is

$$\epsilon_{jk}|_{(x,y,z)} \equiv \frac{1}{2} \left( \frac{\partial v^k}{\partial x^j} + \frac{\partial v^j}{\partial x^k} \right), \quad (\text{A.36})$$

and the components of the deviatoric stress tensor are given as

$$\tau_{jk}|_{(x,y,z)} \equiv 2\nu \epsilon_{jk}|_{(x,y,z)} + \iota \epsilon_{jk}|_{(x,y,z)} \delta_{jk}. \quad (\text{A.37})$$

#### A.1.4 The continuity equation

With (A.19) the continuity equation is expressed in general coordinates as

$$\frac{\partial(\rho \overline{G})}{\partial t} + \frac{\partial(\rho \overline{G} \dot{q}^n)}{\partial q^n} = 0. \quad (\text{A.38})$$

Note, that this formulation is general and requires the velocity components of the transformed system  $\dot{q}^i$ .



### A.1.5 Spherical coordinates

For completeness and later reference one example of a non-Cartesian physical reference system is introduced with its corresponding diagonal elements of the conjugate metric tensor: a sphere. The transformation from a Cartesian  $(x, y, z)$  to a spherical  $(\lambda, \phi, r)$  coordinate system can be described as

$$\begin{aligned} x &= r \cos(\phi) \cos(\lambda) \\ y &= r \cos(\phi) \sin(\lambda) \\ z &= r \sin(\phi), \end{aligned} \quad (\text{A.39})$$

with longitude  $\lambda$ , latitude  $\phi$  and distance from the centre  $r$  (Holton, 1992). The relations (A.39) represent the  $x^i$ -coordinates expressed through the new  $q^i$ -coordinate lines. If one further introduces a second set of coordinates  $(\hat{x}, \hat{y}, \hat{z})$ :

$$\begin{aligned} \hat{x} &= a\lambda \\ \hat{y} &= a\phi \\ \hat{z} &= r - a \end{aligned} \quad (\text{A.40})$$

where  $a = 6.37122 \times 10^6 m$  is the radius of the Earth, above transformation can be written as

$$\begin{aligned} x &= a\gamma \cos(\hat{y}/a) \cos(\hat{x}/a) \\ y &= a\gamma \cos(\hat{y}/a) \sin(\hat{x}/a) \\ z &= a\gamma \sin(\hat{y}/a) \end{aligned} \quad (\text{A.41})$$

with

$$\gamma \equiv \frac{r}{a} = \frac{a + \hat{z}}{a}. \quad (\text{A.42})$$

Using (A.16) the metric terms  $g_{ij}$  can be computed for the transformation given in (A.41) as

$$\begin{aligned} g_{11} &= \gamma^2 \cos^2(\hat{y}/a) \\ g_{22} &= \gamma^2 \\ g_{33} &= 1 \\ g_{ij} &= 0 \text{ for all } i \neq j. \end{aligned} \quad (\text{A.43})$$

With (A.18) one finds the physical velocity components on the sphere (ie. in the transformed system with transformed unit vectors) as

$$\begin{aligned} \mathbf{u}_{(\hat{x}, \hat{y}, \hat{z})} &= \dot{\hat{x}} \mathbf{q}_{\hat{x}} + \dot{\hat{y}} \mathbf{q}_{\hat{y}} + \dot{\hat{z}} \mathbf{q}_{\hat{z}} \\ &= \gamma \cos(\hat{y}/a) \dot{\hat{x}} \mathbf{e}_{\hat{x}} + \gamma \dot{\hat{y}} \mathbf{e}_{\hat{y}} + \dot{\hat{z}} \mathbf{e}_{\hat{z}} \\ &= u \mathbf{e}_{\hat{x}} + v \mathbf{e}_{\hat{y}} + w \mathbf{e}_{\hat{z}}. \end{aligned} \quad (\text{A.44})$$

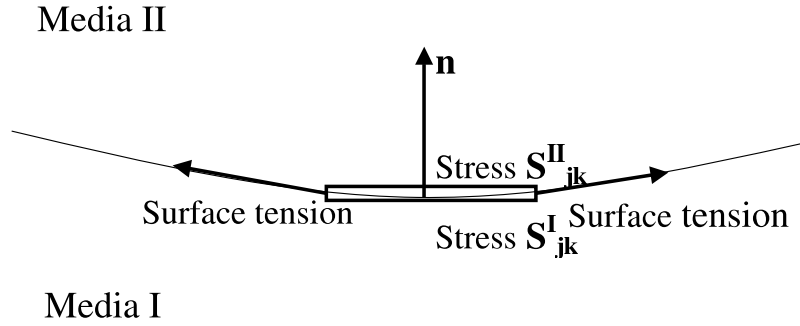


Figure A.1: Relation between the stresses on the two sides of a boundary between two fluids (after Batchelor (1967), pp. 69).

The contravariant velocity components  $(\dot{x}, \dot{y}, \dot{z})$  expressed through the physical velocities on the sphere  $(u, v, w)$  (cf. Holton (1992)) are given by

$$\begin{aligned}\dot{x} &= \frac{u}{\gamma \cos(\hat{y}/a)} \\ \dot{y} &= \frac{v}{\gamma} \\ \dot{z} &= w.\end{aligned}\tag{A.45}$$

### A.1.6 Free surface boundary condition

The variety of formal *free surface* definitions found in the literature reflects the variety of applications in which the free surface concept applies (e.g., the definition via pressure in atmospheric studies (Dutton, 1986), or the definition via the Bernoulli equation in potential flow theory, see Stoker (1957), pp. 19). However, different formulations are often the result of simplifications (see for example Lamb (1975), pp. 363), introduced to the more general concept presented in Batchelor (1967), pp. 148-150, and summarised here.

Given an impermeable material surface separating two media, as defined in the *kinematic condition* (1.23), one has in general two more conditions describing the transition of a transportable quantity (e.g. fluid momentum) from one side of the interface to the other side (Batchelor, 1967). Considering fluid momentum, the first transition relation is the continuity of the velocity across the interface. This is discussed in section 1.5.3 for the special case of a fluid-solid interface with *no slip* boundary condition. The second transition relation assumes the continuity of the stress across the interface (Batchelor, 1967). This relation is determined by a balance calculation of the forces at the interface (see figure A.1 and Batchelor (1967), pp. 69). The stress tensor components are given as

$$\mathcal{S}_{jk} = -p\delta_{jk} + \tau_{jk},\tag{A.46}$$

where the  $\tau_{jk}$  denote the components of the deviatoric stress given in equation (A.37). A balance of the forces at the interface between fluid *I* and *II* including surface tension  $\mathcal{T}$

gives

$$\mathcal{S}_{jk}^{II} n_k - \mathcal{S}_{jk}^I n_k = \mathcal{T}. \quad (\text{A.47})$$

If for convenience, the tangential component of the surface force  $\mathbf{t} \cdot \mathbf{S} \cdot \mathbf{n}$  and the normal component  $\mathbf{n} \cdot \mathbf{S} \cdot \mathbf{n}$  are treated separately, using equation (A.37), and in the absence of surface tension one obtains the two conditions

$$\begin{aligned} \nu^{II} \epsilon_{jk}^{II} t_j n_k &= \nu^I \epsilon_{jk}^I t_j n_k, \\ p^{II} - 2\nu^{II} \epsilon_{jk}^{II} n_j n_k + \iota^{II} \epsilon_{jk}^{II} \delta_{jk} &= p^I - 2\nu^I \epsilon_{jk}^I n_j n_k + \iota^I \epsilon_{jk}^I \delta_{jk}. \end{aligned} \quad (\text{A.48})$$

In the special case where the kinematic viscosity and the density normalised bulk viscosity of fluid  $II$  are negligible compared to fluid  $I$ , one finds for the bounding surface of fluid  $I$

$$\begin{aligned} \epsilon_{jk}^I t_j n_k &= 0, \\ p^I - 2\nu^I \epsilon_{jk}^I n_j n_k + \iota^I \epsilon_{jk}^I \delta_{jk} &= p^{II}, \end{aligned} \quad (\text{A.49})$$

which defines a *free surface* of fluid  $I$ . In the absence of viscosity, surface tension and other external forces, the conditions (A.49) express the invariance of pressure at the (moving) impermeable bounding surface. This may be combined with (1.23) to give

$$\frac{dF}{dt} := \frac{d(p^I - p^{II})}{dt} = 0 \text{ at } F(x, y, z, t) = 0. \quad (\text{A.50})$$

If pressure is negligible in the upper fluid  $p^{II} \approx 0$  one recovers Baines' free surface condition of vanishing pressure at the interface.

## A.2 Symbol tables

Table A.1: Description of Abbreviations.

<i>DLR</i>	Deutsches Zentrum für Luft- und Raumfahrt
<i>DNS</i>	Direct numerical simulation
<i>ECMWF</i>	European Centre for Medium Range Weather Forecast
<i>FCT</i>	flux-corrected transport
<i>GESIMA</i>	Geesthachter Simulationsmodell der Atmosphäre
<i>LES</i>	Large eddy simulation
<i>MESOSCOF</i>	Mesoscale flow and cloud model Oberpfaffenhofen
<i>MPDATA</i>	Multidimensional positive definite advection transport algorithm
<i>NCAR</i>	National Centre for Atmospheric Research
<i>NFT</i>	Nonoscillatory forward-in-time
<i>QBO</i>	Quasi-biennial oscillation
<i>SAO</i>	Semi-annual oscillation
<i>TVD</i>	total variation diminishing

Table A.2: Description of symbols in the text.

$\rho; \rho_b; \rho^*; \rho_r, \rho_0$	density; anelastic density; Jacobian weighted density; reference density	$[kgm^{-3}]$
$\rho_*$	restratified density profile after re-ordering	$[kgm^{-3}]$
$\theta$	potential temperature	$[K]$
$\theta_b$	reference potential temperature	$[K]$
$\theta'$	potential temperature perturbation	$[K]$
$b'$	buoyancy perturbation	$[ms^{-2}]$
$\pi'$	normalised pressure perturbation	$[m^2s^{-2}]$
$\phi', p'$	pressure perturbation	$[Nm^{-2}]$
$v^j; u, v, w$	physical velocity	$[ms^{-1}]$
$u_e, v_e, w_e, \rho_e, \theta_e$	environmental (ambient) profile(s)	
$\bar{\rho}, \bar{p}$	environmental (ambient) hydrostatically balanced density, pressure	
$g; g^*$	gravity acceleration; reduced gravity	$[ms^{-2}]$
$N$	Brunt-Väisällä frequency	$[s^{-1}]$
$\nu := \mu/rho$	kinematic viscosity	$[m^2s^{-1}]$
$\mu$	molecular viscosity	$[kgm^{-1}s^{-1}]$
$\iota := \lambda/rho$	density normalised bulk viscosity	$[m^2s^{-1}]$
$\kappa$	diffusivity (of salt or heat)	$[m^2s^{-1}]$

Table A.2: continued...

$U; \mathbf{V}_{\text{crit}} = (U_{\text{crit}}, V_{\text{crit}})$	characteristic or background zonal mean flow velocity; critical mean flow velocity	$[ms^{-1}]$
$\bar{u}^t, \bar{\rho}^t, \bar{w}$	time interval averaged zonal velocity, density, vertical velocity	
$F_u$	$U/\sqrt{gd_0}$ , undisturbed Froude number	
$Ri$	$-(g/\rho)(\partial\rho/\partial z)/((\partial u/\partial z)^2 + (\partial v/\partial z)^2)$ , local or gradient Richardson number	
$z_s; z_{s0}; a$	surface topography; mountain height; mountain half-width	$[m]$
$H; H_0$	height of the top surface, physical system; transformed system	$[m]$
$L_x, L_y$	zonal, meridional domain size	$[m]$
$L; T$	characteristic length; time	
$d_1; d_0$	shallow-water fluid depth; undisturbed depth	$[m]$
$\epsilon$	forcing amplitude	$[m]$
$\gamma$	attenuation depth of changing ambient profile	$[m]$
$\mathbf{i}_i$	i-th (Cartesian) unit vector in physical system	
$\mathbf{q}_i, q_i; \mathbf{q}^i, q^i$	i-th covariant unit vector in transformed system, respective coordinate; i-th contravariant unit vector, respective coordinate	
$\mathbb{J}, \mathbf{A}$	a tensor ; a vector	
$\Gamma_{ij}^k$	Christoffel symbol of the 2nd kind	
$x^j; x, y, z, t$	physical coordinates	
$\bar{x}^j; \bar{x} \equiv E, \bar{y} \equiv D, \bar{z} \equiv C, \bar{t}$	transformed coordinates	
$\xi$	generalised vertical coordinate	
$\overline{v^{*j}}; \dot{\bar{x}}^j$	transformed contravariant velocity components	
$\overline{v^{sj}}$	transformed solenoidal velocity components	
$\overline{G}; \overline{G}_0$	Jacobian of the transformation	
$\tilde{G}_j^k$	transformation coefficient $j, k$	
$g^{ij}$	$i, j$ element of the conjugate metric tensor of the physical system	
$\delta_i^k$	Kronecker-symbol	
$R; F^j$	right hand side (rhs); rhs forcing terms in the momentum equation	
$\tau, \tau_{ij}$	$(i, j$ element of) viscous or deviatoric stress tensor	
$\mathcal{V}$	viscous term in momentum equation	

Table A.2: continued...

$\mathcal{H}$	diffusive term in thermodynamic equation	
$\mathcal{D}$	dissipative term in kinetic energy equation	
$\mathcal{S}$	stress tensor	
$\mathcal{T}$	surface tension	
$k, l, m$	dimensional zonal ( $\equiv 2\pi s/L_x$ ), meridional, vertical wave number	$[m^{-1}]$
$s$	non-dimensional zonal wave-number	
$\omega; \omega_0$	wave frequency; forcing frequency	$[s^{-1}]$
$c_x, c := \omega/k$	horizontal wave phase speed	$[ms^{-1}]$
$\sigma; \sigma_\nu; \sigma_\kappa$	dispersion relation; $\nu(m^2 + k^2); \kappa(m^2 + k^2)$	
$\psi; \hat{\psi}, \psi_0$	stream function; vertical structure of stream function	
$\mathcal{A} = \mathcal{E}/(\omega_0 - Uk)$	wave action	$[kgs^{-1}m^{-1}]$
$\mathcal{E}$	wave energy density	$[Nm^{-2}]$
$E_k; \overline{K}; K'$	kinetic energy; mean ; transient;	$[Nm]$
$E_p; E_b; E_a$	potential energy; background; available;	$[Nm]$
$z_j; \hat{z}_k$	complex data value; Fourier transformed complex value;	
$\mathcal{R}(x)$	Real part of complex value x	
$\mathcal{I}(x)$	Imaginary part of complex value x	
$\mathcal{O}(x)$	scaling, in the order of x	

# Bibliography

- Anderson, D., J. Tannehill, and R. Pletcher (1984). *Computational Fluid Mechanics and Heat Transfer*. New York: Hemisphere Publ. Corp. [3](#)
- Andrews, D. and M. McIntyre (1978). On wave-action and its relatives. *J. Fluid Mech.* *89*, 647–664. Corrigendum Vol 95, pp. 796; also Vol. 106, pp.331. [72](#)
- Baines, P. (1995). *Topographic effects in stratified flows*. Cambridge, New York: Cambridge University Press. [11](#), [12](#), [14](#), [15](#), [50](#), [52](#), [71](#), [72](#), [90](#)
- Baldwin, M., L.J., T. Dunkerton, K. Hamilton, P. Haynes, W. Randel, J. Holton, M. Alexander, I. Hirota, T. Horinouchi, D. Jones, J. Kinnersley, C. Marquardt, K. Sato, and M. Takahashi (2001). The quasi-biennial oscillation. *Reviews Geophys.* *39*(2), 179–229. [4](#), [5](#), [89](#)
- Batchelor, G. (1967). *An Introduction to Fluid Dynamics*. New York, London: Cambridge University Press. [15](#), [17](#), [104](#)
- Bleck, R. (1974). Short range prediction in isentropic coordinates with filtered and unfiltered numerical models. *Mon. Weather Rev.* *102*, 813–829. [2](#)
- Bleck, R. and L. Smith (1990). A wind-driven isopycnic coordinate model of the north and equatorial atlantic ocean I: Model development and supporting experiments. *J. Geophys. Res.* *95C*, 3273–3285. [2](#)
- Booker, J. and F. Bretherton (1967). The critical layer for internal gravity waves in a shear flow. *J. Fluid Mech.* *27*, 513–539. [11](#)
- Bougeault, P. (1983). A non-reflective upper boundary condition for limited-height hydrostatic models. *Mon. Weather Rev.* *111*, 229–247. [1](#), [18](#)
- Bretherton, F. (1966). The propagation of groups of internal gravity waves in a shear flow. *Q.J.R. Meteorol. Soc.* *92*, 466–480. [11](#), [69](#), [72](#)
- Bronstein, I. and K. Semendjajew (1987). *Taschenbuch der Mathematik* (23rd ed.). Verlag Harri Deutsch: Thun and Frankfurt: Grosche G, Ziegler V, Ziegler D (eds). [42](#)

- Casulli, V. (1999). A semi-implicit finite difference method for non-hydrostatic, free surface flows. *Int. J. Numer. Methods Fluids* 30, 425–440. 16, 39
- Casulli, V. and R. Cheng (1992). Semi-implicit finite difference methods for three dimensional shallow water flow. *Int. J. Numer. Methods Fluids* 15, 629–648. 16, 39
- Chisholm, J. (1978). *Vectors in three-dimensional space*. Cambridge, New York: Cambridge University Press. 98
- Chu, P. (1999). Two kinds of predictability in the Lorenz system. *J. Atmos. Sci.* 56, 1427–1432. 1
- Clark, T. (1977). A small scale dynamic model using a terrain following coordinate transformation. *J. Comput. Phys.* 24, 186–215. 3, 97, 101
- Clark, T. and R. Farley (1984). Severe downslope windstorm calculations in two and three spatial dimensions using anelastic interactive grid nesting: A possible mechanism for gustiness. *J. Atmos. Sci.* 41, 329–350. 22
- Clark, T. and M. Miller (1991). Pressure drag and momentum fluxes due to the alps II: Representation in large-scale atmospheric models. *Q.J.R. Meteorol. Soc.* 117, 527–552. 30
- Courant, R. and D. Hilbert (1989). *Courant & Hilbert (classics ed.)*, Volume II. J. Wiley & Sons, New York: Wiley Interscience Publishers. 12, 13
- Daley, R. (1988). The normal modes of the spherical non-hydrostatic equations with applications to the filtering of acoustic modes. *Tellus* 40A, 96–106. 10
- Drazin, P. and W. Reid (1981). *Hydrodynamic stability*. Cambridge, New York: Cambridge University Press. 10, 11, 49, 69
- Dunkerton, T. (1981). Wave transience in a compressible atmosphere. Part II: Transient equatorial waves in the quasi-biennial oscillation. *J. Atmos. Sci.* 38, 298–307. 5, 6, 7, 89
- Dunkerton, T. (1997). The role of gravity waves in the quasi-biennial oscillation. *J. Geophys. Res.* 102(D22), 26053–26076. 6, 96
- Durrant, D. (1999). *Numerical methods for wave equations in geophysical fluid dynamics*. New York: Springer-Verlag. 12, 13, 26
- Dutton, J. (1986). *The Ceaseless Wind*. Dover Publications Inc. 2, 15, 97, 104
- Egger, J. and K. Hoinka (1992). Fronts and orography. *Meteorol. Atmos. Phys.* 48, 3–36. 11



- Eliassen, A. and E. Palm (1961). On the transfer of energy in stationary mountain waves. *Geophys. Publ.* 22, 1–23. 69
- Flynn, M. and B. Sutherland (2004). Intrusive gravity currents and internal gravity wave generation in stratified fluid. *J. Fluid Mech.* 514, 355–383. 90
- Freudenthal, H. (1970-1980). *Dictionary of Scientific Biography*, Volume I-XVI, Chapter Riemann. New York: C.C. Gillispie, Scribner & Sons. 2
- Gabis, I. and O. Troshichev (2005). QBO cycle identified by changes in height profile of the zonal winds: new regularities. *J. Atm. Sol. Terr. Phys.* 67, 33–44. 89
- Gal-Chen, T. and C. Somerville (1975). On the use of a coordinate transformation for the solution of the Navier-Stokes equations. *J. Comput. Phys.* 17, 209–228. 1, 3, 97, 101
- Galmiche, M., O. Thual, and P. Bonneton (2000). Wave/wave interaction producing horizontal mean flows in stably stratified fluids. *Dyn. Atm. Ocean* 31, 193–207. 7, 71, 73, 85
- Gejadze, I. and G. Copeland (2004). Adjoint sensitivity analysis for fluid flow with free surface. *Int. J. Numer. Methods Fluids*. submitted. 87, 94
- Gibson, J., P. Kallberg, S. Uppala, A. Hernandez, A. Nomura, and E. Serrano (1999). ECMWF re-analysis project report series: 1. ERA-15 description. Technical report, ECMWF, Shinfield Park, Reading. 6
- Gill, A. (1982). *Atmosphere-Ocean Dynamics*, Volume 30 of *International geophysics series*. London: Academic Press. 8, 10, 30, 35, 61, 71
- Giorgetta, M., E. Manzini, and E. Roeckner (2002). Forcing of the quasi-biennial oscillation from a broad spectrum of atmospheric waves. *Geophys. Res. Lett.* 29(8), 86–1–86–4. 7, 91, 96
- Givoli, D. (1991). Non-reflecting boundary conditions. *J. Comput. Phys.* 94, 1–29. 1, 18
- Greiner, W. and H. Stock (1991). *Hydrodynamik* (4. Auflage ed.), Volume 2A of *Theoretische Physik*. Verlag Harri Deutsch. 17
- Gresho, P. and R. Sani (1987). On pressure boundary conditions for the incompressible Navier-Stokes equations. *Int. J. Numer. Methods Fluids*, 1111–1145. 95
- Grimshaw, R. (1972). Nonlinear internal gravity waves in a slowly varying medium. *J. Fluid Mech.* 54, 193–207. 72
- Grimshaw, R. (1974). Internal gravity waves in a slowly varying dissipative medium. *Geophys. Fluid Dyn.* 6, 131–148. 72

- Grimshaw, R. (1975). Nonlinear internal gravity waves and their interaction with the mean wind. *J. Atmos. Sci.* 32, 1779–1793. [71](#), [72](#)
- Grosch, C. and S. Orszag (1977). Numerical solution of problems in unbounded regions: coordinate transforms. *J. Comput. Phys.* 25, 273–295. [1](#), [34](#)
- Haynes, P. (1998). The latitudinal structure of the quasi-biennial oscillation. *Q.J.R. Meteorol. Soc.* 124, 2645–2670. [92](#)
- Herzog, H.-J. (1995). Testing a radiative upper boundary condition in a nonlinear model with hybrid vertical coordinate. *Meteorol. Atmos. Phys.* 55, 185–204. [1](#), [18](#)
- Higdon, R. (2002). A two-level time-stepping method for layered ocean circulation models. *J. Comput. Phys.* 177, 59–94. [2](#), [16](#)
- Holton, J. (1992). *An introduction to dynamic meteorology* (3rd ed.), Volume 23 of *International Geophysics series*. New York: Academic Press. [4](#), [5](#), [90](#), [93](#), [103](#), [104](#)
- Holton, J. and R. Lindzen (1972). An updated theory for the quasi-biennial cycle of the tropical stratosphere. *J. Atmos. Sci.* 29, 1076–1079. [5](#), [6](#), [8](#), [89](#), [96](#)
- Horinouchi, T. (2003). Tropical cumulus convection and upward-propagating waves in middle-atmospheric GCMs. *J. Atmos. Sci.* 60, 2765–2782. [6](#), [91](#)
- Horinouchi, T. and S. Yoden (1998). Wave-mean flow interaction associated with a QBO-like oscillation simulated in a simplified GCM. *J. Atmos. Sci.* 55, 502–525. [7](#), [8](#), [89](#), [91](#), [92](#), [96](#)
- Houghton, D. and A. Kasahara (1968). Nonlinear shallow fluid flow over an isolated ridge. *Comm. Pure Appl. Math.* 21, 1–23. [35](#), [36](#), [39](#)
- Hsu, Y.-J. and Arakawa (1990). Numerical modeling of the atmosphere with an isentropic vertical coordinate. *Mon. Weather Rev.* 118, 1933–1959. [2](#)
- Iskandarani, M., D. Haidvogel, and J. Levin (2003). A three-dimensional spectral element model for the solution of the hydrostatic primitive equations. *J. Comput. Phys.* 186, 397–425. [16](#), [39](#)
- Kapitza, H. and D. Eppel (1992). The non-hydrostatic mesoscale model GESIMA. Part I: Dynamical equations and tests. *Beitr. Phys. Atmosph.* 65(2), 129–144. [3](#)
- Kasahara, A. (1974). Various vertical coordinate systems used for numerical weather prediction. *Mon. Weather Rev.* 102, 509–522. [2](#), [10](#)
- Kim, Y.-J., D. Eckermann, and H.-Y. Chun (2003). An overview of the past, present and future of gravity-wave drag parameterization for numerical climate and weather prediction models. *Dyn. Atm. Ocean* 41, 65–98. [94](#)

- Klemp, J. and D. Durran (1983). An upper boundary condition permitting internal gravity wave radiation in numerical mesoscale models. *Mon. Weather Rev.* *111*, 430–444. [1](#), [18](#)
- Klemp, J., W. Skamarock, and O. Fuhrer (2003). Numerical consistency of metric terms in terrain-following coordinates. *Mon. Weather Rev.* *131*, 1229–1239. [14](#), [32](#), [33](#)
- Konor, C. and A. Arakawa (1997). Design of an atmospheric model based on a generalized vertical coordinate. *Mon. Weather Rev.* *125*, 1649–1673. [2](#)
- Koop, C. (1981). A preliminary investigation of the interaction of internal gravity waves with a steady shearing motion. *J. Fluid Mech.* *113*, 347–386. [12](#), [52](#), [90](#)
- Lamb, H. (1975). *Hydrodynamics* (6th ed.). New York, London: Cambridge University Press. [15](#), [25](#), [104](#)
- Laprise, R. (1992). The Euler equations of motion with hydrostatic pressure as an independent variable. *Mon. Weather Rev.* *120*, 197–207. [2](#)
- Laprise, R. and W. Peltier (1989a). The linear stability of nonlinear mountain waves: Implications for the understanding of severe downslope windstorms. *J. Atmos. Sci.* *46*, 545–564. [63](#), [93](#)
- Laprise, R. and W. Peltier (1989b). The structure and energetics of transient eddies in a numerical simulation of breaking mountain waves. *J. Atmos. Sci.* *46*, 565–585. [63](#), [93](#)
- Leutbecher, M. (1998). *Die Ausbreitung orographisch angeregter Schwerewellen in die Stratosphäre*. Ph. D. thesis, Ludwig-Maximilians-Universität München, Institut für Physik der Atmosphäre des DLR, Oberpfaffenhofen. [11](#), [12](#)
- Lignieres, F. (1999). The small-Peclet-number approximation in stellar radiative zones. *Astron. Astrophys.* *348*, 933–939. [11](#)
- Lilly, D. (1962). On the numerical simulation of buoyant convection. *Tellus* *14* (2), 148–172. [101](#)
- Lindzen, R. (1987). On the development of the theory of the QBO. *Bull. Am. Meteorol. Soc.* *68* (4), 329–337. [6](#)
- Lindzen, R., E. Batten, and J. Kine (1968). Oscillations in atmospheres with tops. *Mon. Weather Rev.* *96*, 133–140. [1](#)
- Lindzen, R., B. Farrell, and D. Jacqmin (1982). Vacillations due to wave interference: Applications to the atmosphere and to annulus experiments. *J. Atmos. Sci.* *39*, 14–23. [94](#)
- Lindzen, R. and J. Holton (1968). A theory of the quasi-biennial oscillation. *J. Atmos. Sci.* *25*, 1095–1107. [5](#), [6](#), [89](#)

- Lipps, F. and R. Hemler (1982). A scale analysis of deep moist convection and some related numerical calculations. *J. Atmos. Sci.* 39, 2192–2210. 1, 21
- Luo, H. and T. Bewley (2004). On the contravariant form of the Navier-Stokes equations in time-dependent curvilinear coordinates. *J. Comput. Phys.* 199, 355–375. 100
- Madala, R. and S. Piacsek (1977). A semi-implicit numerical model for baroclinic oceans. *J. Comput. Phys.* 23, 167–178. 2, 16
- Madden, R. and P. Julian (1972). Description of global scale circulation cells in the tropics with 40-50 day period. *J. Atmos. Sci.* 29, 1109–1123. 94
- Madden, R. and P. Julian (1994). Observations of the 40-50-day tropical oscillation - a review. *Mon. Weather Rev.* 122, 814–837. 94
- McIntyre, M. (1994). The quasi-biennial oscillation (QBO): some points about the terrestrial QBO and the possibility of related phenomena in the solar interior. In Nesme-Ribes (Ed.), *The Solar engine and its influence on the terrestrial atmosphere and climate*, Volume 25 of *Nato ASI Subseries I*, Heidelberg, pp. 293–320. Springer-Verlag. 5, 6
- Miles, J. (1961). On the stability of heterogeneous shear flows. *J. Fluid Mech.* 10, 496–508. 11
- Milne-Thomson, L. (1968). *Theoretical Hydrodynamics* (5th ed.). The MacMillan Press Ltd. 30
- Moncrieff, M. (2004). Analytic representation of the large scale organization of tropical convection. *J. Atmos. Sci.* 61, 1521–1538. 94
- Morton, B. (1984). The generation and decay of vorticity. *Astrophys. Fluid Dynamics* 28, 277–308. 17, 18
- Nadiga, B., L. Margolin, and P. Smolarkiewicz (1996). Different approximations of shallow fluid flow over an obstacle. *Phys. Fluids* 8, 2066–2077. 34, 35, 39
- NAG (2004). *NAG Fortran library manual* (NP3546/20A ed.). C06 - summation of series. 66
- Namin, M., B. Lin, and R. Falconer (2001). An implicit numerical algorithm for solving non-hydrostatic free-surface flow problems. *Int. J. Numer. Methods Fluids* 35, 341–356. 16, 39
- Nicoud, F. and T. Schönfeld (2002). Integral boundary conditions for unsteady biomedical CFD applications. *Int. J. Numer. Methods Fluids* 40, 457–465. 29
- Otobe, N., S. Sakai, S. Yoden, and M. Shiotani (1998). Visualization and WKB analysis of the internal gravity wave in the QBO experiment. *Nagare, Japan Society of Fluid Mechanics* 17(3). <http://www.nagare.or.jp/mm/98/index.htm>. 49, 58, 83, 84

- Phillips, N. (1957). A coordinate system having some special advantages for numerical forecasting. *J. Meteor.* *14*, 184–185. [2](#), [3](#)
- Phillips, N. (1990). Dispersion in large scale weather prediction. *WMO Sixth IMO lecture*. [1](#), [10](#)
- Plumb, R. (1977). The interaction of two internal waves with the mean flow: implications for the theory of the quasi-biennial oscillation. *J. Atmos. Sci.* *34*, 1847–1858. [5](#), [6](#), [7](#), [51](#), [52](#), [70](#), [71](#), [73](#), [76](#), [85](#), [89](#)
- Plumb, R. and D. McEwan (1978). The instability of a forced standing wave in a viscous stratified fluid: A laboratory analogue of the quasi-biennial oscillation. *J. Atmos. Sci.* *35*, 1827–1839. [3](#), [5](#), [6](#), [7](#), [42](#), [43](#), [44](#), [46](#), [47](#), [51](#), [59](#), [73](#), [83](#), [84](#), [85](#), [89](#), [95](#)
- Poulin, F., G. Flierl, and J. Pedlosky (2003). Parametric instability in oscillatory shear flows. *J. Fluid Mech.* *481*, 329–353. [94](#)
- Prandtl, L. (1961). *Ludwig Prandtl Gesammelte Abhandlungen*, Volume II, Chapter Turbulenz und Wirbelbildung. Springer-Verlag. [16](#)
- Prusa, J. and P. Smolarkiewicz (2003). An all-scale anelastic model for geophysical flows: dynamic grid deformation. *J. Comput. Phys.* *190*, 601–622. [3](#), [21](#), [22](#), [23](#), [24](#), [26](#), [28](#), [97](#)
- Prusa, J., P. Smolarkiewicz, and R. Garcia (1996). On the propagation and breaking at high altitudes of gravity waves excited by tropospheric forcing. *J. Atmos. Sci.* *53*, 2186–2216. [1](#), [2](#), [3](#), [12](#), [18](#)
- Prusa, J., P. Smolarkiewicz, and A. Wyszogrodzki (2001). Simulations of gravity wave induced turbulence using 512 PE CRAY T3E. *Int. J. Applied Math. Comp. Science*, 2186–2216. [23](#)
- Read, P., S. Lewis, and R. Hide (1997). Laboratory and numerical studies of baroclinic waves in an internally heated rotating fluid annulus: a case of wave/vortex duality? *J. Fluid Mech.* *337*, 155–191. [58](#)
- Richtmyer, R. and K. Morton (1967). *Difference Methods for Initial-Value Problems* (2nd ed.). New York: Wiley-Interscience. [39](#)
- Riemann, B. (1873, May). On the hypotheses which lie at the basis of geometry. *Nature VIII*. [2](#)
- Rotunno, R. and P. Smolarkiewicz (1995). Vorticity generation in the shallow-water equations as applied to hydraulic jumps. *J. Atmos. Sci.* *52*, 320–330. [34](#)
- Schär, C., D. Leuenberger, O. Fuhrer, D. Lüthi, and C. Girard (2002). A new terrain-following vertical coordinate formulation for atmospheric prediction models. *Mon. Weather Rev.* *130*, 2459–2480. [32](#)

- Schumann, U. (1996). Direct and large eddy simulations of stratified homogeneous shear flows. *Dyn. Atm. Ocean* 23, 81–98. 93
- Schumann, U., T. Hauf, H. Höller, H. Schmidt, and H. Volkert (1987). A mesoscale model for the simulation of turbulence, clouds and flow over mountains: formulation and validation examples. *Beitr. Phys. Atmosph.* 60, 413–446. 3
- Shutts, G. (2001). A linear model of back-sheared flow over an isolated hill in the presence of rotation. *J. Atmos. Sci.* 58, 3923–3311. 93
- Simmons, A. and D. Burridge (1981). An energy and angular momentum conserving vertical finite difference scheme and hybrid vertical coordinates. *Mon. Weather Rev.* 109, 758–766. 2, 16
- Simmons, A. and A. Hollingsworth (2002). Some aspects of the improvement in skill of numerical weather prediction. *Q.J.R. Meteorol. Soc.* 128, 647–677. 91
- Skamarock, W., P. Smolarkiewicz, and J. B. Klemp (1997). Preconditioned conjugate-residual solvers for Helmholtz equations in nonhydrostatic models. *Mon. Weather Rev.* 125, 587–599. 28
- Smith, R. (1979). The influence of mountains on the atmosphere. *Adv. Geophys.* 21, 87–230. 11
- Smith, R. (1980). Linear theory of stratified hydrostatic flow past an isolated mountain. *Tellus* 32, 348–364. 46, 84
- Smith, R. (1985). On severe downslope winds. *J. Atmos. Sci.* 42, 2597–2603. 93
- Smolarkiewicz, P. and G. Grell (1992). A class of monotone interpolation schemes. *J. Comput. Phys.* 101, 431–440. 27
- Smolarkiewicz, P., V. Grubišić, and L. Margolin (1997). On forward-in-time differencing for fluids: Stopping criteria for iterative solutions of anelastic pressure equations. *Mon. Weather Rev.* 125, 647–654. 97
- Smolarkiewicz, P., V. Grubišić, L. Margolin, and A. Wyszogrodzki (1999). Forward-in-time differencing for fluids: Nonhydrostatic modeling of fluid motions on a sphere. In *Proc. 1998 Seminar on Recent Developments in Numerical Methods for Atmospheric Modeling*, Reading, UK, pp. 21–43. Eur. Cent. For Medium-Range Weather Forecasts. 22
- Smolarkiewicz, P. and L. Margolin (1993). On forward-in-time differencing for fluids: Extension to a curvilinear framework. *Mon. Weather Rev.* 121, 1847–1859. 26, 27, 35, 55
- Smolarkiewicz, P. and L. Margolin (1994). Variational solver for elliptic problems in atmospheric flows. *Int. J. Applied Math. Comp. Science* 4, 527–551. 28

- Smolarkiewicz, P. and L. Margolin (1997). On forward-in-time differencing for fluids: An Eulerian/semi-Lagrangian non-hydrostatic model for stratified flows. *Atmos. Ocean Special* 35, 127–152. 28
- Smolarkiewicz, P. and L. Margolin (1998). Mpdata: A finite difference solver for geophysical flows. *J. Comput. Phys.* 140, 459–480. 27, 28
- Smolarkiewicz, P., L. Margolin, and A. Wyszogrodzki (2001). A class of nonhydrostatic global models. *J. Atmos. Sci.* 58, 349–364. 23, 27, 28, 30, 55
- Smolarkiewicz, P. and J. Prusa (2002). Forward-in-time differencing for fluids: simulation of geophysical turbulence. In D. Drikakis and B. Guertz (Eds.), *Turbulent Flow Computation*, pp. 207–240. Kluwer Academic Publishers. 26, 27
- Smolarkiewicz, P. and J. Prusa (2004). Toward mesh adaptivity for geophysical turbulence. *Int. J. Numer. Methods Fluids*. to appear. 25, 102
- Smolarkiewicz, P. and J. Pudykiewicz (1992). A class of semi-Lagrangian approximations for fluids. *J. Atmos. Sci.* 49, 2082–2096. 27, 30
- Staquet, C. and J. Sommeria (2002). Internal gravity waves: from instabilities to turbulence. *Annu. Rev. Fluid Mech.* 34, 559–593. 12
- Stoker, J. (1957). *Water Waves*, Volume IV of *Pure and Applied Mathematics*. New York: Interscience Publishers. 104
- Suarez, M., A. Arakawa, and D. Randall (1983). Parameterization of the planetary boundary layer in the ucla general circulation model: Formulation and results. *Mon. Weather Rev.* 111, 2224–2243. 2
- Takahashi, M. (1999). Simulation of the quasi-biennial oscillation in a general circulation model. *Geophys. Res. Lett.* 26(9), 1307–1310. 7, 92
- Temperton, C. (1983). Self-sorting mixed-radix fast Fourier transforms. *J. Comput. Phys.* 52, 1–23. 67
- Temperton, C., M. Hortal, and A. Simmons (2001). A two-time-level semi-Lagrangian global spectral model. *Q.J.R. Meteorol. Soc.* 127, 111–127. 16
- Teoh, S., G. Ivey, and J. Imberger (1997). Laboratory study of the interaction between two internal wave rays. *J. Fluid Mech.* 336, 91–122. 12
- Tiedke, M. (1989). A comprehensive mass flux scheme for cumulus parameterization. *Mon. Weather Rev.* 117, 1779–1800. 92
- Tindall, J. (2003). *Dynamics of the tropical tropopause and lower stratosphere*. Ph. D. thesis, University of Reading. 7

- Tremback, C., J. Powell, W. Cotton, and R. Pielke (1987). The forward-in-time upstream advection scheme: extension to higher orders. *Mon. Weather Rev.* *115*, 540–555. [26](#)
- Trenberth, K. and D. Stepaniak (2002). A pathological problem with NCEP reanalyses in the stratosphere. *J. Climate* *15*, 690–695. [1](#)
- Ucellini, L., D. Johnson, and R. Schlesinger (1979). An isentropic and sigma coordinate hybrid numerical model: model development and some initial tests. *J. Atmos. Sci.* *36*, 390–413. [2](#)
- Untch, A. (1998). Aspects of stratospheric modelling at ECMWF. In *Proc. ECMWF Workshop on Recent Developments in numerical methods for atmospheric modelling*, Reading, UK, pp. 442–453. Eur. Cent. For Medium-Range Weather Forecasts. [7](#), [91](#), [96](#)
- Uppala, S., P. Kallberg, A. Simmons, and collaborators (2004). ECMWF re-analysis project report series: The ERA-40 re-analysis. Technical report, ECMWF, Shinfield Park, Reading. in preparation. [4](#), [89](#)
- ISI (10th July 2002). Web of science. <http://wos.mimas.ac.uk>. [3](#)
- Wedi, N. and P. Smolarkiewicz (2004a). Extending Gal-Chen & Somerville terrain-following coordinate transformation on time-dependent curvilinear boundaries. *J. Comput. Phys.* *193*, 1–20. [1](#)
- Wedi, N. and P. Smolarkiewicz (2004b). Laboratory for internal gravity-wave dynamics: The numerical equivalent to the quasi-biennial oscillation (QBO) analogue. *Int. J. Numer. Methods Fluids*. in press. [1](#)
- Welch, W., P. Smolarkiewicz, R. Rotunno, and B. Boville (2001). The large-scale effects of flow over periodic mesoscale topography. *J. Atmos. Sci.* *58*, 1477–1492. [30](#)
- Winters, K., P. Lombard, J. Riley, and E. D’Asaro (1995). Available potential energy and mixing in density-stratified fluids. *J. Fluid Mech.* *289*, 115–128. [61](#), [62](#), [63](#), [64](#)
- Wu, J. and J. Wu (1998). Boundary vorticity dynamics since Lighthill’s 1963 article: review and development. *Theoret. Comput. Fluid Dynamics* *10*, 459–474. [17](#)
- [www.gfd-dennou.org](http://www.gfd-dennou.org) (20th May 2004). Atmosphere and ocean in a laboratory. [http://www.gfd-dennou.org/library/gfd\\_exp/exp\\_e/index.htm](http://www.gfd-dennou.org/library/gfd_exp/exp_e/index.htm). [6](#), [43](#), [44](#), [47](#), [49](#), [50](#), [58](#)
- Zdunkowski, W. and A. Bott (2003). *Dynamics of the Atmosphere: A course in theoretical meteorology*. Cambridge, New York: Cambridge University Press. [97](#), [98](#)



# Acknowledgements

This dissertation has been written in collaboration with the Institute for Atmospheric Physics at Deutsches Zentrum für Luft- und Raumfahrt (DLR), the National Centre for Atmospheric Research (NCAR) and the European Centre for Medium Range Weather Forecasts (ECMWF). The numerical experiments have been performed on the IBM power4 supercomputer at ECMWF.

I would like to thank Prof Dr Ulrich Schumann for supervising this dissertation and for his support and encouragement. I am very grateful to Dr Piotr Smolarkiewicz for his invaluable guidance, enthusiasm, and his persistent criticism which substantially improved this thesis. I would also like to thank Prof Dr Joseph Egger for his helpful comments on an earlier version of the manuscript.

I thank all my colleagues at ECMWF for their support during the course of my work. I am especially grateful to Dr Agathe Untch, Dr Mariano Hortal and Dr Martin Miller for numerous discussions, many helpful comments and for reviewing earlier versions of the manuscript. Furthermore, I would like to thank my wife Dr Sabine Gruber for her constructive suggestions. I am also indebted to Dr Anthony Hollingsworth for suggesting to simulate numerically the Plumb and McEwan laboratory experiment.

Finally, I am grateful to ECMWF and NCAR for providing the necessary library and computing facilities. A special thanks to Dr Adrian Tompkins for his help with IDL.



# Curriculum vitae

Nils Peter Wedi

## Persönliche Daten

Anschrift	24 Beauchief Close Reading, RG6 4HY Great Britain
Geburtsdatum	29. November 1969
Geburtsort	Greven, Krs Steinfurt, Nordrhein-Westfalen
Staatsangehörigkeit	deutsch
Familienstand	verheiratet mit Dr. Sabine Gruber

## Schulbildung

1976-1979	Gangolf-Grundschule, Nordwalde, Nordrhein-Westfalen
1979-1988	Städt. Gymnasium Borghorst, Nordrhein-Westfalen
Juni 1988	Abitur

## Wehrdienst

1988-1990	Grundwehrdienst, Begleitbatterie 7, Dülmen
-----------	--

## Studium

1990-1995	Studium der Meteorologie an der Johannes Gutenberg-Universität Mainz
Feb. 1995	Diplom in Meteorologie. Titel der Diplomarbeit: "Die Strahlungsbilanz in komplexem Terrain" (Betreuer: Prof. Dr. W. Zdunkowski)
seit Nov. 2002	Promotionsstudent an der Ludwig-Maximilians-Universität München

## Beruflicher Werdegang

seit Jan. 1995	Wissenschaftlicher Mitarbeiter am Europäischen Zentrum für Mittelfristige Wettervorhersage in Reading (Großbritannien)
----------------	--